#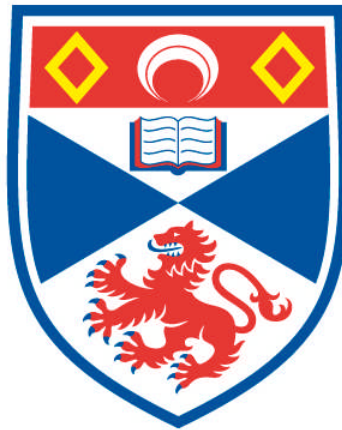 THE DEVELOPMENT AND ASSESSMENT OF CARDIAC MAGNETIC RESONANCE IMAGING FOR THE DETECTION OF AGE- AND DISEASE-RELATED CHANGES IN THE HUMAN HEART

Shona Matthew

**A Thesis Submitted for the Degree of PhD
at the
University of St Andrews**

2012

The Development and Assessment of Cardiac Magnetic Resonance Imaging for the Detection of Age- and Disease-Related Changes in the Human Heart

Shona Matthew
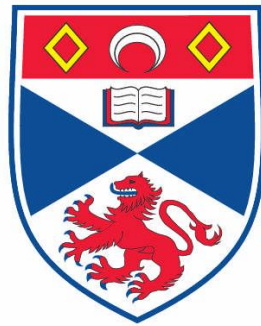
This thesis is submitted in partial fulfilment for the degree of PhD at the University of St Andrews

31 July 2012

This thesis is dedicated to my foster parents

Frank & Mary Dow

and

Christine & Jimmy Craig

For showing me a better life. Fond memories and eternal gratitude.

Contents

2. The Human Heart — 49

3. The Development of Cardiac Magnetic Resonance Imaging — 66

6. Assessment of clinical differences at 1.5T between quantitative right and left ventricular volumes and ejection fractions using MRI   122

7. Normal Ranges of Left Ventricular Functional Parameters at 3 Tesla   132

Abstract and scope

Abstract

Cardiovascular disease (CVD) is a term used to describe a variety of diseases and events that impact the heart and circulatory system. CVD is the United Kingdom's (UKs) biggest killer, causing more than 50,000 premature deaths each year. Early recognition of the potential for magnetic resonance imaging (MRI) to provide a versatile, non-ionising, non-invasive, technique for the assessment of CVD resulted in the modality becoming an area of intense interest in the research, radiology and cardiology communities. The first half of this thesis reviews some of the key developments in magnetic resonance hardware and software that have led to cardiac magnetic resonance imaging (CMRI) emerging as a reliable and reproducible tool, with a range of applications ideally suited for the evaluation of cardiac morphology, function, viability, valvular disease, perfusion, and congenital cardiomyopathies. In addition to this, the advantages and challenges of imaging at 3.0T in comparison to 1.5T are discussed. The second half of this thesis presents a number of investigations that were specifically designed to explore the capability of CMRI to accurately detect subtle age and disease related changes in the human heart. Our investigations begin with a study at 1.5T that explores the clinical and scientific significance of the less frequently used measure of right ventricular function to test the hypothesis that the inclusion of this data

provides a more informative assessment of overall cardiac function. The focus then shifts to imaging at 3.0T and the challenges of optimising cardiac imaging at this field strength are discussed. Normal quantitative parameters of cardiac function are established at this field strength for the left ventricle and the left atrium of local volunteers. These values are used to investigate disease related changes in left ventricle and left atrium of distinct patient cohorts. This work concludes by investigating the impact of gadolinium-based contrast agents on the quantitative parameters of cardiac function.

The Scope of the Thesis

This thesis is concerned with studies regarding both the basic principles and clinical practice of CMRI when performed at 1.5T and 3.0T. Chapters 2–5 provide the platform of knowledge necessary to appreciate the experimental work presented in 6–9 of this thesis.

Chapter 1 begins with a brief introduction to the physics of magnetic resonance imaging before comparing the various cardiac imaging modalities routinely available in British hospitals today.

Chapter 2 provides an overview of normal cardiac anatomy and function before discussing the cardiac disease-related changes that are relevant to chapters 6–9.

Chapter 3 is a literature review, which explores some of the key hardware and software developments that have led to a paradigm shift in CMRI over the past three decades. The overall impact of these developments on this research is laid into context.

Chapter 4 starts with a brief comparison of the radio frequency and gradient fields of the 1.5T and 3.0T Siemens imaging systems utilised for the purpose of this research. This is followed by a discussion on the advantages and challenges of imaging at 3.0 Tesla in comparison to 1.5 Tesla.

Chapter 5 defines a cardiac magnetic resonance imaging protocol and discussed two fast gradient echo sequences, both of which are fundamental to cardiac imaging. In addition to this, chapter 5 contains examples of the images obtained using these sequences together with a brief discussion of the clinical information that can be gained from some of these images. The chapter concludes with an introduction to image analysis and the important clinical parameters that are obtained from post-processing short-axis cine images.

Chapters 6–8 investigate the clinical and scientific significance of novel or infrequently used measures of cardiac function with the hypothesis that the inclusion of this data may provide a more informative assessment of overall cardiac function.

Chapter 6 This chapter details a study that was designed to test inter-observer reproducibility between a novice and experienced observer. In conjunction to this, the quantitative right and left ventricular analysis of three distinct clinical cohorts were examined with the hypothesis that the inclusion of RV data may generate a more informative characterisation of cardiac function.

Chapter 7 Begins with a discussion on the challenges faced in optimising ventricular imaging at 3.0T. This is followed by a study designed to define subtle age-related functional changes in both male and female healthy volunteers in a bid to provide normal ranges of cardiac function at 3.0T for the local population. Measures of ejection fraction, end-diastolic volume, end-systolic volume, and left ventricular mass for 100 volunteers are obtained and compared. This chapter concludes by using these normal ranges to determine if disease-related cardiac changes exist in a cohort of patients with Systemic Lupus Erythematosus.

Chapter 8 An optimised LA protocol is implemented to identify possible volumetric variations between healthy volunteers and patient cohorts with carefully defined clinical cardiac conditions.

Gadolinium-based contrast agents are used in CMRI protocols to enhance imaging by shortening the inherent T1 values of tissue, effectively creating a contrast change.

Chapter 9 focuses on the effect of contrast agent delivery on important calculated cardiac variables, particularly on the value of LV mass. Significant differences are highlighted that may have important implications for the correct interpretation of patient data in clinical studies.

Chapter 10 concludes this thesis and consolidates the achievements of chapters 6–9 before discussing the future of CMRI. This thesis is drawn to a close with an overview of present studies and future work.

Appendix A: This appendix begins with a modification to the Bloch Equations to provide explicate forms for M_x, M_y and M_z. This is followed by a valid solution to an incoherent steady-state imaging technique where the transverse magnetisation is essentially zero before the application of the excitation pulse (FLASH). The equitation describing the magnetisation from a coherent steady-state technique (TrueFISP) is given without proof.

Part two of this appendix describes an essential quality assurance test that is routinely performed on all of our MRI scanners to ensure that they are performing to the manufacturer's specifications. Novel matlab code is presented that efficiently post-processes the images acquired during testing.

Appendix B contains the MATLAB® code discussed in Appendix A of this thesis.

Acknowledgements

I would like to express my gratitude to Professor Malcolm H. Dunn of the University of St Andrews for his loyalty, dedication, enthusiasm, support and kindness. It has been a privilege and an honour to work under his supervision.

Thanks also to the significant others who helped make this such an enjoyable journey:

This project would not have been possible without the kind consent of the clinical patients, healthy volunteers and *TASCFORCE participants who kindly agreed to their cardiac magnetic resonance images being used for teaching and research purposes.

Tayside Screening For risk of Cardiac Events and the effect of statin on risk reduction.

Finally, thanks to Dr Tom Gallacher of the University of St Andrews for his substantial help in developing the novel MATLAB® code discussed in appendix A of this thesis (thomas.gallacher@gmail.com).

James Clerk Maxwell.

13 June 1831 – 5 November 1879

"… the work of James Clerk Maxwell changed the world forever …"

Albert Einstein. *New Scientist* 1991; **130:** 49.

$$\nabla \times E = -\frac{\partial B}{\partial t}$$

Significant events in the history of NMR and MRI

❖ *Nuclear Magnetic Resonance: Isidor IsaacRabi (1898–1988); Nobel prize for Physics 1944.*

❖ *Nuclear Magnetic Precision Measurements: Felix Bloch (1905–1983) & Edward Mills Purcell (1912–1997); 1952 Nobel Prize for Physics.*

❖ *Magnetic Resonance Imaging: Paul Christian Lauterbur (1929–2007) & Sir Peter Mansfield (Born 1933); 2003 Nobel Prize for Physiology or Medicine.*

❖ *Spin: Otto Stern (1888–1969); 1943 Nobel Prize for Physics.*

❖ *Spin: Walther Gerlach (1889–1979).*

❖ *Nuclear Magnetic Resonance: Edward Mills Purcell (1912–1997); 1952 Nobel Prize for Physics.*

❖ *Spin Angular Momentum: Wolfgang Ernst Pauli (1900–1958); 1945 Nobel Prize for Physics.*

❖ *The Zeeman Effect: Pieter Zeeman (1865–1943); Nobel Prize for Physics 1902.*

❖ *The Boltzmann Distribution: Ludwig Eduard Boltzmann (1844–1906).*

❖ *The Tesla (S.I. Unit of Magnetic Field): Nikola Tesla (1856–1943).*

❖ *Superconductivity: Heike Kamerlingh Onnes (1853–1926); 1913 Nobel Prize for Physics.*

❖ *The Larmor Equation: Joseph Larmor (1857–1942).*

❖ *Pulsed Fourier Transform NMR. Richard R Ernst (Born 1933); Nobel Prize for Chemistry 1991.*

❖ *Construction of the first whole-body MRI scan: University of Aberdeen 1978-79.*

1. The Basics of MRI

A healthy adult human heart expands and contracts an average of 100,000 times a day, continuously pumping approximately 7,000 litres of blood through a system of veins, arteries and capillaries that is in excess of 96,000 kilometres long [1]. This continuous flow of blood through the cardiovascular system is of paramount importance as it delivers nutrients, removes waste and is central to the production of energy and other materials necessary for life (metabolism).

Cardiovascular diseases (CVDs) are a group of disorders that negatively impact the heart and blood vessels. It is estimated that CVDs will be responsible for almost 23.6 million deaths globally per annum by 2030, with men and women being almost equally effected [2]. Consequently, there is a move towards the early identification of cardiovascular disease risk, as proactive disease management may be effective in slowing disease progression [3]. This would have major financial benefits for our national health service (NHS), but more importantly, disease management has the potential to benefit the patient in terms of morbidity and mortality. For example, a patient's long-term survival may be improved by revascularisation procedures, such as coronary artery bypass grafting, if it can be established

that there are viable heart muscle cells in the cardiac territory affected by the occluded vessel [4, 5]

1.1 Diagnostic Imaging

Diagnostic imaging plays a vital role in the identification of cardiac disease-related changes. A number of well-established techniques are available for this purpose, all of which obtain images by measuring the interaction between energy and a biological tissue. This thesis focuses on the application of cardiac magnetic resonance imaging (CMRI), which is a comparatively new imaging modality. In particular, we investigate the ability of CMRI to detect age and disease related changes in the human heart. This chapter begins with a brief introduction to magnetic resonance imaging (MRI); however the interested reader is directed to the following books for a more thorough discussion of the science involved in this technique [6, 7].

1.2 Magnetic Resonance Imaging

Paul Lauterbur produced the first primitive magnetic resonance image in 1973. Subsequent rapid developments in hardware and software lead to the introduction of the first clinical whole-body scanners less than 10 years later. Today MRI is established as an essential radiological tool with an estimated 60 million MRI exams performed each year, worldwide [8].

1.3 Nuclear Magnetic Resonance

Magnetic resonance imaging is based on the principles of proton nuclear magnetic resonance (NMR). NMR is used to induce and detect a very weak radio frequency signal that is a manifestation of nuclear magnetism. NMR can only be performed on isotopes with a net spin angular momentum whose natural abundance is high enough to be detected.

1.4 Spin Angular Momentum

Nuclear spin angular momentum (J) is a fundamental property of nature that makes the nucleus a continuously rotating positive charge, and as a moving charge it has an associated magnetic field and magnetic dipole moment (μ) (Figure 1.1).
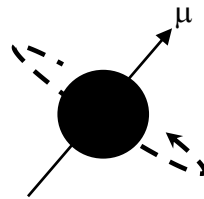
Figure 1.1 Spin angular momentum makes the proton a continuously rotating positive charge.

The magnetic dipole moment of a nucleus is directly proportional to the spin angular momentum:

$$\mu = \gamma J \qquad (1.1)$$

Where γ is a proportionality constant, known as the gyromagnetic ratio.

1.4.1 Gyromagnetic Ratio

The gyromagnetic ratio (γ) relates the nuclear rotating frequency to the strength

of the magnetic field and is commonly expressed in terms of Mega-Hertz per

Tesla (MHz/T) in MRI. Every nucleus suitable for MRI has its own specific

gyromagnetic value. For example, hydrogen nuclei (^{1}H) have a gyromagnetic

ratio of:

$$\gamma = 42.6 MHz/T \qquad (1.2)$$

The magnitude of the nuclear spin angular momentum is given by:

$$|J| = \sqrt{I(I+1)}\,\hbar \qquad (1.3)$$

Where I is the spin angular momentum quantum number and $\hbar$ is Planck's

constant. The magnitude of the angular momentum along a chosen axis is given

by convention as:

$$J_z = m_I \hbar \qquad (1.4)$$

Where m_I is the magnetic quantum number and generally = -I, -I+1,…I-1, I.

There are 2I+1 allowed orientations or quantum states of the nucleus. All of

which have the same energy in the absence of a magnetic field.

1.5 Hydrogen Nuclei

Protons, neutron and electrons are spin one-half particles. An atom with one proton, one neutron and one electron has a net nuclear spin of 1 and a net electronic spin of ½. Where two spins of opposite signs are paired, the observable manifestation of spin is eliminated.

Hydrogen (^{1}H) nuclei only contain a single proton, giving them a net nuclear spin of ½. This, coupled with their relatively high gyromagnetic ratio and biological abundance of ~63% in the human body, makes them ideal for magnetic resonance imaging. Water-based tissues, such as the myocardium, have an even higher biological abundance of ~80%.

1.6 The Zeeman Effect

In the absence of an external magnetic field ($\mathbf{B_0}$), the individual magnetic dipole moments of the protons within a sample have no preferred orientation, and therefore precess incoherently. However, once exposed to an external field, the spin one-half nuclei experience a torque that causes their magnetic moments to begin precessing in one of two allowed quantum states. The lower energy, spin up or spin +½ state, is aligned parallel with the applied magnetic field whilst the higher energy, spin down or spin -½ state, is aligned anti-parallel to the external field.

1.7 The Boltzmann Distribution

At room temperature, the population of spins in the lower energy level (N_+) will slightly outnumber the population of spins in the upper energy level (N_-) (Figure 1.2). This spin excess would equate to 1 in 10^6 at 1.5 Tesla.
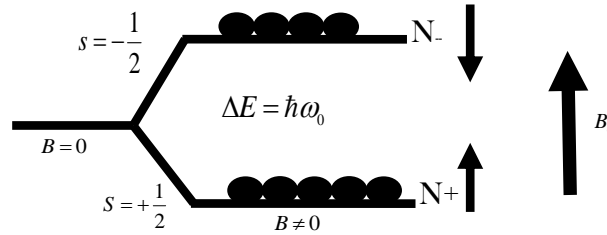
Figure 1.2 The Zeeman energy levels for a spin one-half system.

This division of spins is predicted by the classical Boltzmann distribution:

$$\frac{N_-}{N_+} = e^{-\frac{\Delta E}{kT}} \qquad (1.5)$$

Where ΔE = the energy difference between the spin states (1.4); k = Boltzmann's constant, (1.3805×10^{-23} J/K); and T = the temperature in Kelvin.

$$\Delta E = E_2 - E_1 = 2\mu B_0 \qquad (1.6)$$

$$\Delta E = 2\gamma m_I \hbar B_0 \qquad (1.7)$$

1.8 Larmor Equation

For the spin ½ proton, m_I = +/- ½, hence the energy difference between the two states is:

$$\Delta E = \gamma \hbar B_0 \qquad\qquad (1.8)$$

By applying Planck's Law to equation (1.6), we obtain:

$$h v = \gamma \hbar B_0 \qquad\qquad (1.9)$$

thus, allowing us to determine a value for the precessional frequency of the protons using the most fundamental equation in MRI physics – the Larmor Equation:

$$\omega = \gamma B_0 \qquad\qquad (1.10)$$

1.9 Net Magnetisation Vector

Although individual spins obey the laws of quantum mechanics, the average behaviour of a group of spins (called spin packets) experiencing the same magnetic field strength, is best described using classical mechanics. Hence, the vector sum of the magnetisation vectors from all spin packets is represented by a net magnetisation vector ($\mathbf{M_0}$) (Figure 1.3).
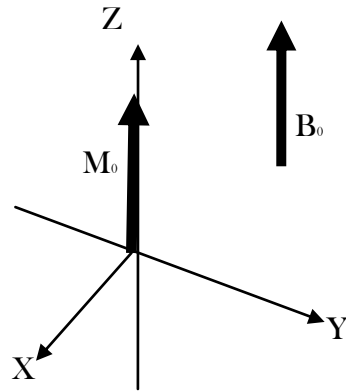
Figure 1.3 The vector sum of all spin packets is represented by the net magnetisation vector, $\mathbf{M_0}$.

$$M_0 = (N_+ - N_-)\left(\gamma\frac{\hbar}{2}\right) \qquad (1.11)$$

From equation (1.5):
$$\frac{N_-}{N_+} = e^{\frac{-\Delta E}{kT}}$$

And for small $\Delta E/kT$:
$$N_+ \approx N_-\left(1 + \frac{\Delta E}{kT}\right)$$

On rearranging:
$$(N_+ - N_-) = \frac{N_-\Delta E}{kT}$$

Substituting into (1.11):
$$M_0 = \frac{N_-\Delta E}{kT}\frac{\gamma\hbar}{2}$$

We finally obtain:
$$M_0 = \left(\frac{P_d}{2}\right)\frac{\gamma\hbar B}{kT}\frac{\gamma\hbar}{2} \qquad (1.12)$$

Where P_d represents the density of protons per unit volume ($P_d/2 = N_-$).

The signal in MRI comes predominantly from $\mathbf{M_0}$ and its magnitude is dependent on a number of factors, which include the magnitude of $\mathbf{B_0}$, the proton density of the tissue, and the proton's magnetic moment component ($\gamma\hbar/2$).

$$M_0 = \frac{P_d \gamma^2 \hbar^2}{4kT} B_0 \qquad (1.13)$$

1.10 The Main Magnetic Field

Magnetic resonance imaging involves the interaction of three types of magnetic field: the main (static) magnetic field, an oscillating radio frequency (RF) field, and gradient magnetic fields. The primary job of the main magnetic field in MRI is to align the spins to form the net magnetisation vector. This is achieved using superconducting magnets as they provide a range of desirable attributes including field strengths in the Tesla range that have excellent homogeniety and temporal stability.

1.10.1 Superconducting Magnets

Superconducting magnets are a form of electromagnet and consist of a solenoid (a coil of superconducting multifilament wire made of niobium-titanium alloy embedded as fine filaments in a copper matrix). The solenoid is cryogenically cooled to a very low temperature of around 4.2°K using liquid helium. This reduces the resistance in the wires to zero, permitting the very strong electrical

currents required to create high magnetic fields to be passed through the wires without generating significant heat. A superconducting magnetic field stores a substantial amount of energy (Es), which can be calculated using:

$$Es = \frac{1}{2}LI^2 \qquad (1.14)$$

Where L is the inductance of the coil windings and I is the current flowing through them. So for a 1.5T magnet with 150 Henrys of inductance and 200 amperes of current, the stored energy would equate to 3.6MJ.

1.11 The Radio Frequency Field

In equilibrium, the net magnetisation vector aligns with the main magnetic field along the z-axis. M_0 is several magnitudes smaller than B_0 (µT v 1.5T). In addition to this, M_0 is not an oscillating function, and hence cannot be detected by a receiver coil. To resolve this issue, a radio frequency (RF) pulse (B_1) is applied in a plane perpendicular to B_0 (Figure 1.4).
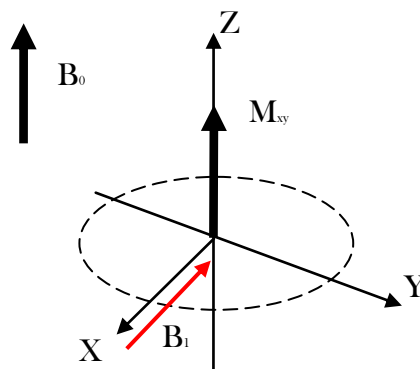
Figure 1.4 An RF pulse is applied in a plane perpendicular to B_0

1.12 Resonance

If the precessional frequency of the RF pulse matches that of the Larmor frequency of the protons then energy is added to the system and resonance can occur. During resonance, spins are encouraged to align with the $\mathbf{B_1}$ field. This phase coherence results in the formation of a net transverse magnetisation vector in the x–y plane ($\mathbf{M_{xy}}$) (Figure 1.4) that precesses simultaneously about $\mathbf{B_0}$ and $\mathbf{B_1}$ in a process known as nutation.

1.12.1 Rotating Frame of Reference
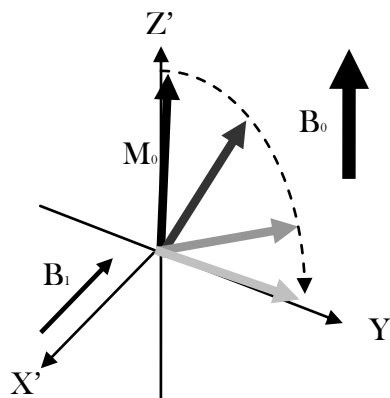
Figure 1.5 Using a rotating frame of reference simplifies the concept of flipping.

The concept of nutation is simplified in MRI physics by considering a rotating frame of reference (rotating at the Larmor frequency about the z-axis). In a rotating frame, spins rotating at the Larmor frequency appear stationary whilst those rotating at higher or lower frequencies are seen to gain or lose phase in comparison.

An observer within the rotating frame of reference will witness a simple arc motion as the magnetisation vector is flipped from the z-axis into the x–y plane (Figure 1.5). An observer standing outside the rotating frame of reference would witness the more complicated nutational motion of the spins.

1.12.2 Flip Angles

The angle (α) through which the spins are flipped from the z-axis into the transverse plane is referred to as the flip angle. It is the choice of amplitude, and duration (τ) of the applied field ($\mathbf{B_1}$) that determines the flip angle of the magnetisation.

$$\theta = \gamma B_1 \tau \qquad (1.15)$$

It is possible to obtain the same angle by applying a strong pulse for a short duration of time, or by applying a weak pulse for a longer period of time. If the entire $\mathbf{M_0}$ vector is flipped into the x–y plane by the RF pulse, then the pulse is referred to as a 90° RF pulse and the angle as a 90° flip angle. At this point: $\mathbf{M_{xy}} = \mathbf{M_0}$.

A 180° pulse would have twice the amplitude or twice the duration of a 90° pulse. The application of a 180° RF pulse inverts the net magnetisation vector by exciting the excess spins in the lower energy level into the upper energy level, without inducing phase coherence.

1.12.3 Partial Flip Angles

It is possible to flip the net magnetisation vector into the x–y plane by less than 90° simply by reducing the power and/or duration of the RF pulse. This results in the magnitude of $\mathbf{M_{xy}}$ being less than the original magnitude of $\mathbf{M_0}$:

$$M_{xy} = M_0 Sin\theta \qquad (1.16)$$

1.12.4 Free Induction Decay

Once in the x–y plane, the precessing net magnetisation induces a voltage and current in a receiver coil which is sensitive only to magnetic fields in the transverse plane. This induced current is the source of the signal for all MRI imaging.

A large signal is induced and detected immediately after a 90° pulse, as all the spins are in phase. This signal is known as the Free Induction Decay (FID) (Figure 1.6).

$$e^{-t/T2^*} Cos\omega t$$
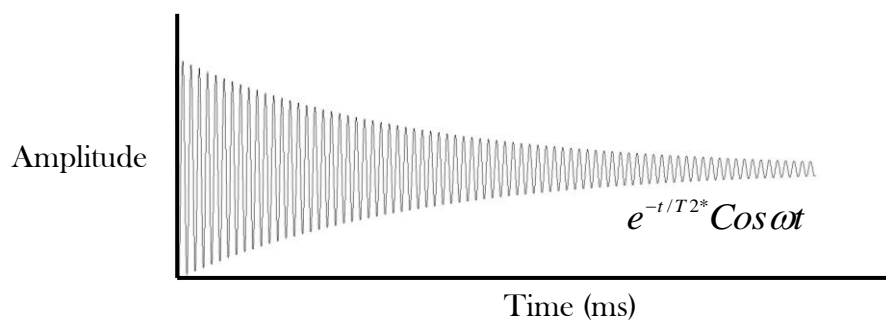
Figure 1.6 Left to its own devices the FID would quickly decay away

Left to its own devices, the FID would rapidly decay away to zero as described by the Bloch Equations (Appendix A). These macroscopic equations describe nuclear magnetisation as a function of time when T1 (1.10.8) and T2 (1.10.9) relaxation processes (Figures 1.7 and 1.8) are present.

1.12.5 T1 Relaxation

The T1 relaxation process is also known as the longitudinal or spin-lattice relaxation time and describes the recovery of the M_z component of the net magnetisation vector as it returns to its equilibrium position along the z-axis after the application of the RF pulse. To relax back into equilibrium, the spins have to transfer the energy gained from the RF pulse to the environment. This transfer of energy is not spontaneous and can only happen if the spins experience an oscillating magnetic field at or near the Larmor frequency. The rate of energy transfer depends on a molecule's natural motions (rotation, vibration and translation). Hydrogen, in the form of water, is a small molecule and therefore, moves quite rapidly. Larger molecules, such as fat molecules move more slowly. The T1 relaxation time reflects the relationship between the natural frequency of these molecules and the resonant or Larmor frequency. When these frequencies are similar, the T1 recovery of M_0 is rapid, when they are very different, the T1 recovery is slow. Hence different tissues exhibit different T1 recover curves (Figure 1.7).
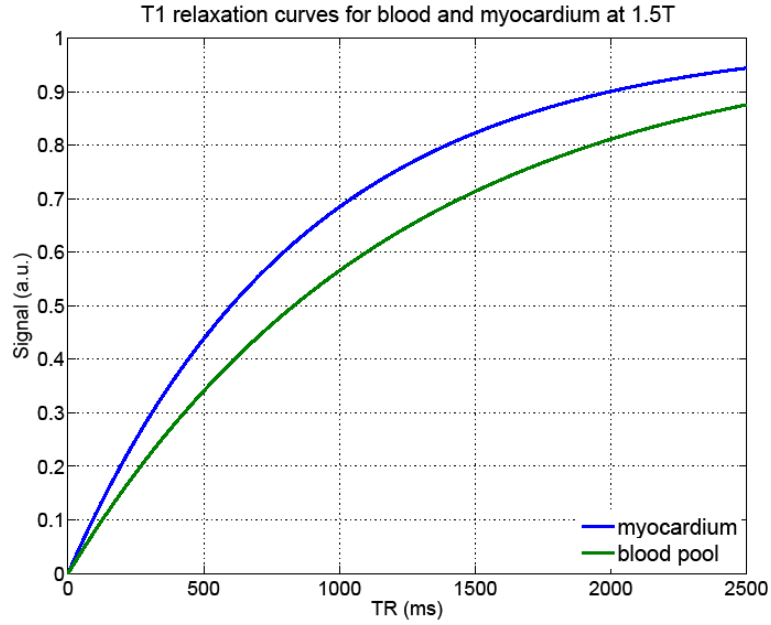
Figure 1.7 The T1 relaxation curves of blood pool of the heart and the heart wall (myocardium) at 1.5T

The equation that describes the T1 relaxation process as a function of time (t) is:

$$M_z(t) = M_0(1 - e^{-t/T1}) \quad (1.17)$$

The T1 relaxation process also governs the recovery of the net magnetisation vector after a 180° pulse.

$$M_z(t) = M_0(1 - 2e^{-t/T1}) \quad (1.18)$$

1.12.6 T2 Decay

The phase coherence witnessed immediately after the application of the RF pulse is short lived as the spins interact with each other. This loss of coherence results in the decay of the transverse magnetisation and ultimately, the loss of signal. Again, this process varies between tissue types with larger molecules,

such as fat, experiencing many static internal magnetic fields in the presence of $\mathbf{B_0}$ due to their chemical structure. The rate of decay of $\mathbf{M_{xy}}$ is governed by the spin-spin relaxation time (T2) of each tissue (Figure 1.8). The equation that describes T2 relaxation as a function of time is:

$$M_{xy} = M_{xy}(0)e^{(-t/T2)} \qquad (1.19)$$
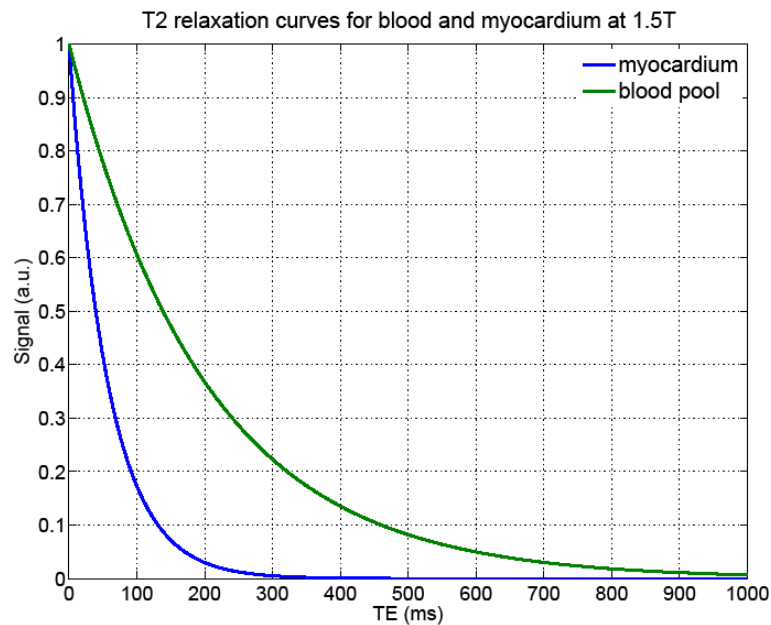
Figure 1.8 The T2 relaxation curves of the myocardial tissue and the blood pool of the heart at 1.5T.

T1 and T2 are exponential processes. In general, T2 decay is five to ten times more rapid than T1 recovery.

1.12.7 T2* Relaxation

T2* (t-two star) is a time constant that includes the additional dephasing effects that influence the decay rate of $\mathbf{M_{xy}}$, such as small magnetic field

inhomogeneities and magnetic susceptibility. T2* therefore, describes a quicker loss of signal than T2 and as a result, T2* is always smaller than T2:

$$1/T2^* = 1/T2 + 1/2\gamma\Delta B \quad (1.20)$$

The dephasing effects that are exclusive to T2* are reversible under certain circumstances. This reversal can be exploited in MR imaging methods [9].

1.13 Image Formation

Image formation in MRI works by defining the signal intensity in an array of pixels so that it corresponds to a three-dimensional co-ordinate system (x, y and z) within the patient. This is a challenging process in MRI as the signal originates from the entire object rather than a point source and is therefore, not simply a case of collimating the receiver coils.

In a highly homogenous magnetic field such as $\mathbf{B_0}$, identical spins in different locations will precess at the same frequency and as a result, the detected signal will contain no spatial information regarding their distribution. However, by distorting $\mathbf{B_0}$ with gradient fields, in a precise and controlled way, protons at different locations will precess at different resonant frequencies. This permits the signal amplitude to be measured as a function of frequency and phase whilst the density of protons in the tissue allows an image of spatial structure to be obtained.

1.13.1 Gradient Magnetic Fields

Gradients fields are small perturbations that have magnitude and direction and are represented as vectors. They are normally applied as pulses in any chosen direction or orientation using gradient coils. These gradient fields provide MRI with its three-dimensional capabilities. When applied in the x, y and z direction the gradient fields are represented by the symbols $\mathbf{G_x}$, $\mathbf{G_y}$, and $\mathbf{G_z}$ respectively. The isocentre of the magnet is the point where x, y, and z = (0, 0, 0). The magnetic field at this point is $\mathbf{B_0}$ and the resonant frequency is ω_0.

1.13.2 Slice Select Gradient

The strength of the gradient characterises the slope of the field as a function of its position along the axis. For a field gradient in the z direction:

$$B_z \, grad = G_z z \qquad (1.21)$$

The Larmor frequency of each spin is therefore dependent on its position along the axis, effectively dividing the patient into 2D slices Larmor frequencies (Figure 1.9):

$$(1.22)$$

$$\omega(z) = -\gamma(B_0 + G_z z) = \omega_0(0) - \gamma G_z z$$
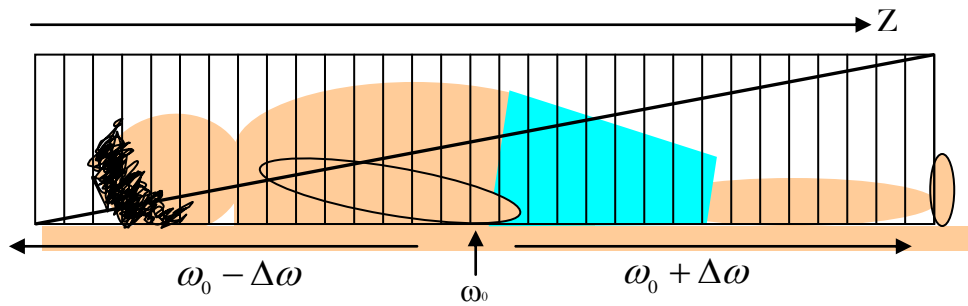
Figure 1.9 A slice select gradient is applied that effectively divides the patient into slices of varying Larmor frequencies.

The centre frequency of the RF pulse controls the location of the slice whilst the range of frequencies in the pulse controls the width. Protons either side of the selected slice will be resonating at higher or lower frequencies. However, the required frequency has to be present within the RF pulse's transmit bandwidth for resonance to occur, thus excitation only takes place close to the isocentre. This allows the position, orientation and thickness of the slice to be manipulated simply by adjusting the gradient or RF waveform properties.

1.13.3 Frequency Encoding

During imaging, a frequency encoding gradient is applied perpendicular to the slice select gradient. Once again the centre of the slice remains unaltered but the resonant frequency of the spins reduces to the left of the central point and increases to the right, thus creating columns of varying Larmor frequency within the slice.

The selected imaging slice is divided into voxels of spins

Apply G_z Gradient

Apply $G_x G_y$ Gradients

G_z

G_x

G_z
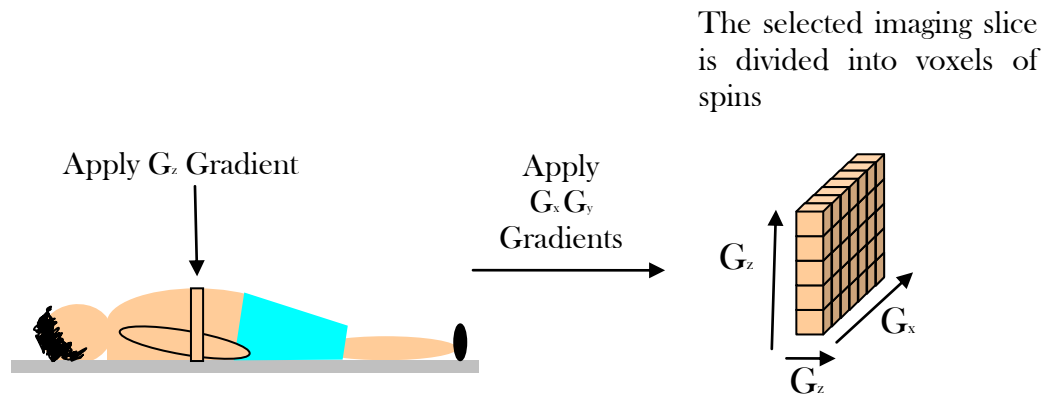
Figure 1.10 The signal is encoded in three directions (Gx, Gy and Gz) resulting in voxels of spins within the selected imaging slice.

1.13.4 Phase Encoding

The application of these two gradients is still not enough to ascribe a unique frequency to each column and row of protons. For this reason, the signal is encoded in terms of phase in the third direction. The phase encoding gradient induces a change in phase that is proportional to distance, effectively dividing the columns of spins into voxels, each with varying precessional speeds (Figure 1.10). When this gradient is switched off the spins revert to their original speeds but keep their phase encoding until either another gradient is applied or the MR signal decays.

Gradients are applied with or after an RF pulse. They can be applied individually or in combination to create transverse, sagittal or coronal, oblique or double oblique slices. During imaging, spatial localisation in the phase encoding direction requires many steps. Each step is performed with an

incremental change in gradient amplitude so that the protons in the same row have the same phase but the protons in the same column have different phases.

The gradient system of a modern scanner comprises of a gradient amplifier and several gradient coils, each of which is positioned around the bore of the magnet. The z gradient (G_z) is provided by a Maxwell pair (Figure 1.11), whilst the x and y gradients are provided by a Golay pair
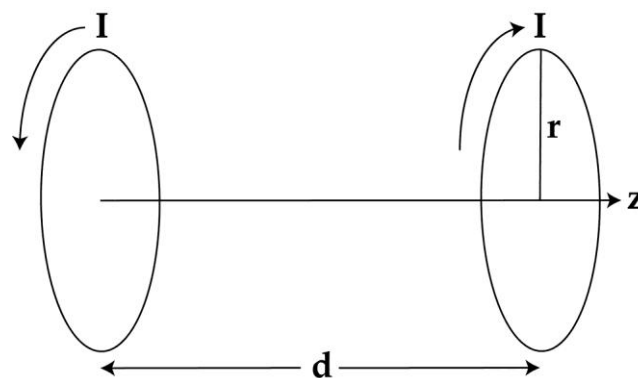
Figure 1.11 A Maxwell coil pair is the most efficient choice for producing a z-gradient (G_z).
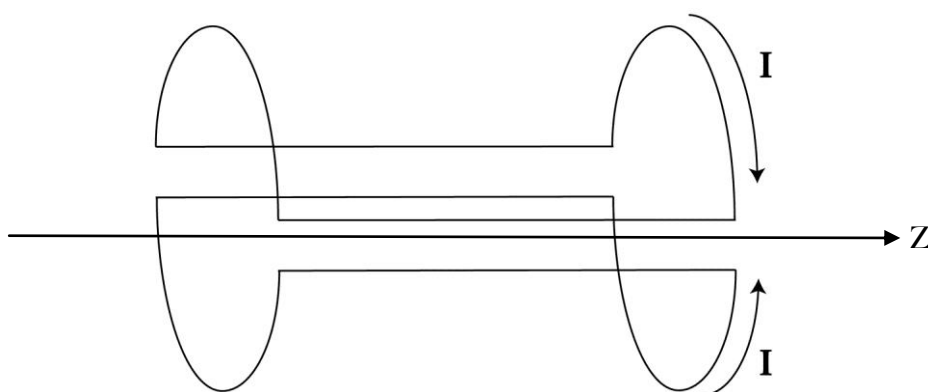
Figure 1.12 The preferred design for a transverse gradient (G_x or G_y) is the Golay pair.

Modern scanners use shielded gradient coils where secondary coils are used to cancel out undesired fields from the primary coils.

Gradient strength is a measure of the change in field strength over distance and is directly proportional to the applied current in the coil. Gradient rise time is a measure of the rate of change of field generated when the gradients are switched on and off. The gradient strength divided by the rise time gives the slew rate of the gradient coils. Slew rates refer to the speed with which the gradients can be turned on and off. Higher gradients are desirable as they allow thinner image slices or smaller fields of view (FOV) to be obtained without changing any other measurement parameters.

Gradient linearity is another important factor in today's high end scanners as gradient non-linearity can lead to image distortion and signal loss. Thus, manufacturers strive to restrict gradient deviations to within 5% of their desired value.

1.13.5 Repetition Time

Typical MR experiments use a series of pulsed RF energy. The repetition time (TR) between successive RF pulses should be long enough to allow additional absorption during the next RF pulse and to prevent the spin system from becoming saturated, but insufficient for complete T1 relaxation.

1.13.6 Echo Time

Fundamental limitations in the electronics of an MR system prevent a measurement of the signal immediate after the application of the RF pulse. Hence, the signal is measured after a short time period, known as the time to echo (TE). TR and TE are intimately related to T1 and T2 respectively. However, unlike T1 and T2, TR and TE can be adjusted and controlled by the operator.

1.13.7 Biological Parameters

T1, T2, T2* and proton density values are inherent properties of biological tissue. Generally, T1 lengthens with increasing field strength as the energy exchange between the spins and their surroundings is less efficient at higher frequencies. Field strength also impacts on T2* values as higher fields have an increased influence on intrinsic susceptibility changes in tissues.

1.14 Pulse sequences

A pulse sequence is basically an MRI software program that has the timing parameters TR and TE embedded within it. A pulse sequence diagram (Figure 1.11) is a timing diagram that illustrates the timings of the RF pulses, gradients and echoes. Pulse sequences control all hardware aspects of an MRI imaging session. Many of the advances in CMRI have resulted from pulse sequence developments rather than hardware updates or alterations.

Pulse sequences can be used to accentuate or suppress different tissues, reduce imaging times, produce spatial localisation and minimise or avoid artefacts.

Sequences can be selected that are sensitive or insensitive to dynamic parameters such as flow, contrast uptake or perfusion, offering exceptional versatility.

There are two main sequence types in MRI, known as Spin Echo (SE) and Gradient Echo (GE).

1.14.1 Spin Echo

The spin echo (SE) technique uses a 90° excitation pulse to flip the net magnetisation vector into the x–y plane where the spins start to precess and de-phase. A short time later (TE/2), a 180° refocusing pulse is applied that rotates the magnetisation about the axis (Figure 1.15). Spins continue to de-phase; however, as the magnetisation has been rotated, the spins are now refocusing. This rotation eliminates the de-phasing effects caused by magnetic field inhomogeneities resulting in the creation of an echo that is dependent on T2 decay. Multiple RF refocusing pulses can be applied after the 90° RF excitation pulse, as long as there is sufficient transverse magnetisation. This creates a train of spin echoes.
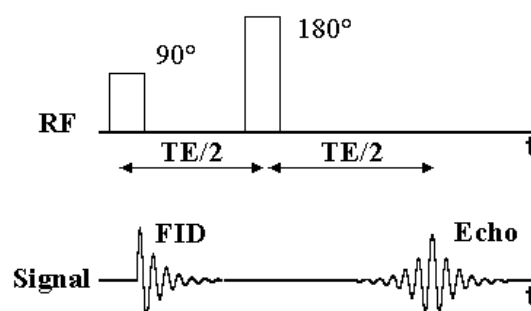
Figure 1.15 The spin echo pulse sequence has a 90° excitation pulse followed by 180° refocusing

1.14.2 Spin Echo – T1 Weighted Images

Image contrast can be manipulated in SE imaging simply by varying the TR and TE values. The selection of a long TR (e.g. 2000ms) will allow the complete (or almost complete) recovery of the T1 curves of the different tissues. Conversely a short TR (e.g. 300ms) will limit the time allowed for the longitudinal magnetisation vector to fully recover and result in the incomplete T1 recovery for some or all tissues. This results in the contrast in such images being dependent on the T1 characteristics of the different tissue types (Table 1.1). Thus, these images are described as being T1 weighted.

1.14.3 Spin Echo – T2 Weighted Image

Similarly, the relaxation (dephasing) rates of the transverse magnetisation vector can provide T2 weighted images in SE if a long TR and a long TE (e.g. 80-140ms) are selected (Table 1.1). The long TR allows the complete recovery of the longitudinal magnetisation vector and the long TE provides sufficient time for T2 relaxation to happen. These T2 weighted images depend on the T2 relaxation rates of the different tissues only as the application of the 180° refocusing pulse at TE/2 refocuses the dephasing spins and cancels the dephasing effects of static magnetic field inhomogeneities. Tissues with a long T2 provide a stronger signal than tissues with a short T2 (e.g. 10-20ms).

Table 1.1 The contrast in SE images is determined by the choice of TR and TE values

Spin Echo Imaging	Short T2	Long T2
Short TR	T1 Weighted	X
Long TR	Proton density	T2 Weighted

1.14.4 Spin Echo – Proton Density Image

Where the operator selects a long TR and a short TE, the T1 and T2 dependence of these images is insubstantial. For this reason, image contrast is dictated by the density of protons in the different tissue types. Tissues with a high Hydrogen content will appear bright whilst tissues with a low Hydrogen content will appear dark.

1.14.5 Gradient Echo

Gradient echo (GE) pulse sequences differ from SE pulse sequences in that they can use an excitation pulse of $< 90°$ to produce an echo. This partial flip angle means that at the time point TE/2, a large component of the net magnetisation vector is lying in the z-axis. Applying a 180° pulse at this point would invert this magnetisation ($\mathbf{M_z}$) into the negative z-axis. This is not desirable as a long TR would be required for $\mathbf{M_z}$ to fully recover. Alternatively, measuring the FID would not provide the time interval essential to spatially encoding the signal. Hence, in GE the FID is de-phased and then re-phased at a later time using a refocusing gradient (Figure 1.16). The gradient reversal in GE sequences refocuses only the spins that have been de-phased by the action of the gradient

itself and not those de-phased by magnetic field inhomogeneities. Hence, GE image contrast is dictated by T2*.
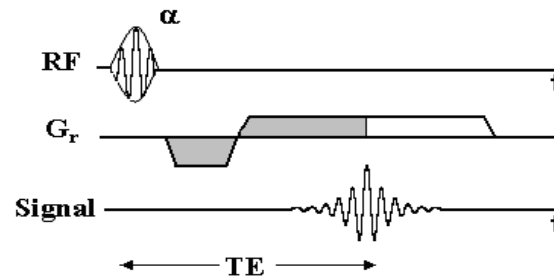
Figure 1.16 The gradient echo pulse sequence uses a partial flip angle of <90° and a refocusing gradient.

As only one RF pulse is applied in GE, it is possible to record the signal more quickly than in SE, resulting in a shorter TE. Partial flip angles also allow the use of shorter TRs. Consequently, GE images are ideal for cardiac imaging as their short TRs and reduced flip angles allow faster imaging times, significantly reducing motion related artefacts. GE sequences are commonly referred to as white-blood imaging, as generally blood and fat appear white in these images.

The signal weighting in a GE image depends on the TR, TE and flip angle. The higher the flip angle, the more T1 weighted the image will be (Table 1.2). The shorter the TE, the less T2* weighted the image will be. In addition to this, there is an optimal combination between TR and flip angle for maximum MR signal. The optimal angle is known as the Ernst angle (α_E) and is calculated from the TR and T1 values:

$$\cos \alpha_E = \exp\left(-\frac{TR}{T1}\right) \qquad (1.22)$$

As the TR is always assumed to be short for a GE sequence, it has much less of an effect on image contrast. By selecting a small flip angle the magnetisation will be almost completely recovered, so there will be very little difference in T1 recovery curves (Table 1.2).

Table 1.2 The contrast in GE images is determined by the choice of flip angle and TE

Gradient Echo Imaging	Short TE	Long TE
Small flip (< 40°)	PD weighted	T2* weighted
Larger flip (>50°)	T1 weighted	X

1.14.6 Anatomy Scans

T1 weighted images usually have excellent contrast making it easy to differentiate between fluids, water-based tissue and fat. For this reason, they are commonly referred to as anatomy scans.
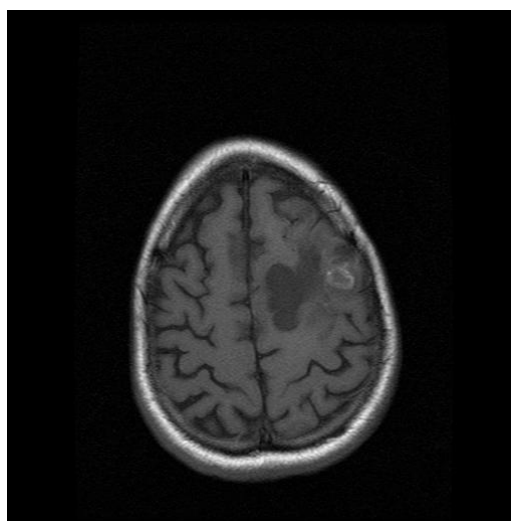
Figure 1.13 A T1 weighted image of the brain shows excellent contrast between normal and abnormal tissues

1.14.7 Pathology Scans

Fluids have the highest intensity in T2 weighted images, showing up very brightly against the darker soft tissue. It is possible to differentiate between normal and abnormal fluids (such as oedema) in an image as they have different T2 relaxation rates and hence different signals. For this reason, T2 scans are considered pathology scans. Most cardiac images are acquired using a ratio of T2 to T1 (Chapter 5).
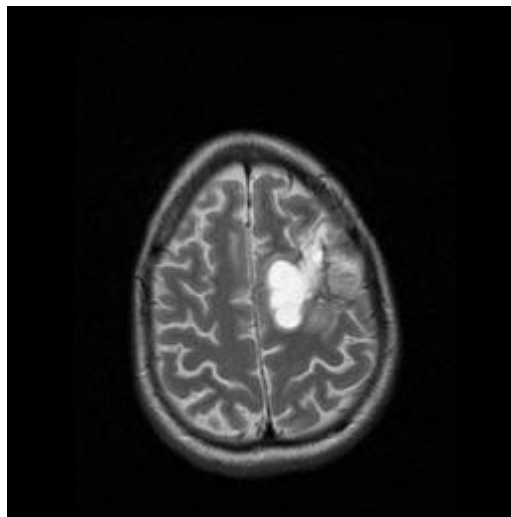
Figure 1.14 A T2 image of the same brain highlights abnormal fluid

1.14.8 Proton Density Scans

Proton density images are dependent primarily on the concentration of mobile hydrogen atoms within the imaging volume. The variation of proton densities in different tissues provides the range of signal intensities and hence, image contrast.

1.15 Coils

In addition to the solenoid coil and gradient coils mentioned previously in this chapter, a body coil and shim coil sets are also built in to the bore of the magnet.

1.15.1 Body Coil

The body coil surrounds the patient in the magnet bore. The main function of this coil is to transmit the RF pulse for all scans and to receive the MRI signal when large parts of the body are being imaged.

1.15.2 Shim Coil Sets

Shim coil sets are built into all state-of-the-art MRI systems. These coils are used to compensate for undesirable field distortions in a passive or active manner. Passive coils consist of shim plates (pieces of metal) that correct for field distortions. Active coils are comprised of loops of wire that a current is passed through to produce supplementary magnetic fields. Shim coils are essential for cardiac imaging at 1.5T and 3.0T as they provide improved field homogeniety across the heart. This will be discussed in Chapter 7.

Various other radio frequency coils are used in MRI to transmit energy and to receive signals. These coils are placed on or around the region of tissue to be scanned. They comprise of transmit receive coils, receive only coils and transmit only coils.

1.15.3 Surface Coils

Insulated surface coils are placed directly on top of the patient's clothing to ensure that the receiver is as close as possible to the MR signal. Surface coils are commonly used in MRI as their close proximity to the patient limits the volume from which noise is detected thus providing good SNR for superficial tissue.

1.15.4 Phased Array Coils

Phased array coils consist of an array of surface receiver coil elements with known sensitivity profiles whose signals are combined to provide a uniform signal intensity over a volume that is in excess of each of the smaller individual coils (Figure 1.17). Phased array coils have a superior SNR to larger coils covering the same area, as the design of these coils ensures that the noise from coil to coil is largely uncorrelated.
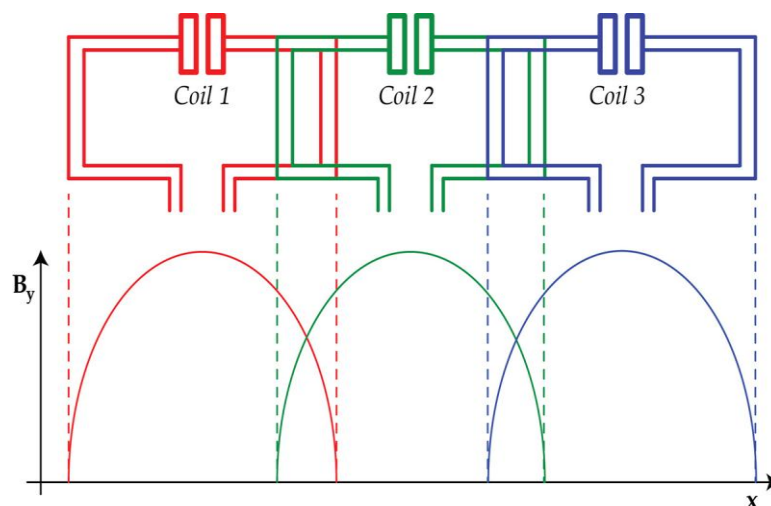
Figure 1.17 Phased array coils are designed so that the noise from coil to coil is largely uncorrelated.
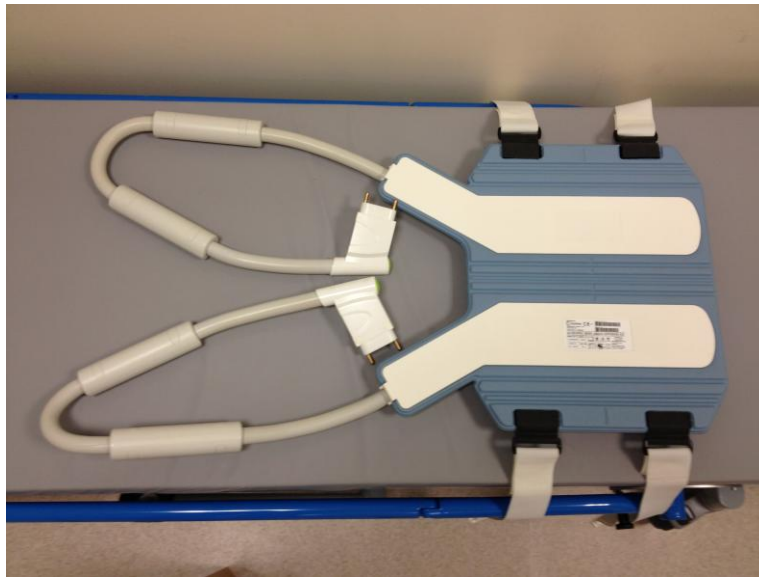
Figure 1.18 A 32 channel phased array cardiac coil

This technology is ideal suited for cardiac imaging as the array can be wrapped around the patient's torso in a bid to obtain optimal images of the heart (Figure 1.18).

1.16 K-Space

Applying gradients in MRI changes the frequency across the patient as a function of position effectively taking the patient from a physical space into a frequency space. Hence, the signal we obtain is a sum of sine waves that add to create a rapidly changing continuous voltage in our receiver coil. This complex signal originates from every voxel in the image.
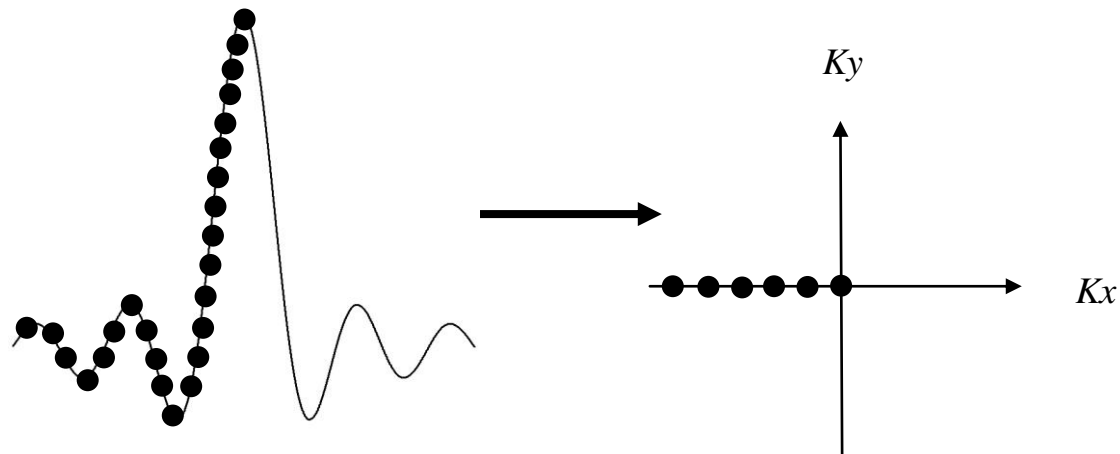
Figure 1.19 The signal is digitised by sampling the voltage across the echo. Each echo fills a single line in the k-space array.

The signal is digitised by sampling the voltage at each point across the echo using an analogue to digital converter (ADC). This allows the amplitude and phase of the signal to be determined as a function of time. Each of these points is represented by a complex number that includes a real and `imaginary part. Rather than directly expressing position, the points indicate the amount of spatial encoding that has taken place at that point, with each point being identified by its value and location, which are equivalent to the amplitude and the frequency of a sinusoid respectively.

In conventional imaging, each excitation pulse provides a single echo that is sampled to fill a single line in k-space (Figure 1.19), with the number of samples acquired across the echo in the x direction determining the number of pixels in the x direction. The number of echoes sampled determines the number of lines in the y direction, which in turn determines the number of

pixels in the y direction. Hence, filling k-space conventionally is a time consuming process as an image with 128 pixels in the y direction would require 128 echoes each with a different phase encoding step.

It would be impossible to create an image before the gradient fields are applied as the uniform precession of all the spins would simply create a uniform sine wave that would superimpose as one dot in K-space. The effective position in k-space is determined by the gradient amplitude and duration as well as the gyromagnetic ratio.

Applying a gradient to de-phase the spins creates a temporary shift in frequency across the sample, making the phases of the protons change as a function of position. The spins at the centre of k-space effectively do not experience a gradient and therefore, they do not experience a frequency shift (ω_0), whereas those over towards the edges of k-space experience the greatest shift
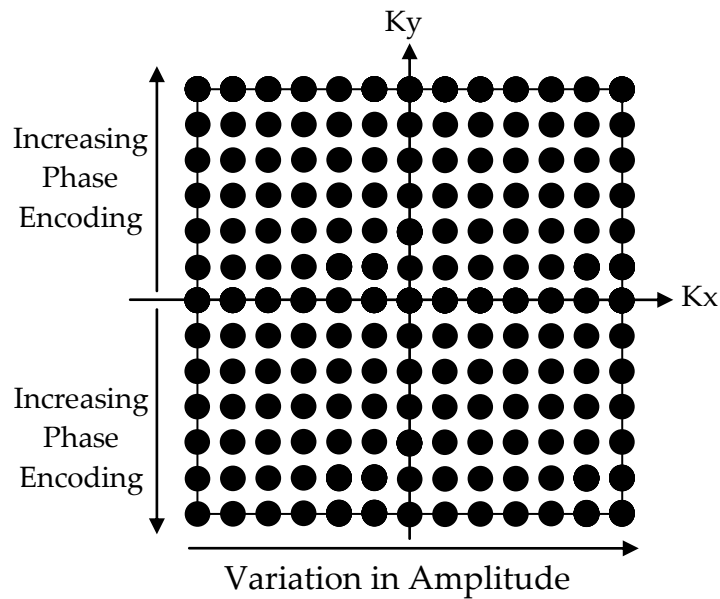
Figure 1.20 Each point in k-space is represented by a complex number that contains a real and an imaginary part and represents the spatial encoding that has taken place at that point.

As the middle point of k-space does not experience a gradient, every proton is in phase, providing a very strong constant signal across the image space. When a mathematical operation [known as a Fourier transform (FT)] is performed on the k-space array to produce the final image, this one point in k-space creates a sheet of uniform intensity that determines the intensity of every pixel in the image. The next point along the x-axis in k-space creates a second sheet of intensity that has an oscillation along the x-axis but is constant in y. This additional sheet is added to the first sheet to increasing the intensity across the whole image, improving the spatial resolution.

The centre of k-space provides the image with contrast and the edges of k-space provide the image with high frequency definition. Frequency is proportional to

distance from the centre of k-space. Removing high frequency data would result in a blurred image with normal contrast.

The desired spatial resolution of the final image (Figure 1.21) is specified by selecting the field of view (FOV) and the number of phase and frequency encoding steps. This in turn determines the extent of the k-space array. The more tightly packed k-space is, the larger the field of view (FOV). Conversely, if the echo is loosely sampled a small field of view is obtained; however the pixel size, contrast and resolution are the same.
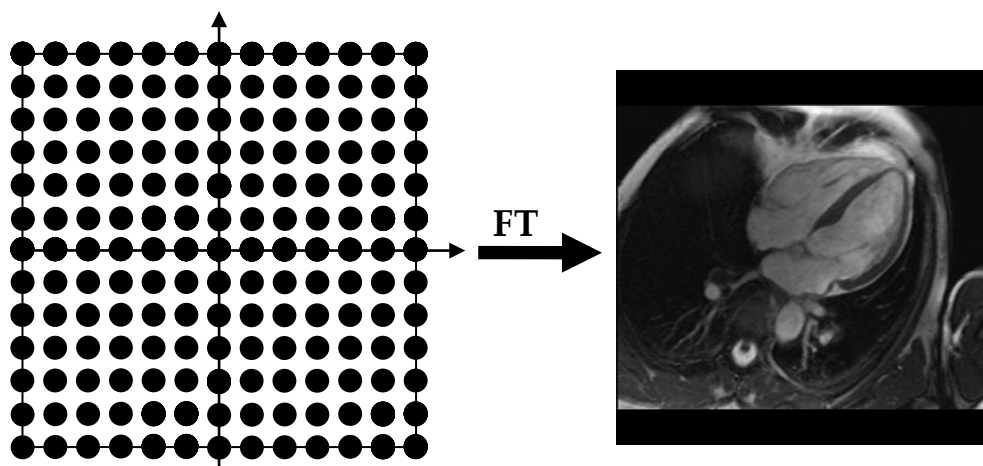
Figure 1.21 A 2-D Fourier Transform is performed on the k-space array to produce the final image.

1.17 SAR limitation

The specific absorption rate (SAR) is a measure of the rate at which energy is absorbed by tissue when exposed to a radiofrequency electromagnetic field. More precisely, it is a measure of the energy deposited by a radiofrequency field in a given mass of tissue. The SAR is limited by the Medicines and Healthcare Regulatory Agency (MHRA) guidelines [10], which state that the

SAR must not exceed 10 W/kg of tissue for the head and trunk or 20 W/kg for the limbs over any 6-minute period. The SAR value is affected by many parameters such as the flip angle, amplitude of the RF pulse, selected protocol parameters, the subject's weight and region of exposure, and the radiofrequency coil. To prevent limits being exceeded, the scanner will slow imaging or suggest that a parameter is reduced, such as increasing the TR or reducing the number of slices to be acquired.

1.18 Cardiac Magnetic Resonance Imaging

Initially, CMRI failed to gain widespread acceptance due to the challenges associated with imaging the beating heart using a complicated technique that is inherently sensitive to patient/organ motion. Despite this, CMRI remained an area of intense interest within the cardiac community due to its unique potential to provide an accurate, and reproducible, full cardiac assessment of morphology and function, perfusion and viability, valvular disease and coronary artery stenosis, all within a single imaging session. The sustained development of CMRI hardware and software techniques discussed in Chapter 3 of this thesis have resulted in a paradigm shift in CMRI's clinical potential, allowing it to fulfil its promise beyond the limitations of other well established cardiac imaging modalities.

1.19 Other Techniques and their Limitations

Although cardiac magnetic resonance imaging is now well-established and has growing popularity within the radiology and cardiology communities, other imaging modalities are presently utilised more frequently in clinical practice.

1.19.1 SPECT and PET

Single photon emission computed tomography (SPECT) and positron emission computed tomography (PET) are imaging techniques that work on the same basic principles. Patients are injected intravenously with a labelled radioisotope, which travels through the coronary arteries to the myocardium where it is absorbed. The decay rate of the isotope is then measured using either a gamma camera or PET scanner, providing a functional picture of the blood supply to the myocardium.
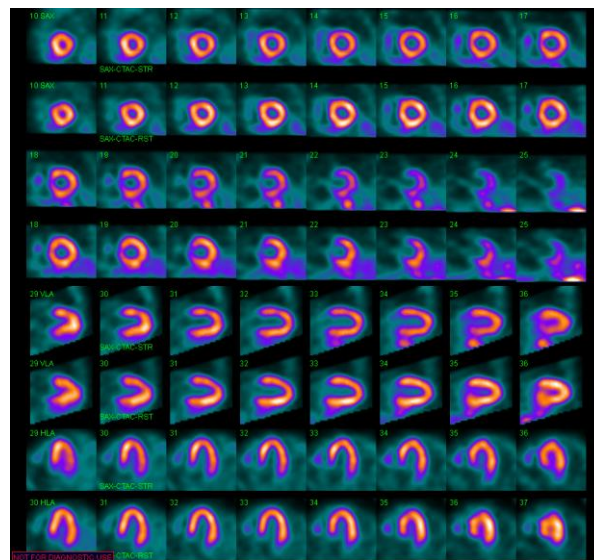
Figure 1.22 A series of SPECT images in three planes showing the uptake of a radioisotope in the heart muscle.

Single Photon Emitted Computed Tomography has become the most popular imaging technique for the diagnostic work-up of patients with coronary artery disease. Conversely, cardiac PET imaging initially failed to become widely established in the United Kingdom because of its requirement for isotopes from restricted sites with a cyclotron. However, this situation is now changing as the required isotopes become more available.

In comparison to CMRI, SPECT and PET are immediately limited by their use of ionising radiation. A further limitation is the difficulty in assigning cardiac wall boundaries when coronary arteries are narrowed or occluded due to the reduced blood flow and hence reduced isotope count in the area fed by the diseased vessel (Figure 1.22).

1.19.2 Computed Tomography

Computed tomography (CT) is an imaging modality that is known to provide accurate and reproducible images [11, 12] of the heart and coronary arteries (Figure 1.23). It does this using a fan-shaped beam of x-rays that pass through the patient to reach detectors. Subsequently, the radiation exposure to the patient is non-trivial. This naturally restricts the use of CT for longitudinal studies designed to chart the progression of cardiac disease-related changes.

A further restriction of CT is that images can only be obtained in sagittal or coronal planes.

Figure 1.23 A CT image of the four chambers of the heart.

1.19.3 Echocardiography

Echocardiography (echo) is the modality of choice for the detection of heart-wall motion abnormalities that are often the earliest manifestations of coronary blood flow restrictions. Echo is a non-ionising technique, which uses a transducer to create a beam of very high frequency sound (ultrasound) waves that are transmitted into the patient and reflected back. The shape, size, density and motion of all objects lying in the path of the beam are then reconstructed on a screen as an image (Figure 1.24).
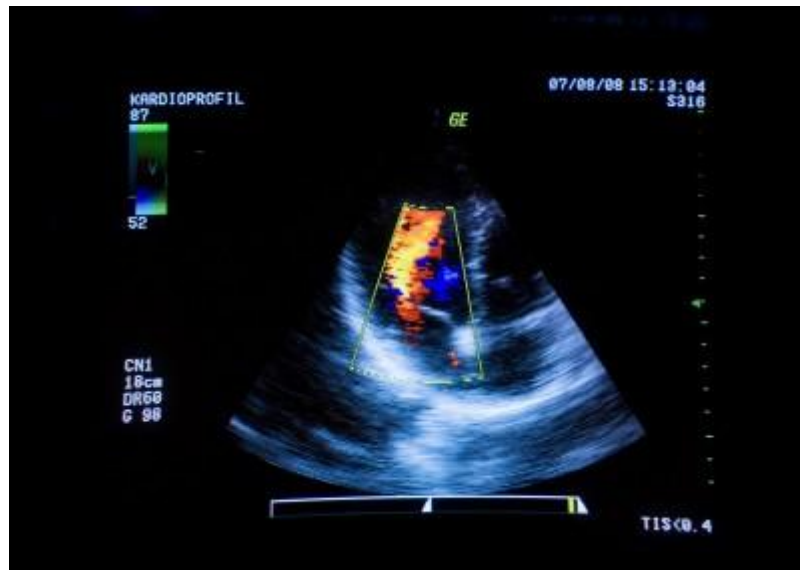
Figure 1.24 An echo image of the heart.

In comparison to CMRI, echo has a number of limitations, the most significant of which are; a significant number of patients (15–20)% do not have adequate acoustic windows to visualise the whole of left ventricle [14], also echo is operator-dependent, and the geometric assumptions made when calculating ventricular and atrial volumes from two-dimensional images can result in large errors [14].

1.20 The Advantages of Cardiac Magnetic Resonance Imaging

CMRI is superior to the other imaging modalities as it is non-ionising and non-invasive. It provides three-dimensional, high-resolution images that have excellent contrast between air, fat, muscle, and blood, without geometric or acoustic window limitations. A further advantage of CMRI is its unique capacity to accentuate or suppress specific tissues (Figure 1.25) simply by choosing the correct imaging sequence. It is CMRI's opulence in terms of

techniques, plus its ability to provide the clinician with a wide range of diagnostic information in a single imaging session that provides it with such an advantage over all the other competing modalities.
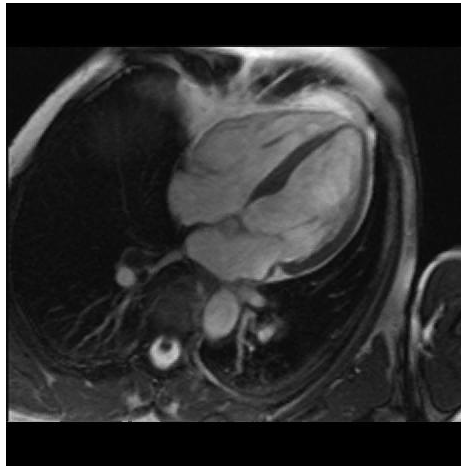
Figure 1.25 A CMR image of the four chambers of the heart.

1.21 The Limitations of Cardiac Magnetic Resonance Imaging

The main limitation of CMRI is the relatively lengthy acquisition times. This can be particularly problematic for very young, old, or infirm patients as they are required to remain motionless and breath-hold throughout each acquisition. A surprisingly small number of patients are too claustrophobic to enter the bore of the magnet, but an increasing number are too large. Manufacturers are responding to the mounting obesity problem by producing systems with 70cm diameter bores (in comparison to the current 60cm), which offer similar field homogeneities to that of the standard systems.

In addition to these limitations, patients presenting for CMRI with metal fragments or some medical implants may be considered unsuitable for imaging

For example, ferromagnetic materials act like dipoles in a magnetic environment. Hence the magnetic field produces a torque to align the dipole with the field. This torque is substantial at high fields.

$$Torque \approx B^2 \, \theta \qquad (1.23)$$

where θ is the angle from the z-axis of the dipole to the z-axis of the main magnetic field.

References

1. University Hospitals of Leicester. How the heart works. Anatomy and physiology; 2010. Available from: http://www.activateyourheart.org.uk/How-The-Heart-Works/AP.aspx (cited 25 April 2011).

2. World Health Organization. Cardiovascular diseases (CVDs); 2011. Available from: http://www.who.int/mediacentre/factsheets/fs317/en/index.html (cited November 2011).

3. De Backer G, Ambrosioni E, Borch-Johnsen K, Brotons C, Cifkova R, Dallongeville J et al. European guidelines on cardiovascular disease prevention in clinical practice. *European Heart Journal* 1998; **19**: 1434–503.

4. Arrighi J. Nuclear probes for assessing myocardial viability in heart failure. *Heart Failure Clinics* 2006; **2**:129–43.

5. Sharma S, Raman S, Sun B, Sai-Sudhakar C, Firstenberg M, Sirak J et al. Anterior wall viability and low ejection fraction predict improvement after CABG. *Journal of Surgical Research* 2010; 171: 416–21.

6. Haacke EM, Brown RW, Thompson MR, Venkatesan R. *Magnetic Resonance Imaging, Physical Principles and Sequence Design.* New York: John Wiley & Sons, 1999.

7. McRobbie DW, Moore EA, Graves MJ, Prince MR. *MRI from Picture to Proton.* New York: Cambridge University Press, 2006.

8. Sutton R, Kanal E, Wilkoff BL, Bello D, Luechinger R, Jenniskens I, et al. Safety of magnetic resonance imaging of patients with a new Medtronic EnRhythm MRI SureScan pacing system: clinical study design 2008. *Trial*; **9: 689.

9. Hahn EL. Spin echoes. *Physical Review* 1950; 80: 580–94.

10. Medicines and Healthcare Regulatory Agency (MHRA) guidelines [mhra.gov.uk 26/04/12].

11. Neubauer S. *MRI and CT.* Oxford University, UK 2007; Elsevier.

12. Raman SV, Shah M, McCarthy B, Garcia A, Ferketich A. Multi-detector row cardiac computed tomography accurately quantifies right and left ventricular size and function compared with cardiac magnetic resonance. *American Heart Journal* 2006; **151:** 736–44.

13. Assomull SK, Cannell TM, Prasad SK. CMR assessments of myocardial infarction and post infarct complications. *Coronary Artery Disease* 2005; **16**: 373–8.

14. Hudsmith LE, Cheng ASH, Tyler DJ, Shirodaria C, Lee J, Petersen SE, et al. Assessment of left atrial volumes at 1.5 Tesla and 3 Tesla using FLASH and SSFP cine imaging. *Journal of Cardiovascular Magnetic Resonance* 2007; **9**: 673–9.

2. The Human Heart
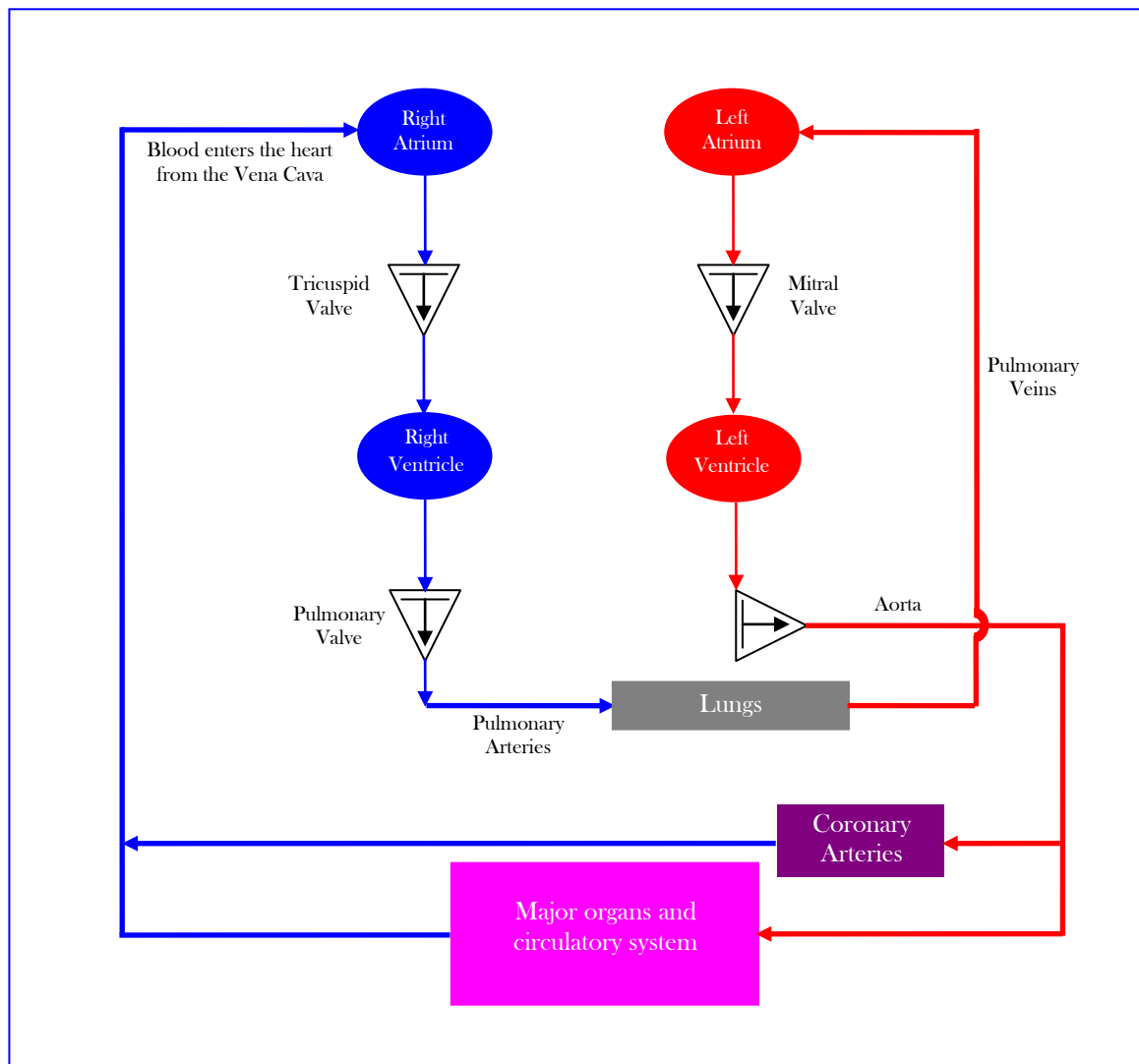
A healthy human heart is a thick, muscular, conical-shaped organ that is slightly larger than a clenched fist and normally weighs between 200g and 400g [1]. It is anchored in the mediastinal space of the thoracic cavity by an extremely tough, protective, fluid filled sac known as the pericardium (Figure 2.1).
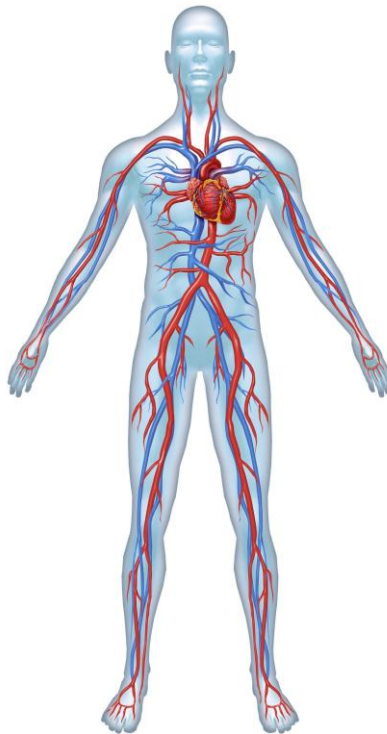
Figure 2.1 The cardiovascular system with the heart anchored in the mediastinal space of the thoracic cavity

2.1 The Chambers of the Heart

The heart consists of four main chambers known as the left and right atria and the left and right ventricles (Figure 2.2). The atria of the heart are principally blood receiving chambers whilst the ventricles of the heart are powerful pumps. A wall known as the septum separates the right side of the heart from the left side, and each chamber is closed off by a one-way valve.

The Right and the Left Artia

The Right and the Left Ventricles
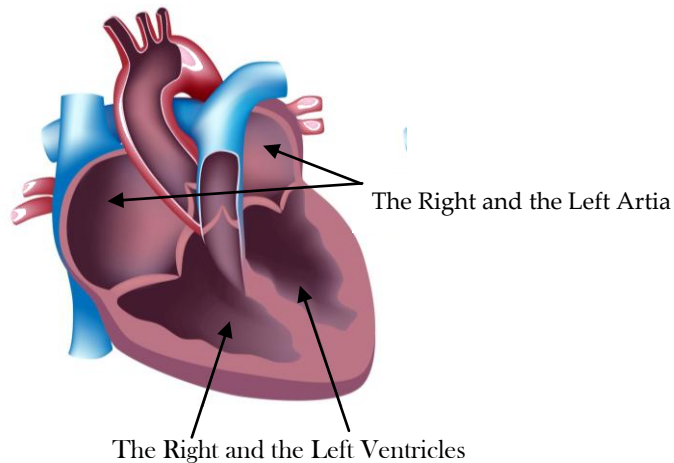
Figure 2.2 This heart consists of four main chambers: the left and right atria and the left and right ventricles.

2.2 The Valves of the Heart

Each valve has a set of flaps or cusps that work in a synchronised manner; opening when the pressure behind them builds up, and closing once blood has passed through them, alleviating the pressure. This simple system ensures blood flows through the heart in a forward direction. The valves on the left side of the heart are known as the mitral and aortic valves, whilst those on the right side of the heart are known as the tricuspid and pulmonary valves (Figure 2.3). The valves and the inner surface of the chambers are lined by a smooth layer of cells (membrane) known as the endocardium.
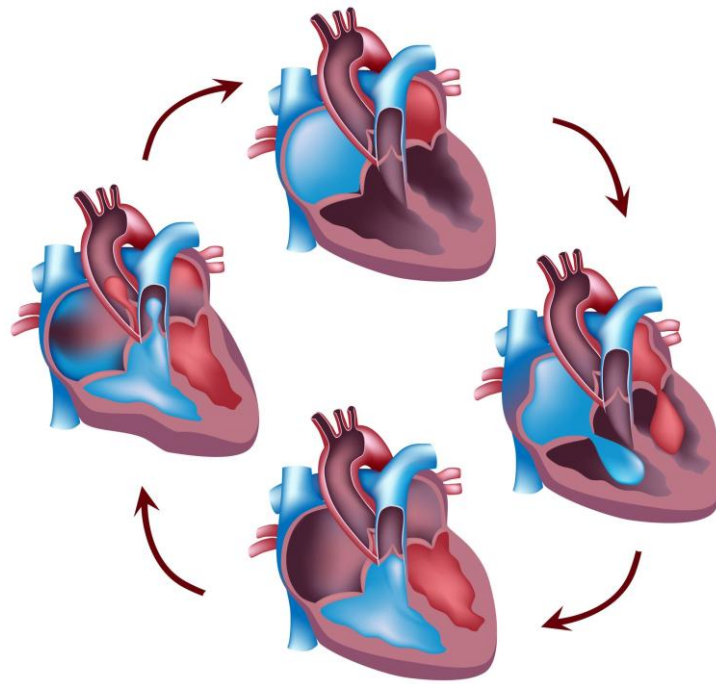
Figure 2.3 The valves of the heart work in a synchronised manner ensuring that blood flows in a forward direction through the heart.

2.3 The Papillary Muscles

The papillary muscles of the heart are attached to the atrio-ventricular valves by the chordae tendinae. These muscles prevent the regurgitation of blood within the cardiac chambers by bracing the valves against increasing pressure; thus limiting their movement (Figure 2.4). There are three papillary muscles in the right ventricle and two in the left.
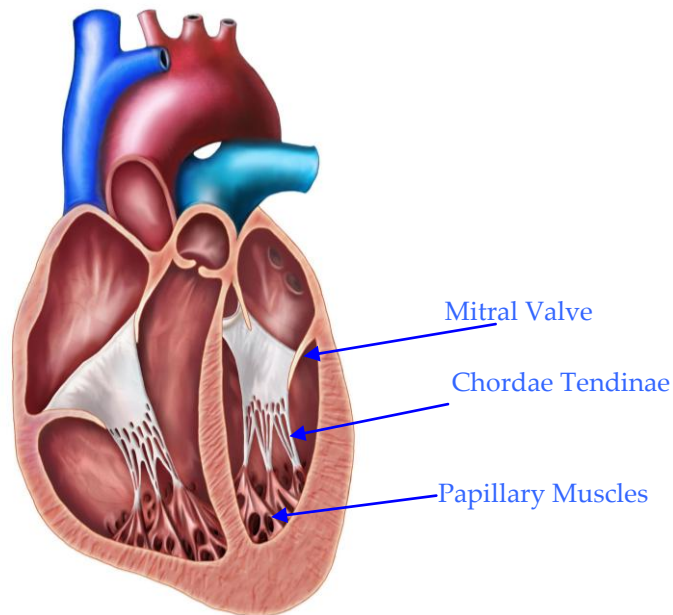
Figure 2.4 The papillary muscles are attached to the valves of the heart by the chordae tendinae

2.4 The Myocardium

The outer layer of the heart consists mostly of connective tissue and fat and is known as the epicardium. The heart walls are positioned between the epicardium and the endocardium and consist mainly of a layer of cardiac muscle known as the myocardium, which is responsible for the contraction and relaxation of the heart. In a healthy heart, the left ventricular myocardium is considerably thicker than that of the right ventricular myocardium.

The cells that make up the myocardium (myocytes) differ from other muscle cells found in the body in that they are lightly striated, have a single nucleus (Figure 2.5) and are involuntarily controlled [2].

Figure 2.5 The cells that make up the myocardium are lightly striated and have a single nucleus.

2.5 Path of Blood through the Heart

Deoxygenated blood enters the right atrium of the heart and flows in a forward direction to reach the right ventricle. When the ventricle is full, the tricuspid valve snaps shut and the ventricle contracts. This forces blood forwards into the lungs, via the pulmonary valve and arteries. Once in the lungs, carbon dioxide is efficiently removed and replaced with oxygen. The blood is then pumped back into the left atrium of the heart, via the pulmonary veins, before flowing into the left ventricle. When the ventricle reaches capacity, the mitral valve snaps shut and the ventricle contracts (Figure 2.6). The oxygen-rich blood is forced out of the ventricle, via the aortic valve. It flows through the aortic arch (Figure 2.7) and into the descending aorta to be distributed to the rest of the circulatory system. Under normal physiological conditions, the volume of blood pumped out of the right atrium at the start of this process is equal to the volume of blood returned to it via the circulatory system [3].
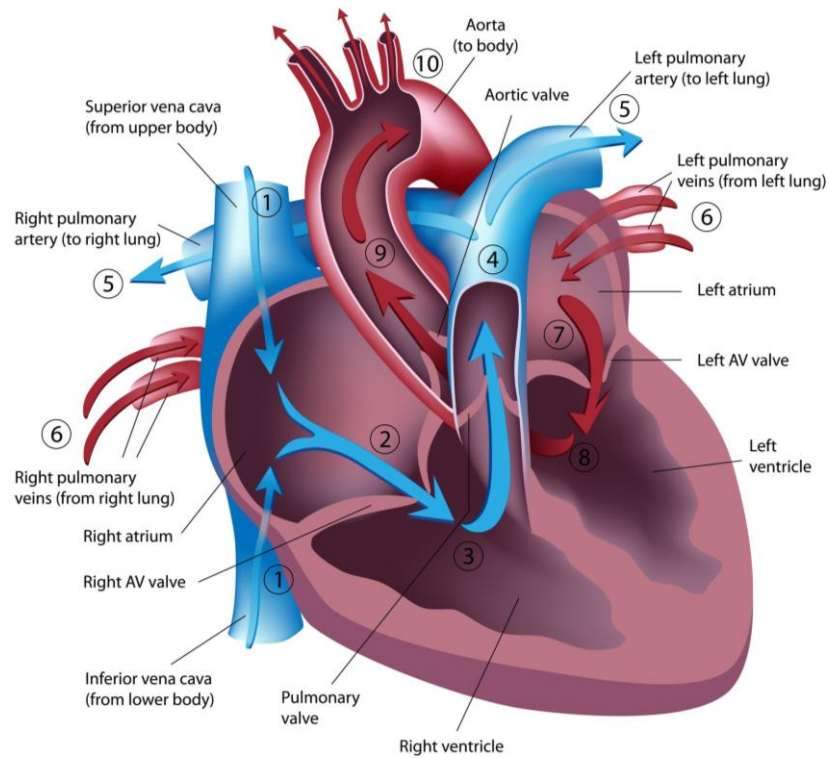
Figure 2.6 The path of blood through the heart (1–10).
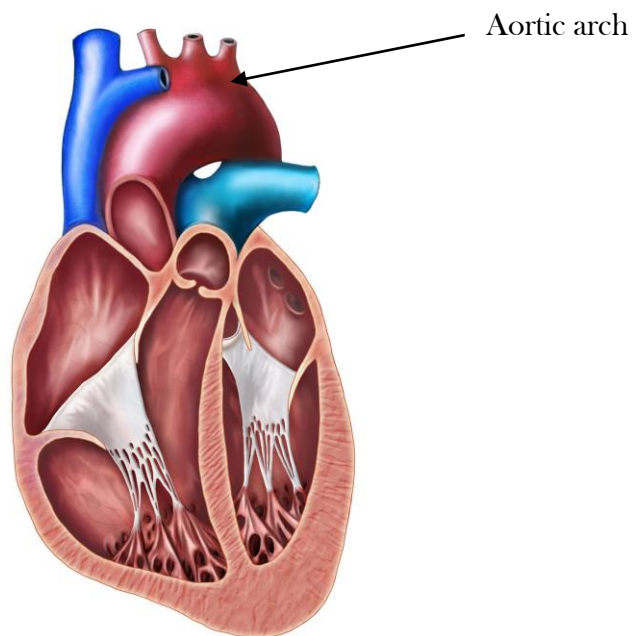
Figure 2.7: Blood leaves the heart through the aortic arch.

2.6 The Coronary Arteries

The first vessels to branch off from the aorta are the right and left coronary arteries [4] (Figure 2.8). These relatively narrow vessels provide the only supply of oxygen to the myocardium, and therefore any blockage of these vessels is critical. The left coronary artery is usually larger than the right coronary artery as it supplies the major part of the heart [5]. The arteries divide to form arterioles and capillaries similar to those found elsewhere in the body.
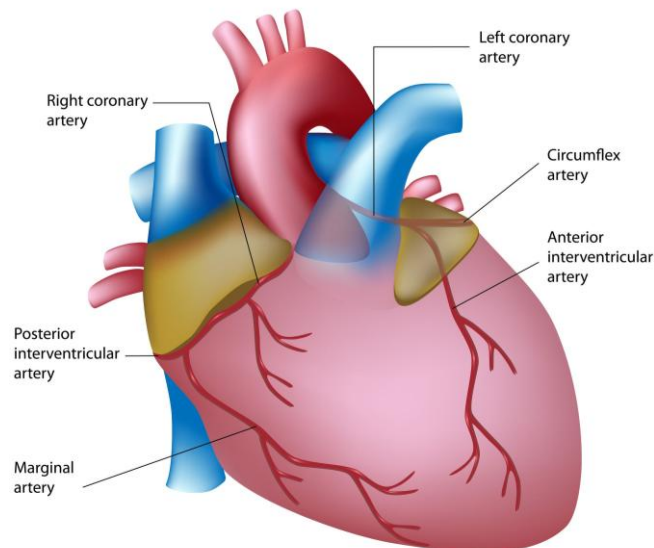
Figure 2.8 The coronary arteries provide essential blood and nutrients to the myocardium.

2.7 Blood Pressure

Blood flows through the chambers of a healthy heart at different pressures. Blood entering the right ventricle develops low pressures of ~25mmHg, whilst the blood returning from the pulmonary veins into the left atrium would typically have a pressure of ~80mmHg. However, blood leaving the left

ventricle needs to successfully travel around the whole of the circulatory system and therefore, typically reaches pressures of ~120mmHg. The values quoted for left atria and ventricle would correspond to a normal blood pressure reading of 120/80mmHg.

2.8 The Cardiac Cycle

The heart expands and contracts in a synchronised fashion that maximises its pumping efficiency, and constitutes the cardiac cycle. During each heart-beat, the right and left atria contract simultaneously, whilst the ventricles elongate and fill (ventricular diastole). This is followed in quick succession by the simultaneous contraction of the ventricles (ventricular systole) [6] before the heart returns to its resting state.

2.9 The Electrocardiogram

An electrocardiogram (ECG) is a recording of the electrical changes in the myocardial muscle during the cardiac cycle and has significant diagnostic benefits in a clinical context. The normal heart produces a typical waveform (normal sinus rhythm) that consists of five deflection waves, universally known as the PQRST complex [7] (Figure 2.9). The P wave is detected as a result of the contraction of the atrial myocardium, whilst the QRS complex results from the contraction of the larger ventricular myocardium. Finally, as the heart returns to an electrically resting state, the T wave is detected.
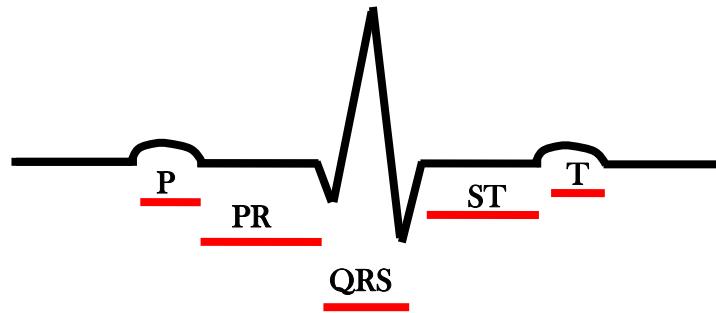
Figure 2.9 The normal heart produces a typical waveform consisting of five deflecting waves.

2.10 Diseases of the Heart

Heart diseases can present in a number of ways, depending on the nature of the underlying disease process and whether the disease process results in impaired cardiac function, coronary insufficiency or rhythm disturbances [8]. Not all cardiac diseases are relevant to the research carried out for the purpose of this, but the cause and effect of those that are have been listed below.

2.10.1 Coronary Artery Disease

The volume of blood flowing in a given portion of myocardium per unit of time is formally known as myocardial perfusion [9]. A myocardial perfusion deficit is a reduction in the blood flow to the myocardium (ischemia) and is indicative of coronary artery disease (CAD) [10]. Coronary artery disease is a chronic progressive disorder of the coronary arteries. It begins with the build-up of fatty material and cholesterol in the blood vessels. This attracts fibrous tissue and calcium, which harden into plaques, resulting in thickening of the artery walls (Figure 2.10). Plaques can break off, altering the endothelial layer and causing a thrombus (or blood clot) to form within the cardiovascular system

[11]. This can partially or totally block (occlude) the coronary arteries, a process known as atherosclerosis. The section of myocardium fed by the affected vessel may be rendered virtually bloodless (infarcted) and thus the supply of oxygen and nutrients to the body may be greatly restricted.

Time
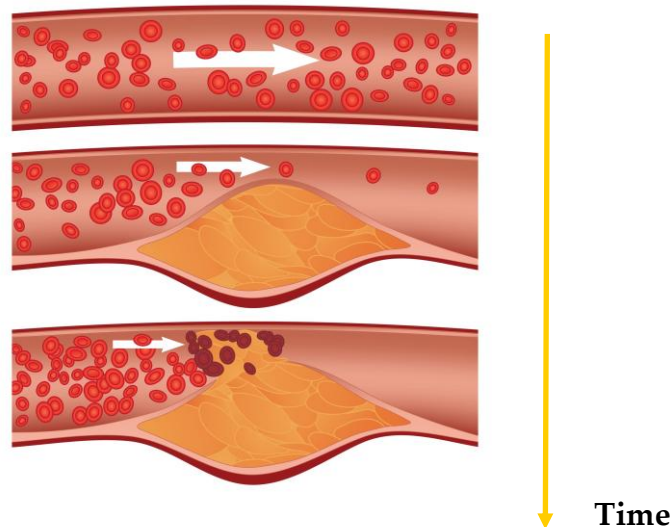
Figure 2.10 Fatty materials and cholesterol can build up in the blood vessels

Under normal resting conditions, the myocardium can recover almost completely from 10–15 minutes of ischemia as the myocytes remain viable [12]. However, certain changes do take place in the myocardium, such as post-ischemic contractile dysfunction, which refers to abnormal mechanical properties of the ventricle wall.

Severe and prolonged ischemia can lead to the destruction of cell membranes and consequently, cell death [13]. Non-viable myocytes cause tissue scarring (myocardial infarction, MI) and irreversible contractile dysfunction. Myocardial

infarction progresses through the myocardium in a wave-like fashion. It starts at the sub-endocardium and progressing through the mid-myocardium, before finally reaching the sub-epicardium. Timely clinical intervention has the potential to prevent the progress of the infarction through the myocardium and thus preserve some contractile function in the myocardial wall segment fed by the occluded vessel or vessels.

2.10.2 Valve Disease

Disease, congenital defects and age-related changes can all affect the ability of the heart valves to open and close correctly. The mitral and aortic valves are more prone to these changes than the tricuspid and pulmonary valves due to the increased pressure (and hence, greater workload) on the left side of the heart [14].

Cusps can become rigid, thickened, or fused together; resulting in a narrowing or stenosis of the valve and subsequent backing-up of blood in the preceding chamber. Where a valve fails to close properly, blood is forced in a backwards direction through the heart by the contracting atrium or ventricle. Both of these scenarios significantly increase the size and the workload of the heart, which has to pump out an extra volume of blood with each beat.

2.10.3 Left Ventricular Hypertrophy

Left ventricular hypertrophy is an enlargement of the left ventricle of the heart and is a result of any chronic disease process that increases the pressure that the left ventricle has to generate in order to pump blood out of the heart (afterload) [8]. The mass of the myocardium increases as myocardial muscle fibres thicken (Figure 2.11). This increases the distance by which oxygen has to diffuse from the capillaries, eventually leading to impaired oxygenation of the centre of the fibre. This hypoxia is believed to be an important factor in the fibrosis that frequently develops in hypertrophied muscle [8]. Left ventricular hypertrophy is most commonly the result of uncontrolled hypertension. Previous studies have found a strong linear and independent link between increased LV mass and cardiovascular risk in patients [15, 16].

Left ventricular hypertrophy

Normal heart

Right ventricle

Left ventricle

Thickening of the myocardium of the left ventricle
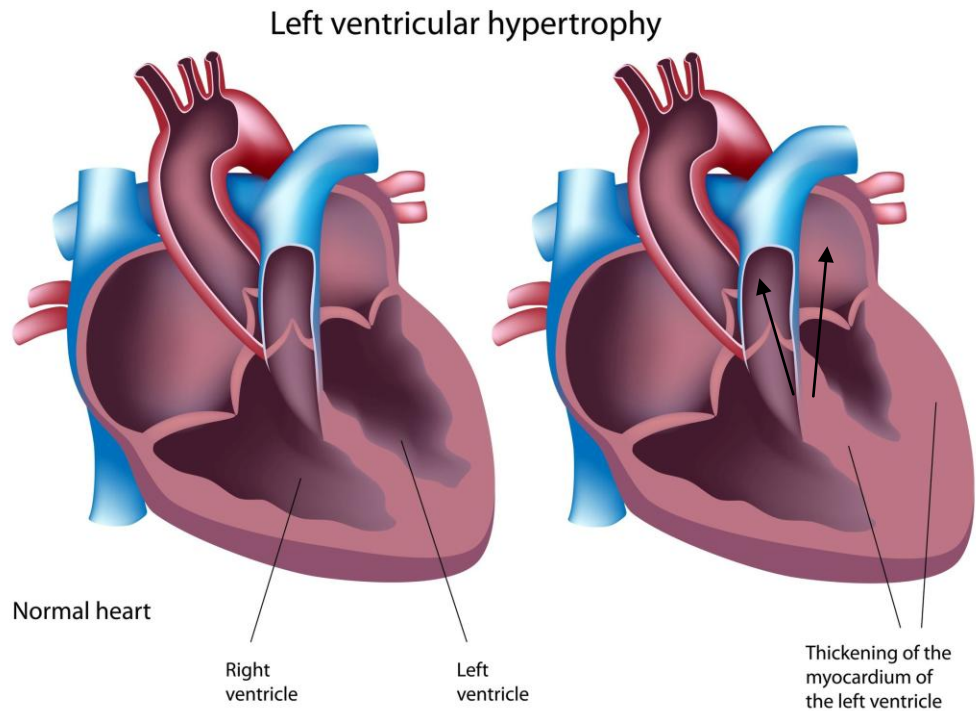
Figure 2.11 Left ventricular hypertrophy is an enlargement of the left ventricle of the heart.

2.10.4 Cardiac Arrhythmias

Cardiac arrhythmia is a term used to describe an abnormal heart rhythm. The heart rate may be too slow, too fast, or too irregular. The main cause of arrhythmias is injured myocytes, which interfere with the electrical activity of the heart. This electrical disequilibrium impairs the synchrony of the heart and impacts on the efficiency of the cardiac cycle. Consequently, the supply of oxygen and nutrients to the body is reduced.

2.10.5 Heart Failure

Heart failure is a major complication of many heart diseases. It is a syndrome defined by the symptoms resulting from diminished contractility and/or the loss of contractile tissue. The volume of blood leaving the right ventricle does

not equal that leaving the left ventricle. Hence, blood backs up, engorging the veins in the lungs and other parts of the body. The supply of blood and nutrients to the body is significantly reduced. Heart failure is a deadly disease that has reached epidemic proportions in industrialised countries [17].

2.11 Acknowledgments

Figures 2.1–2.4, 2.6, 2.7, 2.10 and 2.11 were purchased for this thesis under the terms of a standard licence (123rf.com).

References

1. *Heart Anatomy*. Houston: Texas Heart Institute; 2011 (updated September 2011; cited 23 April 2011). Available from http://www.texasheartinstitute.org/hic/anatomy/anatomy2.cfm.

2. Myocytes. *Encyclopaedia Britannica Online*; 2011(cited 23 April 2011). Available from http://www.britannica.com/EBchecked/topic/400459/myocyte.

3. Katz AM. Ernest Henry Starling, His Predecessors, and the "Law of the Heart". *Circulation* 2002; 106: 2986–92.

4. Cohen BJ, Taylor JJ. *Memmler's Structure and Function of the Human Body* (8th Edition). Philadelphia: Lippincott Williams and Wilkins, 2005.

5. Snell R. *Clinical Anatomy by Regions* (8th Edition). Baltimore: Lippincott, Williams and Wilkins, 2008.

6. Moore K, Dalley A, Agur A. *Clinically Oriented Anatomy* (6th Edition). Baltimore: Lippincott Williams and Wilkins, 2010.

7. Brooker C. *The Royal Society of Medicine Pocket Medical Dictionary* (15th Edition). London: Churchill Livingstone, 2003.

8. McLenachan J, Cowan JD. *Cardiology* (8th Edition). Edinburgh: Elsevier Saunders, 2005.

9. Elliot MD, Kim R.J. Late gadolinium cardiovascular magnetic resonance in the assessment of myocardial viability. *Coronary Artery Disease* 2005; 16: 365–72.

10. Nagel E. Magnetic resonance perfusion imaging for detection of ischemic heart disease. *Heart and Metabolism* 2008; 38: 19–21.

11. Hubbard J, Mechan D. *The Physiology of Health and Illness with Related Anatomy*. Cheltenham: Stanley Thornes (Publishers) Ltd, 1997.

12. Kloner RA, Jennings RB. Consequences of brief ischemia: Stunning, preconditioning, and their clinical implications: Part 1. *Circulation* 2001; 104: 2981–89.

13. Julian DG, Camm AJ, Fox KM, Hall RJC, Poole-Wilson A. *Diseases of the Heart* (2nd Edition). London: W.B. Saunders Company Ltd, 1996.

14. Bender J. Heart valve disease. *Yale University School of Medicine Heart Book*. New York: Hearst Books, 1992.

15. Schillaci G, Verdecchia P, Porcellati C, Cuccurullo O, Cosco C, Pertticone F. Continuous relation between left ventricular mass and cardiovascular risk in essential hypertension. *Hypertension* 2000; 35: 580–6.

16. Fuster V, Kim RJ. Frontiers of cardiovascular magnetic resonance imaging. *Circulation* 2005; 112: 135–144.

17. Khan M.G. *Heart Disease Diagnosis and Therapy: A Practical Approach* (2nd Edition). New Jersey: Humana Press Inc. 2005.

3. The Development of Cardiac Magnetic Resonance Imaging

Current cardiac magnetic resonance imaging (CMRI) is virtually unrecognisable from the primitive scans of the 1980s. Significant advancements have transformed CMRI from a lengthy, complicated, artefact-prone technique that was largely avoided by clinicians, into an essential clinical tool that has recently emerged as the accepted gold standard imaging modality for cardiac mass, function and myocardial viability [1, 2].

Figure 3.1 A 3.0T MRI scanner and a volunteer encased in a combination of surface coils.

3.1 Hardware Developments

Speed and efficiency are a fundamental requirement of successful CMRI because of the associated physiological motion and flow constraints. These requirements were the motivating force for many developments involving advanced CMRI hardware and software. We begin this chapter with a discussion on the main hardware developments before moving on to the software developments and cardiac application that have contributed to the transformation of CMRI.

3.1.1 Higher Fields

Progression in CMRI has been intimately related to the rapid historical increments in the magnitude of the external magnetic field. The first clinical whole-body scanner, constructed in Aberdeen in 1980, had a static magnetic field strength of 0.04 Tesla (T). By 1998, researchers at The Ohio State University, USA, had designed and assembled the world's first 8T whole-body scanner [3] although the primary components were manufactured by different well established instrumentation companies. More recently, the University of Illinois, USA, developed a whole-body scanner with a main magnetic field strength of 9.4T.

Presently, MRI scanners with field strengths in excess of 4T can only be used for research purposes due to strict international regulations that were introduced to protect the patient [4]. When this limit was introduced in 2002 there was an

immediately shift in 3.0T systems from the research to the clinical setting [5] after approximately 15 years of optimisation.

Field strengths in the Tesla range would not have been possible without the introduction of niobium-titanium alloy superconducting magnets in the early 1980s. These magnets have greatly improved magnetic field stability and homogeneity compared to those of the air or iron core electromagnets that preceded them [6].

The cardiac images obtained for the purpose of this research were acquired using a 1.5T Siemens Avanto and a 3.0T Siemens Trio (Figure 3.1). Fields of these magnitudes are considered crucial for CMRI as they provide the essential combination of spatial and temporal resolution. In addition to this, both systems are equipped with top-of-the- range gradient systems.

3.1.2 Gradient Capabilities

Cardiac imaging requires high performance gradients in order to take advantage of the potential for faster imaging and to provide images of a beating heart that have sufficient spatial resolution for diagnostic purposes. Thus, gradient performance has been another focus of intense research and development over the past three decades.

Gradient strengths have increased from 10mT/m in the 1980s to 50mT/m today, whilst current slew rate limits are in the order of $200 Tm^{-1}s^{-1}$.

However, gradient systems are now considered to be at human physiological limits because of peripheral nerve stimulation [7], which occurs when rapidly switching gradients induce electric fields in the tissue of the patient. This shifts the charge in the nerve fibres and stimulates peripheral nerves. Peripheral nerve stimulation can be avoided by restricting the exposure of the patient or volunteer to pulsed magnetic fields below a magnitude of 20 Ts^{-1}. This corresponds to a current density of $400mAm^{-1}$.

3.1.3 Phased Array Coils

Due to the restrictions on gradient performance, other techniques were explored and developed in a continuing bid to improve temporal resolution. One such development was the design and implementation of phased array coil technology in the late 1980s (Figure *3.2)*. The first multi-element coil was a simple two-element array. Since then, phased array coil technology has developed at an efficient pace and now state-of-the-art coil systems with up to 32 elements are available in the clinical setting.
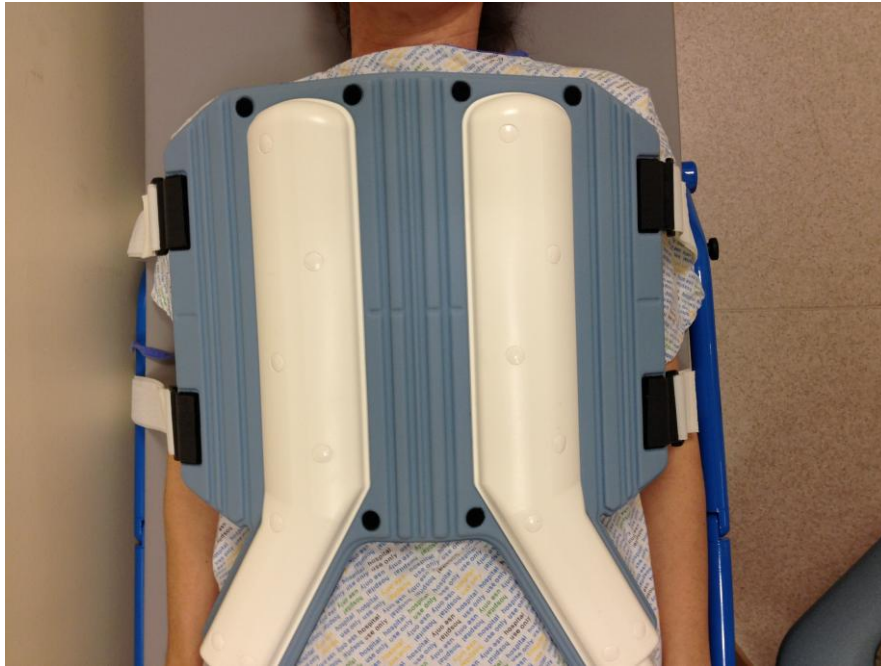
Figure 3.2 Phased array coil technology helps to improve spatial and temporal resolution.

Phased array coil technology has not yet reached its full potential. Scientists are continuing to design, develop and perfect systems with an ever increasing numbers of array coil elements [8]. As each element of an array coil must be attached to a separate independent receiver channel (to minimise coupling between the elements), magnet manufacturers have had to quickly respond to this technology by increasing the number of available channels in their MRI receivers [9, 10].

Phased array technology has successfully improved the spatial and temporal resolution of cardiac imaging, but just as importantly, it has also provided the necessary hardware for parallel imaging techniques.

3.1.4 Parallel Imaging

The concept of parallel imaging (PI) was introduced between the years of 1987 and 1993 [11–13] as a means of compensating for the severe limitations resulting from gradient capabilities. The initial idea of parallel imaging was to achieve ultra-fast imaging by eliminating the time-consuming phase encoding steps required to build an MR image. This was thought to be achievable by exploiting the differences in sensitivities between the multiple individual coil elements in a receive array. However, it soon became apparent that there was a fundamental and practical limit to the number of phase encodes possible using this technique [14]. Hence, a new strategy for parallel imaging was successfully developed, which uses the spatial information inherent in an array coil to allow a reduction in phase encoding steps. [15]. Although this technique is formally known as partially parallel imaging (PPI) in a bid to differentiate it from the earlier technique, it is commonly referred to as parallel imaging.

3.1.5 Nyquist Criteria

Loosely sampling the MRI data by reducing the number of phase encoding steps violates the Nyquist criteria if the sampling rate is less than twice that of the highest frequency expected. This would result in a reduction in the field of view if spatial resolution is not to be compromised [16]. For this reason, parallel imaging applies various reconstruction techniques to reconstruct full images from the sub sampled data. These techniques recover the sampling to the Nyquist rate by exploiting spatial or temporal correlations [17].

Practical implementation of PI techniques began in 1997 with the introduction of simultaneous acquisition of spatial harmonics (SMASH) [18]. SMASH performs image reconstruction in the k-space domain by using coil sensitivity maps from the image domain to determine the reconstruction parameters. The introduction of this technique attracted enthusiastic interest from the MRI community due to the fact that it was proposed and implemented in cardiac imaging, which is considered one of the most challenging MRI disciplines [19].

The introduction of other novel PI techniques quickly followed. These techniques included two of the most popular and successful PI techniques to date: sensitivity encoding for fast MRI (SENSE) was introduced in 1999 [20] and generalised autocalibrating partially parallel acquisitions (GRAPPA) in 2002 [21]. With SENSE the coil reference data and the sub-sampled MRI data are operated on in the image domain to produce the final image whilst with GRAPPA, all data are operated on in the k-space domain. GRAPPA and SENSE both provide good results [22] and are now widely available on commercial scanners.

Parallel imaging in combination with phased array coil technology considerably enhances the performance of CMRI by reducing acquisition times, speeding up fast imaging techniques and reducing flow and motion artefacts. PI is

particularly beneficial at high fields as the reduced scanning times make it easier for the operator to remain within specific absorption rate (SAR) thresholds [23].

3.2 Software Developments

Over the past three decades there has been a rapid growth in the number and type of pulse sequences available in a bid to meet the growing demand for new applications. The class of sequences that have now become standard in a cardiac imaging protocol will be discussed in Chapter 5 of this thesis. However, special mention must be given at this point to a one of these rapid imaging sequences that is based on a fast gradient echo acquisitions known as balanced steady-state free precession (SSFP). SSFP sequences provide excellent SNR and T2/T1 contrast allowing the generation of exceptional contrast between blood and muscle, regardless of flow.

3.2.1 K-Space

As previously mentioned, the conventional way to fill k-space was in a linear or sequential fashion, one horizontal line at a time. Each line of the k-space matrix required a new echo and hence, a new excitation pulse. K-space could be filled from the bottom (linear) or from the top (reverse linear) with the centre line of k-space always being acquired in the middle. This was a lengthy process with spin echo techniques as a sufficient 'wait time' is necessary between excitation

pulses to allow the net magnetisation vector to recover enough to produce a detectable signal with the next RF pulse.

The introduction of gradient echo techniques in 1991 helped address this problem as their reduced flip angles improved temporal resolution by reducing the required wait time (as partial flips need less time to relax back into equilibrium than 90° or 180° pulses) [24].

3.2.2 K-Space Segmentation

Similar developments since then have looked at filling k-space in a more time efficient manner [25]. Multi-echo imaging uses a single excitation pulse to create a train of echoes, each of which is used to simultaneously fill a line of k-space. For example, a train containing four echoes would fill k-space four times faster than conventional k-space filling. An added advantage of this technique is that it can also be used to determine the contrast of an image as each of the echoes in the train will have a different TE. Hence, placing the first echo in the centre of K-space will provide a proton density weighted image, whilst placing the last echo in the centre of k-space provides a heavily T2-weighted image.

Another novel technique exploited the conjugate symmetry of k-space in a bid to improve temporal resolution. Simply by collecting slightly more than the second half of the echo only (fractional echo), just over one half of k-space could be filled and the fractional data flipped to fill the whole of k-space. In the same

way, the whole echo could be used to fill just slightly more than the top or bottom of k-space, before the data is flipped to fill the whole of k-space.

Although these techniques provide full resolution data, they do impact on the SNR. However, SNR could be increased by increasing the number of times the signal was sampled (averages). These k-space techniques had a major impact on CMRI as they significantly reduced acquisition times from 3–5 minutes for four to five slices, to just a few seconds [26].

3.2.3 Echo Planar Imaging

Echo planar imaging (EPI) [27] is the fastest imaging method available at present. EPI acquires multiple lines of imaging data after a single RF pulse. There are a number of different EPI methods available that differ in the way that they efficiently fill k-space. For example, single shot EPI can fill k-space in a blipped (blipped phase encoding) or constant (constant phase encoding) way. Single shot techniques fill the whole of k-space in a single TR, effectively eliminating any degree of T1 weighting in the image. Hence image contrast depends on proton density and T2.

Echo planar imaging is a technologically challenging technique that requires high performance gradient systems and special RF coils to minimise gradient induced Eddy currents. However, the introduction of these techniques allowed

images to be acquired in milliseconds rather than minutes, in some cases reflecting nearly a 10,000-fold gain in speed [28].

3.3 Cardiac Applications

It is not just hardware and software developments that have transformed CMRI. Certain applications have also contributed as they have had a major impact on the reduction of cardiac and respiratory motion artefacts.

3.3.1 Breath-Holding Techniques

Efficient k-space segmentation brought cine cardiac imaging into the realms of a single breath-hold, permitting the introduction of breath-holding techniques for most cardiac acquisitions. By instructing the patient to hold their breath at end-expiration, for the duration of an acquisition (typically around 15 seconds), respiratory motion-induced artefacts could be dramatically reduced.

3.3.2 Gating and Triggering Techniques

Cardiac gating and triggering techniques were first employed in CMRI in 1981 [29] and introduced as a standard application 1984 [30]. Gating and triggering techniques significantly reduced motion artefact by correlating the acquisition of cardiac images at a specific phase of the cardiac cycle with a physiological signal from the patient; generally, an electrocardiogram (ECG) (Figure 3.3).
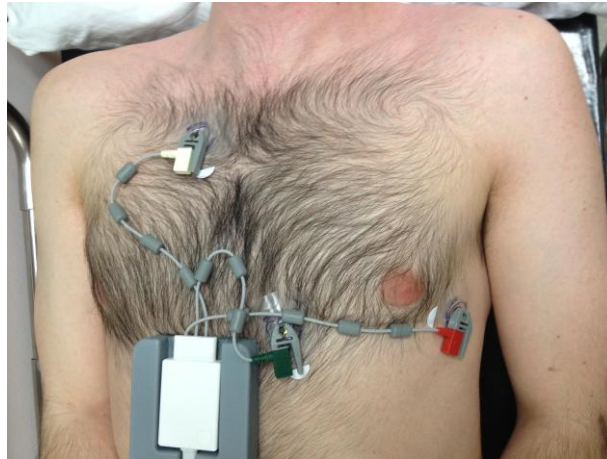
Figure 3.3 Cardiac gating significantly reduces motion artefact

3.3.2.1 Prospective Triggering

Prospective triggering utilises the preceding R wave of the QRS complex to trigger image acquisition during the subsequent R–R interval. This technique requires the image acquisition length to be shorter than the R–R interval, otherwise the next R wave will be ignored, prolonging acquisition times and potentially creating image artefacts. This technique is particularly useful whenever data acquisition is too slow to occur during a short fraction of the cardiac cycle.

An unfortunate limitation of this technique is that it is not possible to capture the whole cardiac cycle. Hence, end of diastole and early atrial contraction are not acquired [31].

3.3.2.2 Retrospective Gating

Retrospective gating is particularly useful when acquiring images of the beating heart, as data is acquired continuously throughout the R–R interval

and then retrospectively matched to the patient's ECG tracing. Retrospective gating does not require a trigger window, allowing irregular heartbeats to be rejected. Hence, this technique is valuable for alleviating the problems associated with arrhythmias where irregular heartbeats can fail to trigger image acquisition, potentially resulting in an inaccurate assessment of cardiac function.

3.4 Contrast Agents

The introduction of gadolinium-based contrast agents to CMRI [32] played a significant role in the overall success of the technique. Gadolinium (Gd) is a rare Earth element that has seven electrons in its outer shell, making it one of the most effective paramagnetic agents. Due to the extreme toxicity of free gadolinium, it is always chelated to diethylene triamine pentaacetic acid (Gd-DTPA) for imaging purposes. This makes it non-toxic and easily cleared via the kidneys.

Figure 3.4 Dotarem is a gadolinium-based contrast agent used frequently in MRI.

Gd-DTPA is administered intravenously and rapidly diffuses from the vascular space to the extracellular space due to its small molecular size of 550 Da. It enhances imaging by shortening the T1 and T2 of tissues (although the decrease in T2 is very slight) through the interaction of its unpaired electrons with the Hydrogen nuclei in water. The effect on T1 is linearly proportional to the concentration of the agent.

$$\frac{1}{T1_c} = \frac{1}{T1_i} + R_1 * C \qquad (1)$$

Where $T1_c$ is the T1 of the tissue after the administration of Gd-DTPA, $T1_i$ is the inherent T1 of the tissue, R is the relaxivity of Gd-DTPA (~4.5L/mmol/s) and C is the concentration of Gd-DTPA.

3.5 Conclusion

The hardware, software and cardiac applications discussed in this chapter have all made a significant contribution to the successful development of CMRI as a powerful imaging tool. Many of the techniques mentioned continue to develop at an efficient pace with the ultimate goal of providing real-time cardiac imaging.

References

1. Bogaert J, Dymarkowski S, Taylor A. Comparison of left ventricular ejection fraction and volumes in heart failure by echocardiography, radionuclide ventriculography and cardiovascular magnetic resonance; are they interchangeable? *European Heart Journal* 2000; **21**: 1387–96.

2. Clay S, Alfakih K, Radjenovic A, Jones T, Ridgway JP, Sinvananthan MU. Normal range of human left ventricular volumes and mass using steady state free precession MRI in the radial long axis orientation 200. *MAGMA* 2006; **19**: 41–5.

3. Burgess RE (2004) Magnetic Resonance Imaging at Ultra High Field: Implications for Human Neuroimaging. Dissertation, The Ohio State University, USA.

4. U.S. Department of Health and Human Services, Food and Drug Administration, Centre for Devices and Radiological Health, Radiological Devices Branch, Guidance for Industry: www.fda.gov.

5. Kuhl C, Träber F, Schild HH. Whole-body high-field-strength (3.0-T) MR imaging in clinical practice. Part 1. Technical considerations and clinical applications. *Radiology* 2008; **246**: 675–96.

6. Hu X, Norris DG. Advances in high-field magnetic resonance imaging. *Annual Review of Biomedical Engineering* 2004; **6**: 157–84.

7. Blaimer M, Breuer F, Mueller M, Heidemann RM, Griswold MA, Jakob PM. SMASH, SENSE, PILS, GRAPPA. How to choose the optimal method. *Topics in Magnetic Resonance Imaging* 2004; **15**: 223–35.

8. Wiggins GC, Polimeni JR, Potthast A, Schmitt M, Alagappan V, Wald LL 96-channel receive-only head coil for 3 Tesla: Design optimisation and evaluation. Magn Reson Med 2009; 62(3): 754-762.

9. Hyde J.S. Froncisz W., Jesmanowicz A., Kneeland J.B. Simultaneous image acquisition from the head (or body) coil and a surface coil. *Magnetic Resonance in Medicine* 1998; **6**: 235–9.

10. Wright SM, McDougall MP, Kurpad K. Coil Arrays for parallel MRI: Introduction and Overview. Magnetic Resonance Systems Laboratory, Department of Electrical Engineering Texas A&M University, College Station, TX, USA. http://www.mr.ethz.ch/parallelmri04/abstracts/pub/Wright.pdf

11. Carlson J.W. An algorithm for NMR imaging reconstruction based on multiple RF receiver coils. *Journal of Magnetic Resonance* 1987; **74**: 376–380

12. Hutchison M., Raff U. Fast MRI data acquisition using multiple detectors. *Magnetic Resonance in Medicine* 1998; **6**: 87–91.

13. Kwait D, Einav S, Navon G. A decoupled coil detector array for fast image acquisition in magnetic resonance imaging. *Medical Physics* 1991; **18**: 251–65.

14. Kellman P. Parallel imaging: The basics. ISMRM 2004. http://dir.nhlbi.nih.gov/staffpages/kellmanp/flash/ISMRM%202004%20-%20Parallel%20Imaging%20-%20The%20Basics.swf

15. Attili A, Schuster A, Nagel E, Reiber JHC, van der Geest RJ. Quantification in cardiac MRI: advances in image acquisition and processing. *International Journal of Cardiovascular Imaging* 2010; **26**: 27–40.

16. Kozerke S, Plein SJ. Accelerated CMR using zonal, parallel and prior knowledge driven imaging methods. *Journal of Cardiovascular Magnetic Resonance* 2008; **10**: 29.

17. Lai P, Huang F, Larson AC, Li D J. Fast four-dimensional coronary MR angiography with k-t GRAPPA. *Journal of Magnetic Resonance Imaging* 2008; **27**: 659–65.

18. Sodickson DK, Manning WJ. Simultaneous acquisition of spatial harmonics (SMASH): fast imaging with radiofrequency coil arrays. *Magnetic Resonance in Medicine* 1997; **38**: 591–603.

19. Larkman DJ, Nunes RG. Parallel magnetic resonance imaging. Physics in Medicine and Biology 2007; **52**: R15–R55.

20. Pruessmann KP, Weiger M, Scheidegger MB, Boesiqer P. SENSE: sensitivity encoding for fast MRI. *Magnetic Resonance in Medicine* 1999; **42**: 952–62.

21. Griswold MA, Jakob PM, Heidemann RM, Nittka M, Jellus V, Wang J, Kiefer B, Haase A. Generalised autocalibrating partially parallel acquisitions (GRAPPA). *Magnetic Resonance in Medicine* 2002; **47**: 1202–10.

22. Griswold MA. Advanced K-Space Based Parallel Imaging Methods. University of Wurzburg, Wurzburg, Germany.

23. Evidence review. Multi-channel RF and parallel imaging technologies for MRI scanners. NHS Purchasing and supply agency 2008. CEP 08016

24. Atkinson DJ, Edelman RR. Cineangiography of the heart in a single breath hold with a segmented turbo-FLASH sequence. *Radiology* 1991; **178**: 357–360.

25. Chien D, Atkinson DJ and Edelman RR. Strategies to improve contrast in turboFLASH imaging: Reordered phase encoding and K-space segmentation. *Journal of Magnetic Resonance Imaging* 1991; **1**: 63–70.

26. Didier D, Ratib O, Friedli B, Oberhaensli I, Chatelain P et al. Cine gradient-echo MR imaging in the evaluation of cardiovascular diseases. *Radiographics* 1993; **13**: 561–73.

27. Mansfield P. Multi-planar image formation using NMR spin echoes. *Journal of Physics C* 1977; 10:L55:349-352].

28. Moonen CTW, Bandettini PA, Baert AL. Echo-planar imaging (EPI) and functional MRI. Springer-Verlag Berlin Heidelberg 1999

29. Nuclear magnetic resonance (NMR) tomography of the normal heart. Hawkes RC, Holland GN, Moore WS, Roebuck EJ, Worthington BS. *Journal of Computer Assisted Tomography* 1981; **5**: 605–12.

30. Lanzer P, Barta C, Botvinick EH, Wiesendanger HUD, Modin G, Higgins CB. ECG synchronised cardiac MR imaging: method and evaluation. *Radiology* 1985; **155**: 681–6.

31. Bogaert J, Dymarkowski S, Taylor A. Comparison of left ventricular ejection fraction and volumes in heart failure by echocardiography, radionuclide ventriculography and cardiovascular magnetic resonance; are they interchangeable? *European Heart Journal* 2000; **21**: 1387–96.

32. Lombardi M, Jones RA, Westby J, Torheim G, Southon TE, Haraldseth O, Michelassi C, Kvaerness J, Rinck PA, L'Abbate A. Use of the Mean Transit Time of an Intravascular Contrast Agent as an Exchange-Intensive Index of Myocardial Perfusion, *Journal of Magnetic Resonance Imaging* 1999; **9**: 402–8.

33. Brown M, Semelka RC, *MRI: Basic Principles and Applications*. Wiley-Liss, New York, 1999.

34. Ferrari M. Cancer nanotechnology: Opportunities and challenges. *Nature Reviews Cancer* 2005; 5: 162–71.

35. Nagahara LA, Lee JSH, Molnar LK, Panaro NJ, Farrell D et al. Strategic workshop on cancer nanotechnology. *Cancer Research* 2010; **60**: 4265–8.

36. Sanvicens N, Marco MP. Multifunctional nanoparticles – properties and prospects for their use in human medicine. *Trends in Biotechnology* 2008; **26**: 425–33

4. The Advantages, Challenges and Limitations of Imaging at 3.0T in Comparison to 1.5T

4.1 Introduction

Two MRI scanners with similar high-end gradient systems were used for the purpose of this research; a 1.5T Avanto that had been installed 6 years prior to the start of this work, and a 3.0T Trio that was installed 1 year after it commenced. Both systems were manufactured and installed by Siemens Medical Solutions (Erlangen, Germany).

Cardiac imaging at 1.5T has been established for many years. This allowed us to use the Avanto to look at disease related changes in the right ventricle of the human heart using a previously optimised CMRI protocol (chapter 6). However, when the Trio was installed a year into the start of this research, CMRI at 3.0T was still relatively new. For this reason, the studies carried out in Chapters 7 and 8 of this thesis had to initially focus on image optimisation at this field strength.

Cardiac imaging at 3.0T is immediately advantageous for the gain in SNR but it also presents many limitations and challenges. This chapter discusses the pros and explains the cons of imaging at 3.0T in comparison to 1.5T.

4.2 Technical Details of the Magnetic Fields

The technical details of the main, RF and gradient magnetic fields of each system are listed in tables 4.1–4.3.

Table 4.1 External Magnetic Field.

Scanner	Avanto	Trio
Operating Strength (Tesla)	1.5	3.0
Superconductor	Niobium-Titanium	Niobium-Titanium
Stability Over Time (ppm/h)	< 0.1	< 0.1

Table 4.2 Gradient Magnetic Field Performance per Axis.

Scanner	Avanto	Trio
Engine	(76 x 32)SQ	(102 x 32)TQ
Max. Amplitude (mT/m)	45* or 40	45* or 40
Min. Rise Time in μsec (mT/m)	200 (0–40)	200 (0–40)
Max, Slew Rate (T/m/s)	200	200

*DSV, diameter spherical volume (x,y,z) direction.

Table 4.3 Radiofrequency (RF) System.

Scannner	Avanto	Trio
Peak Power of Transmit Amplifier (kW)	15	35
Transmitter Bandwidth (kHz)	500	800
Receiver Bandwidth per channel (Hz)	500-1x106	500-1x106
Maximum Applied RF Field (μT)	30.0	24.7

4.3 The Images

Magnetic resonance images are composed of a distribution of voxels, each of which is comprised of a mixture of signal power and random or systematic

noise. The ratio between this signal and noise [signal-to-noise ratio (SNR)] is of paramount importance for determining the image quality.

4.4 The Signal

As discussed briefly in chapter 1 of this thesis, the signal in MRI comes from the precession of the net magnetisation vector $\mathbf{M_{xy}}$. The precessing vector produces a time-varying magnetic flux that induces a voltage or electromotive force (*emf*) in an appropriately positioned receiver coil [1], According to the principle of reciprocity this can be considered as equivalent to a constant flux, produced by a unit current that is flowing around a receive coil and that penetrates the precessing magnetisation of the sample. Thus, the *emf* induced in the coil is given by [2]:

$$ emf = -\oint \frac{d}{dt}(\underline{M} \cdot \underline{B_1}) d^3r \qquad (4.1) $$

Where B_1 is the time varying magnetic flux produced by the receiver coil per unit current. The vectors M and B_1 form the dot product.

In an ideal system, (ignoring any spin–spin interactions and field inhomogeneities) the signal in each voxel of an MR image can be quantified as a function of the transverse magnetisation in equilibrium ($\mathbf{M_0}$), the centre frequency (ω_0), the B_1 magnetic field and the voxel size ($V_s = \Delta x, \Delta y, \Delta z$) [2].

$$Signal \propto \omega_0 M_0 B_1 V_s \qquad (4.2)$$

By substituting for M_0 (Eq. 1.5) and the Larmor relationship (Eq. 1.6), the signal gain can be shown to be proportional to the square of **B_0.** Thus, by imaging at 3.0T rather than 1.5T we should anticipate a theoretical four-fold increase in signal.

$$Signal \propto \frac{\gamma^3 B_0^2 \rho_0 V_s}{T} B_1 \qquad (4.3)$$

4.5 The Noise

This noise *emf* in an MR image is uniformly distributed over all frequencies and increases as the square of the Larmor frequency at high fields [3]. It is dominated by Johnson or 'white' noise [4], which is a consequence of the thermally driven Brownian motion of electrons within the patient's tissue and within the receiver coil. Human tissue contains many electrolytes that are essential for normal cell function and movement of these ions generates weak electric currents within the body.

The noise *emf* in MRI is proportional to the square root of the receiver bandwidth (BW_r) [5] and is influenced by averaging parameters, such as the number of signal averages (NSA), the number of phase encoding (N_{PE}) steps and the number of frequency encoding (N_{FE}) steps used to create the image.

$$noise \propto \frac{\sqrt{BW_r}}{\sqrt{NSA \cdot N_{PE} \cdot N_{FE}}} \qquad (4.4)$$

Noise from the coils in MRI comes in the form of electrical noise (from the receiving circuit and other external noise contributions). Electrical noise is present in all electrical conductors and is a result of random fluctuations in electrical currents [6]. However, the coils used today in MRI are highly optimised and as a result of this, electrical noise contributions are now considered trivial.

The variance, or random fluctuations, of the noise voltage gives a measure of the quality of the MR data. Noise variance is also a crucial parameter in image processing algorithms such as noise reduction [7]. The equation used to calculate noise variance in MRI is a very fundamental and widely used expression. It is presented here without proof as [8]:

$$\mathrm{var}(emf_{noise}) = \sigma^2 = 4kTR_{eff}BW_r \qquad (4.5)$$

Where R_{eff} is the effective resistance of the receiver coil loaded with the patient.

4.5.1 Signal-to-Noise Ratio

Taking the theoretical four-fold increase in signal into consideration, and offsetting it with the associated linear increase in noise, there is an expected

doubling in signal-to-noise ratio (SNR) between 1.5T and 3.0T under ideal imaging conditions and optimised acquisition techniques [9].

However, CMRI is never performed under ideal imaging conditions due to the challenges of motion and flow associated with the heart. In addition to this, there are further challenges associated with CMRI at 3.0T which include specific absorption rate limits, external field inhomogeneities, susceptibility effects and tissue relaxation times. These challenges have to be taken into consideration as they can all impact on image quality, and correcting for them is nearly always at the expense of SNR. In practice, the actual gain in SNR between 1.5T and 3.0T is usually around 40% with CMRI [10]. This is still a very desirable signal gain and it can be further enhanced by adjusting certain parameters during imaging. For example, the SNR is inversely proportional to the square root of the bandwidth (BW) and proportional to the square root of the number of phase-encoding steps (N_y) and the number of excitations (NEX):

$$SNR \propto (pixel volume)\sqrt{\frac{N_y NEX}{BW}} \quad (4.6)$$

4.6 The Advantages of CMRI at 3.0T

The gain in SNR is the driving force behind cardiac imaging at 3.0T as it can be utilised to facilitate higher spatial and/or temporal resolution than was previously possible at 1.5T. During the image optimisation at 3.0T the

preference was to utilise the increased SNR to improve temporal resolution. Thus, where possible, two to three image slices were acquired per breath-hold at 3.0T in comparison to one to two slices per breath-hold at 1.5T. Increasing temporal resolution provides obvious advantages for volumetric coverage of the heart as it reduces imaging times, and thus decreases the likelihood of motion and flow induced artefacts.

4.7 The Challenges and Limitations of CMRI at 3.0T

The challenges and limitations of CMRI at 3.0T are reflected in its relatively slow acceptance at this field strength [11]. A fundamental reason for many of these challenges and limitations is the linear increase in resonance frequencies, as determined by the Larmor equation. Frequencies increase from 63.9MHz at 1.5T to 127.8MHz at 3.0T and this increase impacts on many physical parameters, some of which are described below. These challenges and limitations had to be considered when optimising left ventricular and left atrial imaging on the 3.0T Trio.

4.7.1 Chemical Shift

The bulk of the MRI signal comes from hydrogen nuclei in the form of water molecules; however other molecules also contribute to the MR signal, including hydrogen nuclei in fatty tissues (lipids). Fat molecules differ considerably in structure and size from water molecules as each fat molecule contains 10–20 carbon atoms and each carbon atom has two hydrogen atoms attached to it.
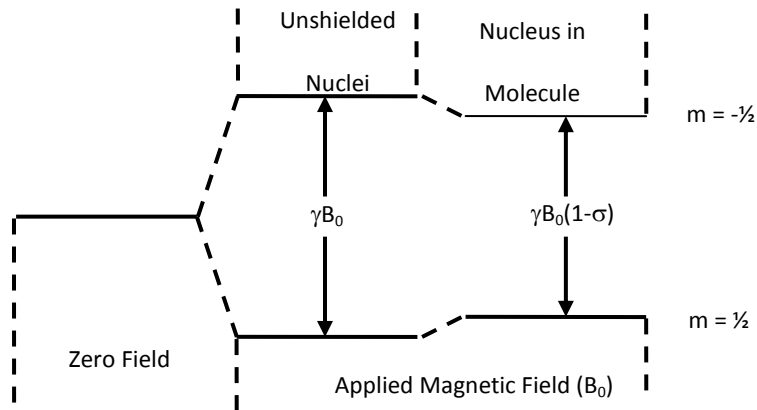
Figure 4.3 The magnetic field that molecules experience is determined by their chemical environment

When water and fat molecules are placed within a strong magnetic field, their electrons circulate within their atomic orbits, inducing a small magnetic field $\mathbf{B_i}$. Depending on the electronic structure of the molecule, this induced field will act to increase or oppose $\mathbf{B_0}$ (Figure 4.3) [12]. Thus, water and fat molecules experience a magnetic field ($\mathbf{B}$) that is determined by both their chemical environment and the magnitude of the applied field $\mathbf{B_0}$. The electron cloud around fat molecules acts to reduce the strength of B_0 and a consequence of this is that the hydrogen atoms in fat molecules have a lower Larmor frequency than the hydrogen atoms in water molecules, which have less chemical shielding.

$$B = B_0 - B_i = B_0(1-\sigma) \quad (4.8)$$

Where σ is the shielding constant of proportionality between $\mathbf{B_0}$ and $\mathbf{B_i}$.

The difference is only 3.5 parts per million (ppm) but it often results in chemical shift artefact where fat and water protons with the same spatial location in tissue emit different signals, and as a consequence of this, fat signals are shifted by a number of pixels in the frequency encoding direction of the image. This manifests on the image as a hypo-intense band of one or more pixels in width, towards the higher frequencies (due to the subtraction of the fat and water signals) and a hyper-intense band towards the lower frequencies (due to the addition of overlapping water and fat signals) (Figure 4.4b).

Chemical shift artefact of this type occurs with spin echo and gradient echo pulse sequences and scales linearly with field strength. It is usually expressed in Hertz or parts per million (ppm):

$$\frac{\omega}{2\pi} = 3.5 \times 10^{-6} \times \gamma B_0 \qquad (4.9)$$

Figure 4.4a Overhead view of a phantom containing a bag of butter (lhs), a cup of oil, and a bag of fat (rhs).
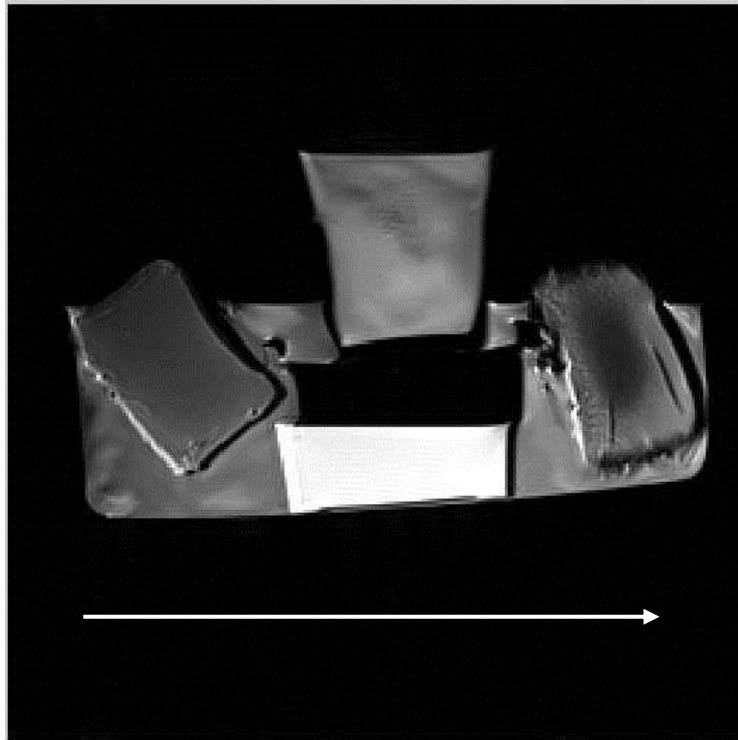
Figure 4.4b The phantom in 4.4a has been filled with water and imaged at a bandwidth of 780Hz/ pixel to show areas of hyper- and hypo-enhancement in the frequency encoding direction (arrow).

4.7.2 Chemical Shift of the Second Kind

The linear increase in resonant frequencies between 1.5T and 3T can also result in a second type of chemical shift artfact when gradient echo techniques are used. Immediately after the RF excitation pulse is applied, fat and water molecules precess in phase. However, due to the difference in their resonant frequencies, they quickly begin to precess in and out of phase with each other. At 1.5T, the hydrogen atoms in fat and water precess in-phase at an echo time (TE) = 0msec, 4.5msec etc., and out of phase at a TE = 2.25msec, 6.75msec etc (4.10).

$$T = 1/f = 1/220Hz = 4.5m\sec \quad (4.10)$$

$$T = 1/f = 1/440Hz = 2.3m\sec \quad (4.11)$$

At 3.0T, this periodicity is almost halved (4.11) making it more difficult for the operator to ensure that the echo time falls at a desired point in the cycle when the fat and water atoms are in phase.

When water and fat are in phase, the signals add together and no artefact occurs. Conversely, when they are out of phase, a signal cancellation occurs and leads to a 'boundary effect' artefact on images; so-called as the artefact manifests itself as a dark boundary along water–fat interfaces (in particular, organs that are surrounded with fat).

A number of techniques are available to eliminate or reduce chemical shift artefacts. For example, the severity of the chemical shift artefact is dependent on the receiver bandwidth used for imaging. Therefore, it is possible to avoid this artefact by increasing the receiver bandwidth, but this will be at the expense of SNR as doubling the receiver bandwidth reduces the SNR by $\sqrt{2}$ (approximately 30%). However, this may be acceptable at 3.0T due to the increased SNR available.

Other options for reducing or eliminating chemical shift artefact include increasing the strength of the frequency encoding gradient to make subtle

differences to the Larmor frequency less relevant or, in the case of the first type of chemical shift artefact, simply switching the phase and frequency encoding directions during imaging.

4.7.3 Dielectric Effect

The propagation velocity of the electromagnetic wave can be considered independent of the frequency in MRI. Hence, the wavelength of the RF excitation pulse (B_1 field) decreases with increasing field strength.

It is estimated that the RF wavelength (λ) is ~ 234cm in free space. However, the dielectric constant for biological tissue is high, ranging from between 10 and 100, and this reduces the wavelength of the RF excitation pulse as it enters the body by the inverse of the square root of the constant [13]. Hence, it is estimated that λ at 3.0T is reduced from ~234cm in free space to about 25–30cm in human tissue, making it comparable to human body dimensions. This 'dielectric effect' can lead to standing wave patterns within the body cavity as the short RF wavelength interferes with its own reflection due to the boundary between air and water. Constructive and destructive interferences of the transmitted RF field give rise to regional brightening or regional signal loss in the image.

4.7.4 B_1 Inhomogeneities

The reduction in the RF wavelength at 3T also impacts on B_1 penetration, and often results in a non-uniform absorption across the patient. As expected,
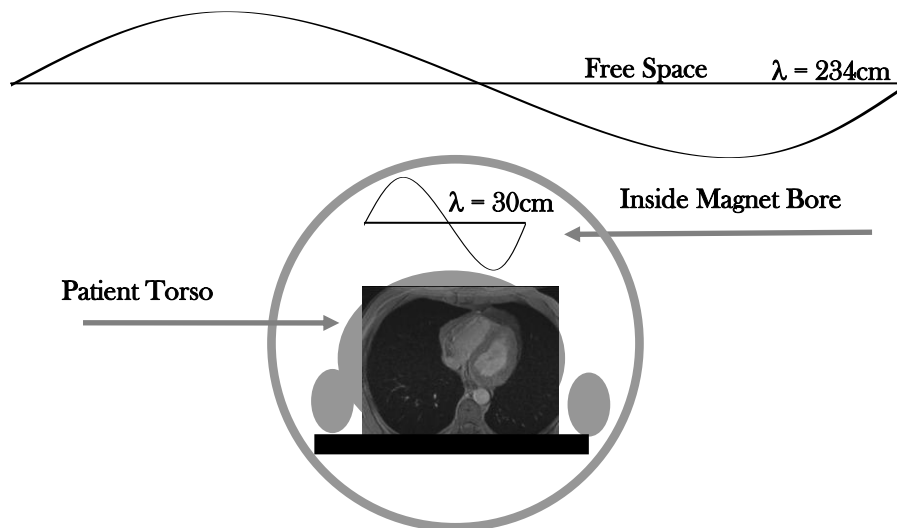
Figure 4.5 The dielectric effect can result in standing wave patterns within the patient's body cavity at 3.0T.

measurements have shown that the B_1 field is more inhomogeneous for cardiac imaging at 3.0T in comparison to 1.5T [14, 15]. This increases the likelihood of image artefacts and can also result in non-uniform flip angles across the imaging volume. In a recent study, flip angles and hence the RF power setting in CMRI, were found to be 20% lower than requested for a flip angle of 60° [16]. These incorrect power settings are problematic as they can result in the failure of magnetisation preparation pulses and consequently produce biased quantitative measurements [17].

4.7.5 Changes in Power Deposition and the Impact on SAR limitations

SAR thresholds are the same for 1.5T and 3T however the power required to create a fixed B_1 amplitude quadruples from 1.5T to 3.0T, due to the doubling in

frequency. By reciprocity, the energy deposited in the tissue of the patient will also quadruple.

$$SAR = \frac{P}{V} = \frac{\langle B^2 \rangle \omega_0}{Q\mu_0} \propto \int B_1^2 dt \qquad (4.12)$$

Where P = power, V = volume of the coil, Q is the Q factor of the coil and μ_0 is the permittivity of free space.

As discussed previously, increased receive bandwidths (BW$_r$) are commonly used at 3T in a bid to reduce chemical shift artefacts. However, by doubling the BW$_r$ you double the SAR. So, potentially SAR can increase by a factor of 8 from 1.5T and 3.0T. Other factors, such as the position of the patient with respect to the isocentre of the magnet and coil design, can also impact on SAR.

Fortunately, a range of options are available to reduce the amount of RF energy deposited in human tissue allowing the operator to remain within the SAR limits. For this reason, imaging at 3T often involves compromises between the number of applied RF pulses, their duration time (dT), the magnitude of the flip angle (α) and the pulse repetition time (TR).

$$\alpha \propto \int B_1(T)dT \qquad (4.13)$$

$$SAR \propto \frac{\alpha^2}{TR} \qquad (4.14)$$

Parallel imaging can limit the SAR, as can the right choice of pulse sequence. The reduced flip angle of gradient echo pulse sequences are preferential to the 90° and 180° flips angles used in spin echo sequences as they deposit less energy on the patient.

4.7.6 Field Inhomogeneities and Susceptibility

All MRI systems are defined in terms of their external magnetic field strengths. The homogeniety of these fields describes their uniformity and, hence their quality. Today's high field superconducting systems have extremely homogenous external fields, particularly in the isocentre of the bore (Table 4.4).

Table 4.4 Siemens Guaranteed Homogeniety of the External Field.

(DSV)	1.5T Avanto (ppm)	3.0T Trio (ppm)
50 cm	<1.50	<1.50
45 cm	<1.00	<0.50
40 cm	<0.75	<0.20
30 cm	<0.50	<0.10
20 cm	<0.25	<0.02
10 cm	<0.05	<0.002

This table contains guaranteed values based on a highly accurate 24-plane plot. DSV = Diameter Spherical Volume (x, y, and z direction).

Very small variations in the external field will always exist, even in an ideal magnet, however they are now so small in today's superconducting magnets that they are measured in parts per million (ppm).

4.7.7 Susceptibility Effects

Magnetic susceptibility (χ) is a measure of the response of a substance to an applied magnetic field. Substances are divided into one of three main groups depending on their susceptibilities: paramagnetic, diamagnetic and ferromagnetic. The extent of a substance's susceptibility is determined by the degree to which its electrons become magnetised and align with or against the external magnetic field.

Human tissue is ~99% diamagnetic. However, different human tissues exhibit different levels of magnetic susceptibility and this induces tiny internal gradients ($\Delta \mathbf{B_i}$) at the interface of different tissue types and between tissue and air-filled structures (such as the lungs). These gradients substantially increase the dephasing rate ($\Delta \phi$) of the spins on both sides of the interface. The phase change caused by magnetic susceptibility at time TE is given by:

$$\Delta \phi = -\gamma \cdot \Delta B_i \cdot TE \qquad (4.15)$$

The increased dephasing produces $\mathbf{B_0}$ field inhomogeneities ($\Delta \mathbf{B_0}$), signal loss, off resonance effects (where signals have the 'wrong' resonant frequency), and ultimately, image artefacts. Susceptibility induced inhomogeneities scale linearly with field strength, doubling between 1.5T and 3.0T [18].

$$\Delta B_0 = \chi B_0 \qquad (4.16)$$

Tissue-related susceptibility artefacts can be quite subtle on images, as the signal tends to be reduced rather than eliminated. These artefacts can be minimised in a number of different ways. For example, reducing the pixel size of an image makes it less likely that voxels will contain tissues with different susceptibilities. Another option is to restrict the dephasing time of the spins by selecting a short TE or opting for a spin echo pulse sequence with its 180° refocusing pulse.

4.7.8 Metal Artefact

Ferromagnetic materials, such as nickel, iron and cobalt, are strongly attracted to a magnetic field and become permanently magnetised when exposed to this environment. A small percentage of patients presenting for a CMRI exam will have ferromagnetic materials within their bodies, usually in the form of surgical clips and devices or shrapnel. These implants may experience a torque in the presence of B_0, and hence there are important safety issues regarding the management of such patients. This has been a challenge at 3T, as safety assessments established for imaging at 1.5T cannot be automatically extrapolated to 3.0T [19].
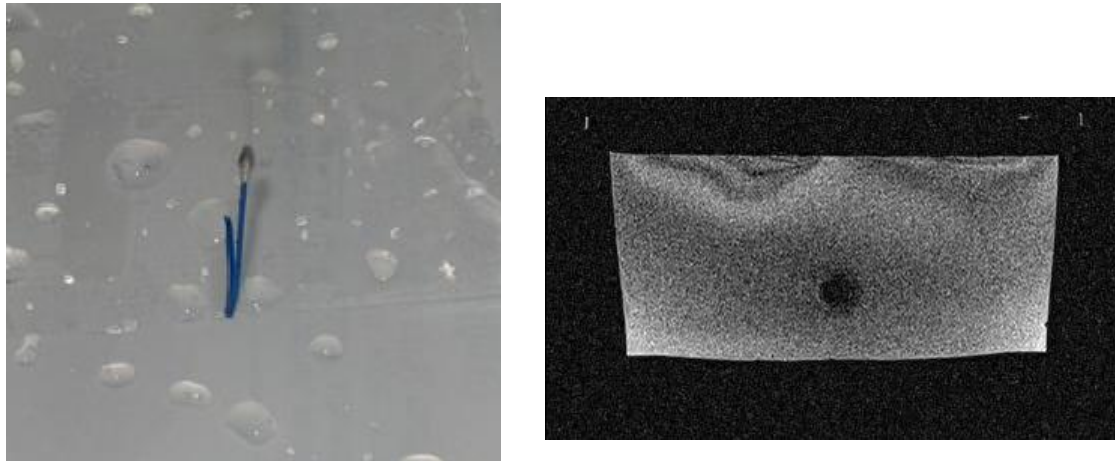
Figure 4.6 (a) A ferromagnetic Capio suture. (b) The image distortion caused by the suture at 1.5T .

However, information on the 'MRI compatibility' of medical implants and devices at 3.0T is becoming more readily available as more and more centres carry out routine imaging at this field strength.

Ferromagnetic materials also cause significant geometric distortions during imaging. This is commonly seen as an area of zero signal surrounded by one or two partial high intensity rims at the edges (Figure 4.6) [20].

4.7.9 Shimming

Hardware solutions such as active shimming can also reduce susceptibility artefacts by applying linear gradients to correct B_0 inhomogeneities. Recently, higher order shimming has been introduced that can improve magnetic field homogeneity in a specific region of interest such as the heart. This has been particularly beneficial at 3.0T.

4.7.10 Parallel imaging

As mentioned previously (3.1.4), parallel imaging speeds image acquisitions by utilising the additional spatial encoding information provided by phased array coil technology to reduce the number of time-consuming phase encoding steps needed to construct an image.

Parallel imaging techniques are beneficial at 1.5T and 3.0T as they reduce the length of the echo train, and thus reduce the build-up of phase errors. A disadvantage of this technology is that the reduced imaging time results in a decreased SNR that is approximately equal to the square root of the time saved. For example, by using parallel imaging to reduce a scan time by a factor of two, the SNR would be reduced by a factor of at least $\sqrt{2}$.

Parallel imaging at 3.0T has the potential to compensate for this reduction by exploiting the SNR gain at this field strength to reduce the imaging time by a factor of two whilst providing the same SNR available at 1.5T.

At present, parallel imaging methods are limited to acceleration factors of around three in most two-dimensional (2D) imaging situations at 3.0T. This is a result of the nonorthogonality of coil-encoding leads increasing the spatially varying noise amplification beyond the inherent increase in noise from undersampling only. However, recent work on dynamic imaging has

demonstrated the feasibility of acceleration factors greater than three with methods that exploit spatial and temporal data correlations jointly.

4.7.11 Coils

Both receiver-only and transmit-receive coils have to be tuned to the resonance frequency of the system they are used with, so coils used at 1.5T cannot be used at 3T. Although the number of accessory-receiving coils has been limited in the past, the coil availability problem is now completely resolved due to more engineering developments being applied to 3T.

4.7.12 The Magnetohydrodynamic Effect

Blood is an ionic fluid and when the ionic velocity vectors of flowing blood within large blood vessels lie perpendicular to a strong external magnetic field, a charge separation will occur. This results in the establishment of an electric field (Faraday's law). This interaction of flowing blood with the high external magnetic field is known as the Magnetohydrodynamic (MHD) effect [21].

The MHD effect only became of interest with the introduction of cardiac imaging, around the mid 1980s. This was due to the transverse alignment of the aortic arch with respect to the high external magnetic field.

The greatest impact from the MHD effect is during systole, when the flow of blood into the aortic arch is greatest. This phase of the cardiac cycle correlates with the S-T segment of the ECG trace (figure 4.7) and therefore, the MHD

effect can result in an elevation of the T wave. Imaging is designed to be triggered by each R wave, but if the T-wave is similar in magnitude to the R wave, imaging can be prematurely triggered resulting in image blurring artefacts.

Figure 4.7 The MHD effect can elevate the T-wave on the ECG trace to a similar magnitude to the R wave resulting in false triggering and image blurring.

The MHD effect is field-dependent and therefore myocardial motion suppression becomes more challenging at 3.0T in comparison to 1.5T as a result of the magneto-hydrodynamic effect.

4.7.13 Vector Cardiogram

Recently, vector cardiogram (VECG) has been introduced to CMRI. This technique greatly reduces the interference of the MHD effect on aortic flow by examining the 3D orientation of the ECG signal and using the calculated vector of the QRS complex as a filter mechanism. This permits electrical signals that occur at a similar timing in the cardiac cycle, or those of a similar magnitude,

but of a different vector to be excluded. This technique can reduce or eliminate the possibility of the T wave being misinterpreted as the R wave.

4.7.14 Contrast to Noise Ratio

Image contrast is defined as the absolute difference in signal intensities generated by two different tissue types (S_A-S_B). T1, T2, T2* relaxation rates and proton density provide the most basic contrast generating mechanism in MRI as they naturally vary with tissue type. A high contrast-to-noise (CNR) between two tissue types (CNR_{AB}) is desirable as it allows subtle signal differences between normal and diseased tissue (S_A-S_B) to be detected above the noise standard deviation (σ_{SD}).

$$CNR_{AB} = \frac{S_A - S_B}{\sigma_{SD}} = SNR_A - SNR_B \qquad (4.17)$$

The increased SNR at $3.0T$ should result in a higher CNR, although this is not guaranteed.

4.8 The Changes in Tissue Relaxation Times

Tissue relaxation rates are known to be dependent on field strength. Previous studies have highlighted an increase in T1 relaxation rates with increasing field strength [22–24] as the associated increase in Larmor frequency means fewer protons are tumbling at or near ω_0, so fewer protons are available to transfer energy efficiently to the lattice. As expected, T1 increases with field strength are

not consistent across all tissue types. For example, the T1 of myocardium was shown to increase by 43% from 1030msec at 1.5T to 1471msec at 3.0T, whilst the T1 of blood increased by 34% from 1441msec at 1.5T to 1932msec at 3.0T [25].

T2 relaxation rates are considered stable between 1.5T and 3.0T as the very small decreases found have no impact on imaging [25, 26]. However, an increased field strength impacts on T2* values to a much greater degree due to the effects on other parameters, particularly susceptibility.

The changes in relaxation rates need to be considered for the successful design and implementation of pulse sequences at higher fields. Sequence parameters such as such as the repetition time (TR), echo time (TE) and acquisition bandwidth need to be optimised for successful CMRI imaging at 3.0T [27].

4.9 Contrast Enhancement

The relaxation rates of gadolinium-based contrast agents have been shown to decrease with increasing field strength [28]. These changes slightly reduce the T_1 shortening caused by the contrast agent; however, this has little impact on imaging at 3.0T.

5. Cardiac Magnetic Resonance Imaging Protocols

5.1 Introduction

Each of the patients and volunteers discussed in chapters 6–9 of this thesis were imaged using a pre-selected CMRI protocol. Imaging protocols consists of a 'recipe' of pulse sequences that are specifically selected to answer a particular clinical or research question. This chapter provides a brief explanation of the basic physics behind two fast gradient echo techniques commonly used in cardiac MR imaging, known as True fast imaging with steady-state (TrueFISP) and Turbo fast low angle shot (TurboFLASH) (both Siemens Medical Solutions, Erlangen, Germany). Following on from this, the cardiac images acquired for this research using TrueFISP and TurboFLASH techniques are discussed along with the reasons for acquiring these images. Where appropriate, the clinical information obtained from these images is also detailed.

5.2 Fast Gradient Echo

TrueFISP and TurboFLASH are variations of the conventional gradient echo technique discussed in chapter 1 of this thesis. These techniques use very short TR values (TR<T2<T1 of the tissues) and small flip angles to shorten acquisition times. A consequence of the short TR value is that a small amount of transverse magnetisation exists at the end of each sequence cycle. TrueFISP and TurboFLASH differ in the way that they deal with this residual magnetisation.

5.3 TrueFISP

TrueFISP belongs to a class of sequences known as balanced steady-state in free precession (bSSFP). These techniques have transformed CMRI as they offer significant improvements on spatial and temporal resolution, coupled with higher tissue contrast, when compared to other CMRI sequences [1, 2]. Balanced SSFP sequences are defined by the coexistence of constant, non-zero longitudinal and transverse magnetisation vectors throughout the whole of the sequence cycle. In order to achieve this equilibrium position, and to enhance SNR, bSSFP techniques recycle the residual magnetisation.

5.3.1 Equilibrium

It takes several steps to establish a balanced steady-state. Initially, an $\alpha/2$ preparation pulse is applied to partially flip the longitudinal magnetisation vector (M_0) into the x–y plane, creating a transverse magnetisation vector (M_{xy}) (Figure 5.1).
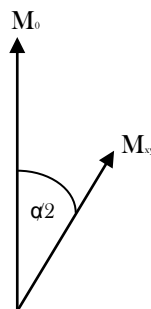
Figure 5.1 An $\alpha/2$ pulse partially flips the longitudinal magnetisation vector into the x–y plane.

After the RF pulse is withdrawn, M_{xy} begins to de-phase (decay) generating an FID. With no further intervention, the FID would rapidly decay away to zero due to several factors associated with relaxation and precession. These include T1 and T2 relaxation, the choice of flip angle (α), phase rotation angle (β), field in-homogeneities, susceptibility effects and gradient encoding. The decay process is halted by the rapid application of a -α pulse at TR/2 (TR/2 < T2*) (Figure 5.2) that generates both an FID and a spin (or Hahn) echo (Figure 5.3).
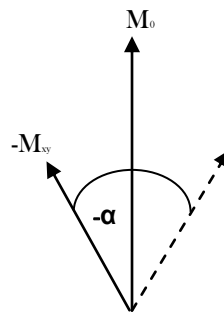
Figure 5.2 The preparation pulse is followed by a –α pulse at TR/2.

The -α pulse is followed by a train of ±α pulses, each separated by a time period TR. This creates a succession of FIDs and spin echoes. If the flip angle, phase and TR remain constant throughout each cycle, a steady-state can be established within a few TRs [3].
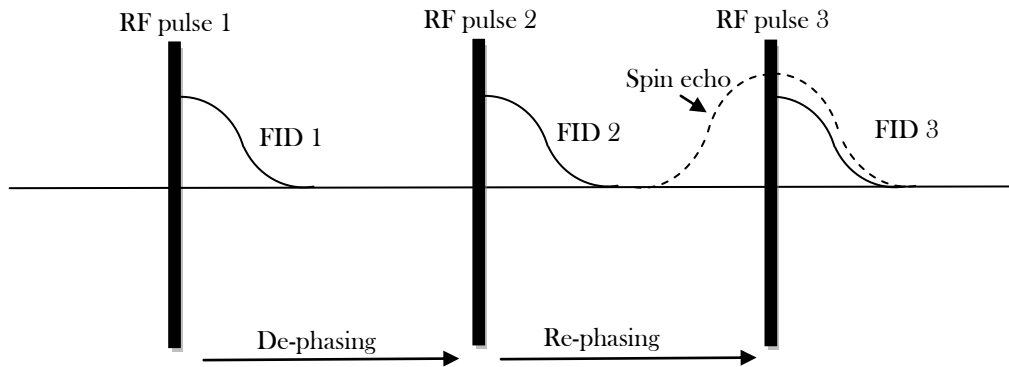
Figure 5.3 A steady-state can be established after a few TR periods.

5.3.2 Rewinder Gradient

As the de-phasing and re-phasing rates of individual spins are equal, the peak of the spin echo from the initial $\alpha/2$ pulse occurs at exactly the same time as the application of the third α pulse (and so on throughout the sequence) (Figure 5.3). This creates a potential problem as an MRI system cannot transmit an RF pulse and receive an echo signal at the same time due to hardware limitations. This issue is resolved by applying a rewinder gradient to prematurely refocus the transverse magnetisation. This ensures that each echo occurs prior to the next excitation pulse rather than during it (Figure 5.4).
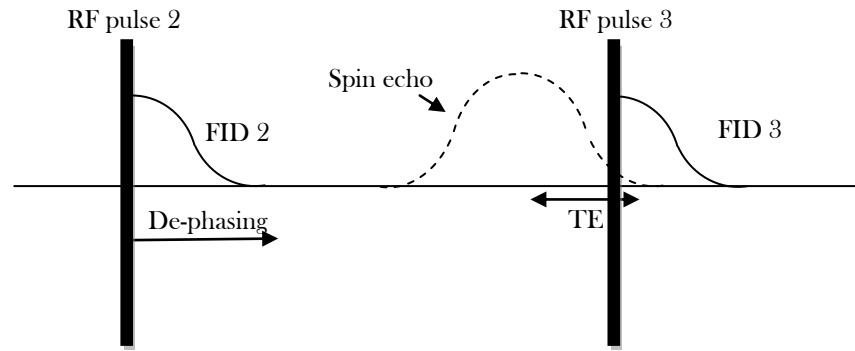
Figure 5.4 A rewinder gradient is applied to ensure the echo occurs before the application of the next RF pulse.

5.3.3 Spatial Encoding

TrueFISP is described as a 'balanced' SSFP sequence as each of the spatial encoding gradients are refocused (balanced) by gradients of equal and opposite polarity during the sequence cycle. This cancels any of the de-phasing effects that would normally be caused by the application of these gradients and ensures that the same precessional angle is achieved in each successive TR. This increases the available SNR. Hence, the only source of phase accrual during each TR comes from off-resonance precession.

5.3.4 The Signal

Once in equilibrium, bSSFP techniques produce two types of signal. The FID provides a signal with mixed T1 and T2* weighting whilst the spin echo provides a signal that is strongly T2 weighted and has negligible T2* contributions [4]. Consequently, the amplitude of the signal is dependent on the T1/T2 ratio of the different tissues, the repetition time (TR), and the flip angle

(α) of the RF excitation pulse. For a TR<<T1<<T2 the general solution for the signal intensity is (given without proof): [5]:

$$M_{ss} = M_p \frac{\sqrt{E_2(1-E_1)}\sin\alpha}{1-(E_1-E_2)\cos\alpha - E_1 E_2} \quad (5.1)$$

Where $E_{1,2} = e^{-TR/T1,T2}$, M_p is the proton density of the tissue and α is the flip angle.

5.3.5 Optimal Flip Angle

The optimal flip angle for bSSFP sequences can be calculated from [5]

$$\cos(\alpha) = \frac{T_1/T_2 - 1}{T_1/T_2 + 1} \quad (5.2)$$

With the signal generated being proportional to [6]:

$$M_{ss} = \frac{1}{2} M_p \sqrt{\frac{T_2}{T_1}} \quad (5.3)$$

5.3.6 Optimal Signal

An optimal signal can be obtained with bSSFP using flip angles in the range of 45°–80°. The choice of flip angle determines the degree of steady-state. A larger flip angle will result in a larger amount of residual transverse magnetisation and hence, the greater the degree of steady-state.

5.3.7 Artefacts

Because of the nature of SSFP sequences, they are very susceptible to artefacts caused by magnetic field in-homogeneities. Any non-uniformity in the main magnetic field can cause slight differences in the precessional frequencies of the spins in $M_{xy,}$ resulting in the spins having different de-phasing rates. This can prevent the transverse magnetisation vector from fully refocusing at the end of each sequence cycle. So rather than each M_{xy} vector adding constructively to create an enhanced signal, the phase differences result in the vectors adding destructively, which manifests as a dark banding artefact across the image (Figure 5.5) [5]. For this reason, cardiac imaging with bSSFP is more demanding at 3.0T than 1.5T due to the increased challenges of maintaining a homogenous field across the heart at this field strength.
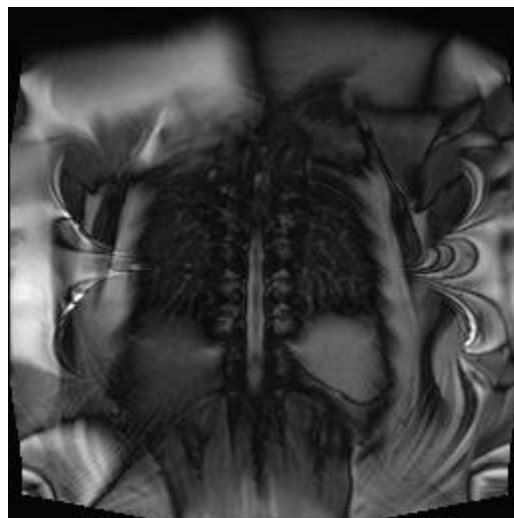
Figure 5.5 Magnetic field in-homogeneities can produce dark banding artefact on images.

5.4 TurboFLASH

TurboFLASH is described as a spoiled gradient echo sequence as an RF spoiler gradient is applied after each echo has been sampled to destroy residual transverse magnetisation and eliminate any T2 weighting. In addition to this, an inversion pulse (~100ms) is applied (followed by a delay) prior to imaging to improve spatial resolution and ensure that the images generated are heavily T1 weighted.

5.5 The Images

Most of the images obtained for the purpose of this research were acquired using bSSFP techniques. For example, each of our CMRI protocols begin with the acquisition of a series of reference, localiser, and cine images that are all acquired using bSSFP sequence.

5.5.1 Reference Images

Reference images allow the operator to accurately locate the patient or volunteer's heart within their chest cavity, as this is known to vary between individuals. These low resolution image slices are acquired rapidly (< 1sec) in the axial, coronal and sagittal planes.

5.5.2 The Localisers

Localiser images are acquired in the 2 chamber (2CH) (Figure 5.6a), 4 chamber (4CH) (Figure 5.6b) and short-axis (SA) (Figure 5.6c) views to satisfy an

agreement between the different imaging modalities that all cardiac images should be defined, oriented, and displayed using the true long axis of the left ventricle (4 chamber view) and selected planes orientated at 90° angles relative to it (2 chamber and short axis views). This standardisation was introduced in 2002 to ensure accurate and reproducible analysis of cardiac function and allow the comparison of functional data between the different imaging modalities.

Localiser images are acquired using a single shot SSFP pulse sequence. The 2CH localiser is planned using the axial reference image. The cut slice is positioned so that it lies in the middle of the left ventricle, parallel to the ventricular septum and roughly perpendicular with the plane of the mitral valve.

The 2CH localiser is then used to plan the 4CH localiser. The cut slice is positioned so that it lies through the centre of the left ventricle, perpendicular to the mitral plane and the apex of the heart. The resulting image is a double-oblique longitudinal axis view through the heart.
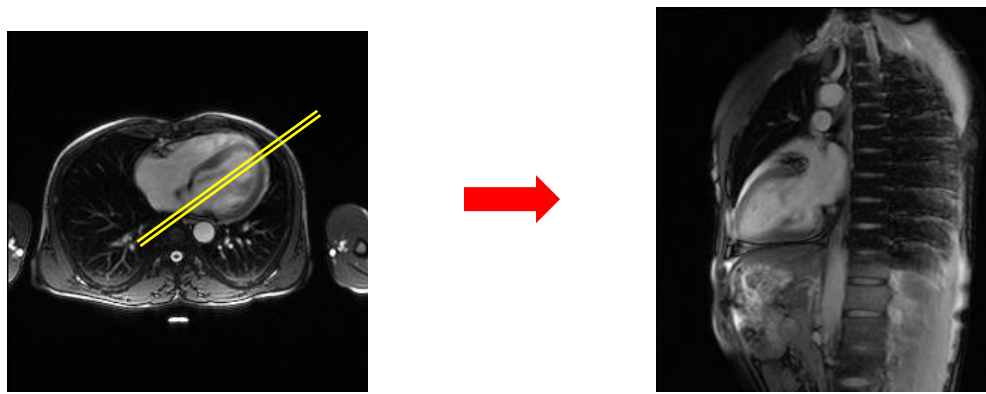
Figure 5.6a The reference axial image is used to plan the two chamber localiser.
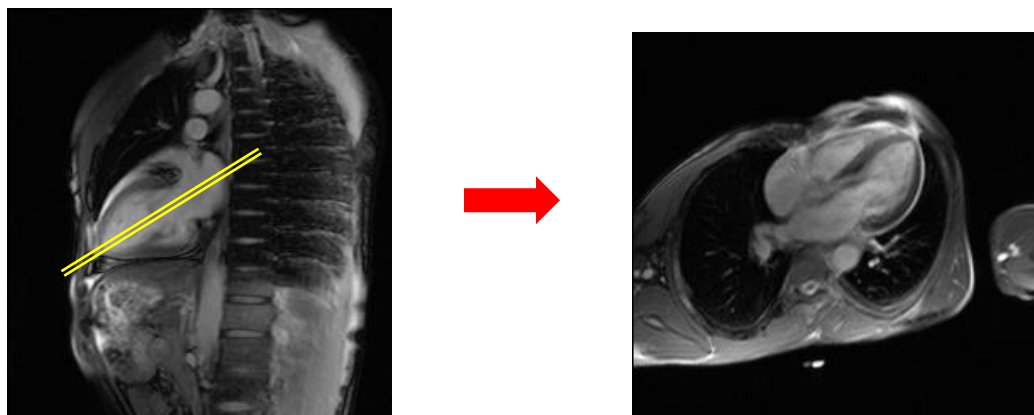
Figure 5.6b The two-chamber localiser is used to plan the four-chamber localiser.

The 2CH and 4CH localisers are then used to plan a series of seven short-axis localiser slices. The cut slices are positioned so that they lie perpendicular to the ventricular septum and parallel to the mitral plane on the 4CH localiser. The operator then ensures that the imaging plane also lies perpendicular to the 2CH localiser.
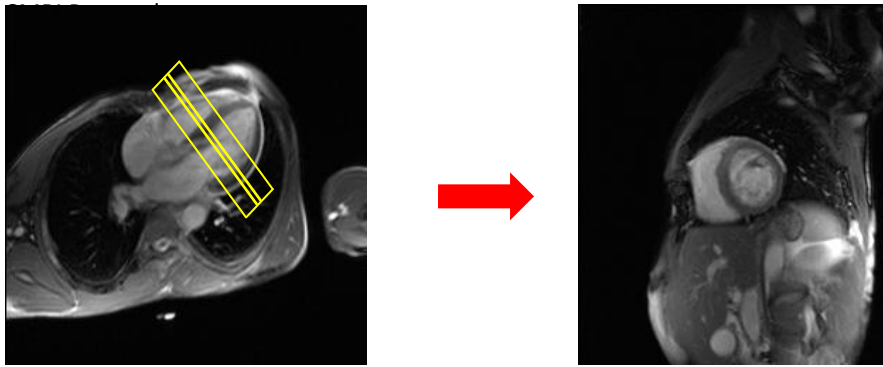
Figure 5.6c Five short axis slices are planned using the two- and four-chamber localisers.

5.6 Functional Imaging

The localiser images are used to plan a series of high-resolution, cardiac-gated breath-hold cine images in the 4CH (Figure 5.7a), 2CH (Figure 5.7b) and SA (Figure 5.7c) views. Each cine series contains 25 frames providing an ECG gated account of the heart as it moves through the different phases of the cardiac cycle.
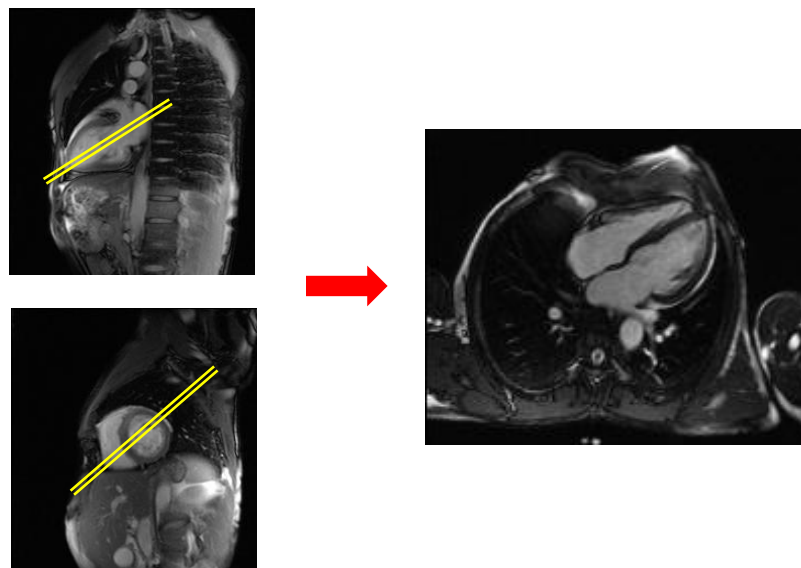
Figure 5.7a The four-chamber cine is planned using the two-chamber and short-axis localisers.
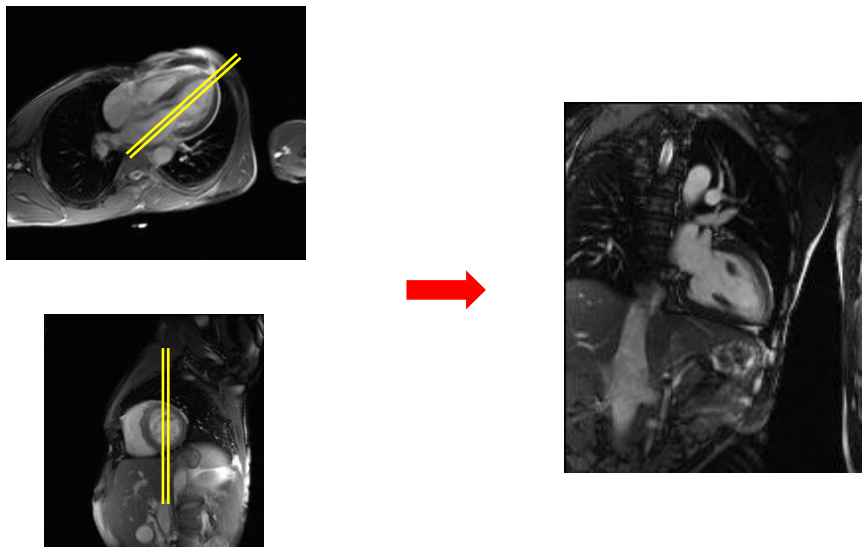
Figure 5.7b The two-chamber cine is planned using the short-axis localiser and the four-chamber cine.
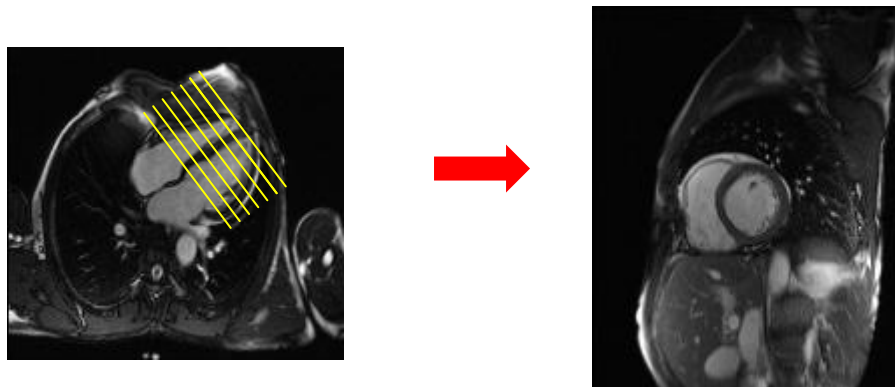
Figure 5.7c A stack of short-axis cine images are planned using the four-chamber cine. The angulations of the cut slices lie perpendicular to the two-chamber cine.

5.6.1 Clinical Information

The localiser, 2CH and 4CH cine images are used to assess overall cardiac morphology in terms of cardiac chamber orientation, pericardial, aortic and pulmonary arterial anatomy. The SA cine images provide a visual assessment of left ventricular (LV) and right ventricular (RV) movement and an assessment of cardiac function (Chapter 6).

5.7 First Pass Perfusion Imaging

First pass perfusion imaging plays a central role in the diagnosis, clinical management and prognosis of patients with known or suspected ischemic heart disease. First pass images are obtained using a 2D single-shot gradient echo technique (TurboFLASH) as it provides excellent visualisation of the first pass of a contrast agent as it transits through the cardiac chambers and into the myocardium (Figure 5.8).
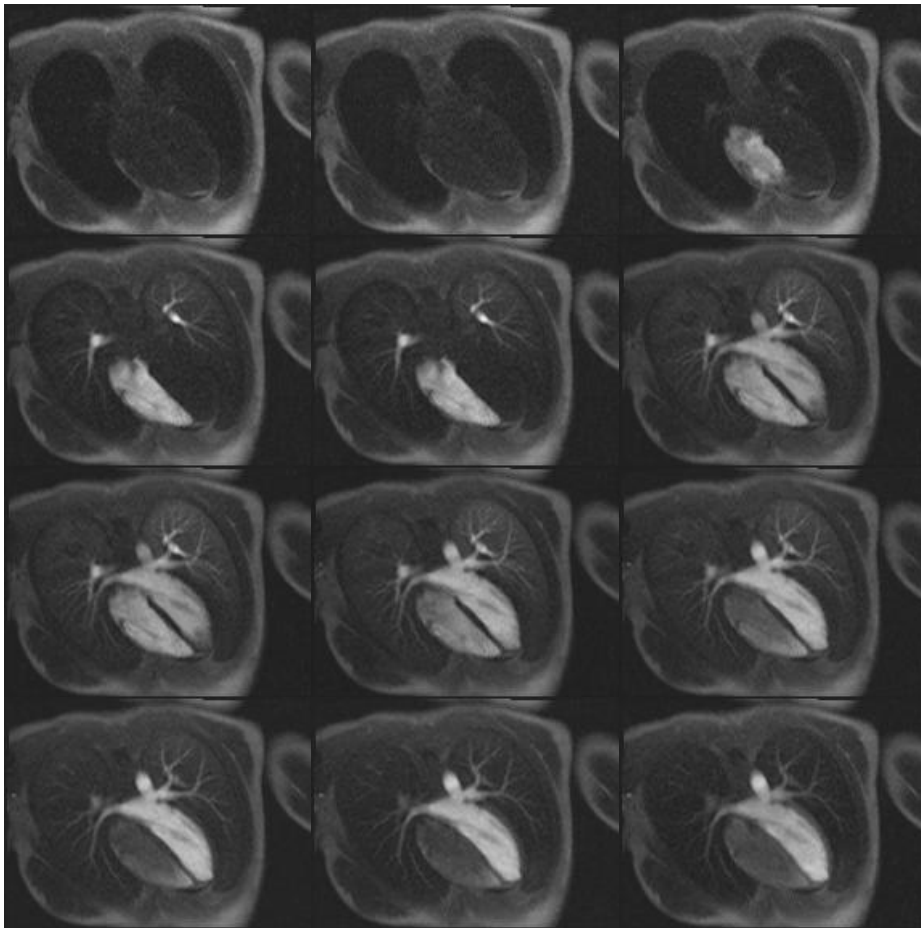
Figure 5.8 First pass perfusion images track a bolus of gadolinium-based contrast agent as it travel through the chamber of the heart and into the myocardium.

5.7.1 Clinical Information

First pass perfusion images are used to help detect any flow limiting lesions in the coronary arteries and therefore, provide an accurate assessment of the functional status of the myocardial microcirculation.

5.8 Post Processing of Cardiac Images

The stack of short-axis cine images discussed above is post-processed by an MRI physicist on a remote workstation using the manufacturer's software (Argus, Siemens Medical Solutions, Erlangen, Germany) to provide measures of end-diastolic volume (EDV), end systolic volume (ESV) stroke volume (SV), ejection fraction (EF), left ventricular mass (LVM) and cardiac output (CO).

5.8.1 Cardiac Volumes

End-diastolic and end-systolic volumes provide a measure of the volume of blood in the cardiac chambers when the heart is most dilated (diastole) and most contracted (systole). Stroke volume (SV) quantifies the difference between EDV and ESV and is therefore a measure of the volume of blood ejected from the chamber with each heartbeat.

5.8.2 Cardiac Mass

Ventricular mass is a measure of the ventricular myocardium from the base of the ventricle to the apex of the heart. The left ventricle has a much thicker myocardium than the other chambers of the heart due to its increased workload (Chapter 2).

5.8.3 Cardiac Output and Ejection Fraction

The volume of blood pumped out of the ventricle each minute is termed the cardiac output (CO). It is the product of the SV and the number of times the heart beats per minute (heart rate). The ejection fraction (EF) quantifies the percentage of blood pumped out of the cardiac chamber with each heart beat. It is calculated using the SV and the EDV (5.1). The function of the heart is most commonly defined by the ejection fraction.

$$EF = \frac{EDV - ESV}{EDV} = \frac{SV}{EDV} \quad (5.1)$$

Quantitative analysis of cardiac function traditionally focuses on the left ventricle (LV) of the heart, as it is the main pumping chamber. However, it is also possible to provide an equivalent assessment of right ventricular (RV) function (Chapter 6) and left atrial (Chapter 8) using the same short-axis stack of images.

It is essential that short-axis image analysis is accurate and reproducible as the measures this semi-automated process provides are crucial in the evaluation of disease progression, response to therapy and appropriate clinical/surgical intervention. For this reason, intra- and inter-observer reproducibility measurements are an essential requirement of any functional CMRI study.

References

1. Oppelt A, Graumann R, Barfub H, Fischer H, Hartl W, Schajor W. FISP-a new fast MRI sequence. Electromedica 1986; 54: 15–18.

2. Carr JC, Simonetti O, Bundy J, Li D, Pereles S, Finn JP. Cine MR angiography of the heart with segmented true fast imaging with steady-state precession. Radiology 2001; 219: 828–834.

3. Carr H. Steady-state free precession in nuclear magnetic resonance. Physical Review 1958; 112: 1693–1701.

4. Govind GB, Babyn PS, Fankharia BG, Chen H-LM, Manohar MS. Steady-State MR Imaging Sequences: Physics, Classification, and Clinical Applications. Radiographics 2008; 28: 1147–1160

5. Scheffler K, Lehnhardt S. Principles and applications of balanced SSFP techniques. European Radiology 2003; 13: 2409–2418

6. Bitar R, Leung G, Perng R, Tadros S, Moody AR et al. MR Pulse Sequences: What every radiologist wants to know but is afraid to ask. Radiographics 2006; 26: 513–537.

6. Assessment of clinical differences at 1.5T between quantitative right and left ventricular volumes and ejection fractions using MRI

6.1 Introduction

Cardiac MRI (CMRI) has excellent accuracy and reproducibility and is currently considered the gold standard modality for the assessment of left ventricular (LV) function and mass (LVM) [1, 2]. It is known that clinical assessment of right ventricular (RV) function can provide independent diagnostic and prognostic value in many congenital and acquired heart diseases [3]. The three-dimensional (3D) volume acquisition of CMRI is well suited for determining right ventricular (RV) parameters [4], with previous studies [5, 6] establishing good RV reproducibility in healthy subjects and patients with various cardiac pathologies. However, CMRI assessment of right ventricular function is often neglected in the evaluation of cardiac function as the right ventricle's complex 3D shape, [7] heavy trabeculations and irregular endocardial border all make assessment of right ventricular parameters more challenging.

6.2 Aims

This study had two aims:

1. To perform right ventricular (RV) and left ventricular (LV) analysis on the short-axis images of three distinct clinical cohorts with the hypothesis that the inclusion of RV data may generate a more informative characterisation of cardiac function.

2. To assess the reproducibility between a novice segmenter, with 2 months experience of cardiac MRI (CMRI) analysis (physicist 1) and an experienced segmenter with 4 years CMRI analysis experience (physicist 2).

6.3 Cohorts

The thirty subjects enrolled in this study were individually assigned to one of three distinct cohorts, each containing nine Males (M) and one female (F):

- Group A, consisting of normal healthy volunteers (NHV), with a mean age of 32 and age range of 24–42 years, selected from individuals with no known cardiac history or underlying health condition.

- Group B, consisting of patients diagnosed with congestive heart failure (CHF), with a mean age of 73 and age range of 59–83 years, selected from individuals clinically diagnosed with left ventricular systolic dysfunction as demonstrated using echocardiography.

- Group C, consisting of patients diagnosed with left ventricular hypertrophy (LVH), with a mean age of 65 and age range of 52–78 years, selected from individuals clinically diagnosed by echocardiography.

6.4 Acquisition Protocol

All magnetic resonance imaging was performed on a 1.5 Tesla whole-body system (Magnetom Avanto Scanner, Siemens Medical Solutions, Erlangen, Germany). A combination of body matrix and spine matrix radio frequency coils and a two-dimensional, prospective cardiac-gated, breath-hold, segmented True-FISP Cine sequence were used to acquire a series of standard short-axis plane images, from the base of the ventricle to the apex of the heart. The imaging parameters used were: TR 38.25 msec, TE 1.08 msec, and flip angle (60°–70°). Acquisition time was reduced using parallel imaging acceleration factor (GRAPPA) of two, allowing one or two slices to be acquired per breath-hold, depending on patient/volunteer ability to sustain breath-hold. A slice thickness of 6mm and inter-slice gap of 4mm was used consistently throughout this study. The selected in-plane resolution was 192 pixels over an optimal field of view (FOV) ranging from 340 to 450 mm, depending on patient/volunteer size.

6.5 Image Analysis

Images were transferred to a remote Leonardo workstation where analysis was performed using ARGUS software (version VA60C; Siemens Medical Solutions, Erlangen, Germany) by two MRI segmenters. Each segmenter independently defined endocardial and epicardial myocardial borders on all LV images from base to apex, corresponding to end-diastole (ED) and end-systole (ES). On RV

images, endocardial borders were defined independently from base to apex, corresponding to ED and ES (Figure 6.1).
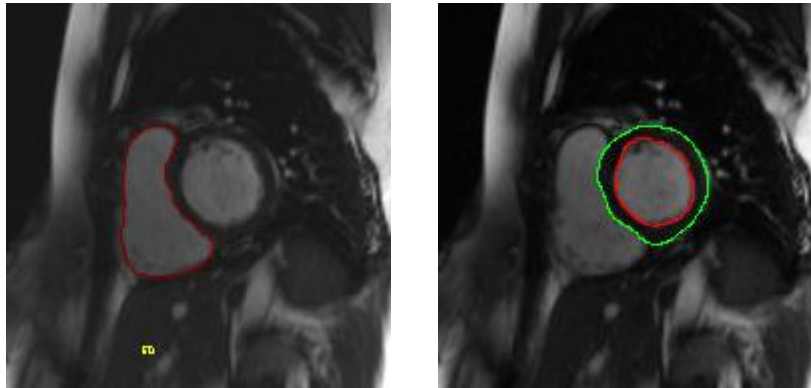
Figure 6.1 Contours were defined independently on the right and left ventricles.

Segmentation rules defining appropriate inclusion and exclusion of papillary muscles as well as appropriate basal slice selection were discussed prior to analysis with the aim of providing consistency between segmenters. In cases where it was impossible to distinguish the papillary muscle structure from the endocardial boundary it was agreed that those papillary muscles would be included within the endocardial contour.

6.6 Statistical Analysis

Statistical analysis was performed on data using SPSS (Chicago, Illinois, USA) in order to test for any significant changes in the parameters of end-diastolic volume (EDV), end-systolic volume (SV), stroke volume (SV) and ejectin fraction (EF) between the normal healthy volunteers and the two patient

cohorts. The mean values obtained by segmenters for both patient cohorts were compared to the mean values obtained for the healthy volunteers, using the paired t-test and assuming unequal variances. There were no systematic differences in the values obtained by the individual segmenters.

6.7 Results

Mean values ± SD were calculated for the left and right ventricular parameters of EDV, ESV, SV and EF using the individual values obtained by each segmenter. The results obtained by segmenter 1 for each clinical cohort are displayed in Table 6.1.

Table 6.1 Mean Values ± Standard Deviation (SD) for the LV and RV parameters of each cohort.

Left Ventricle			
Cohort (n=10)	NHV	CHF	LVH
LV EF ± SD (%)	66.0 ± 6.4	30.3 ± 6.1	74.1 ± 7.6
LV EDV ± SD (ml)	149.4 ± 32.2	244.6 ± 60.7	126.3 ± 42.4
LV ESV ± SD (ml)	52.1 ± 18.8	158.6 ± 52.4	34.5 ± 15.0
LV SV ± SD (ml)	97.3 ± 15.8	65.9 ± 15.4	91.8 ± 29.5
Right Ventricle			
Cohort (n=10)	NHV	CHF	LVH
RV EF ± SD (%)	52.0 ± 4.6	45.0 ± 7.8	57.6 ± 6.4
RV EDV ± SD (ml)	177.1 ± 28.3	135.94 ± 36.8	141.6 ± 40.7
RV ESV ± SD (ml)	85.5 ± 20.1	74.7 ± 23.0	59.9 ± 19.6
RV SV ± SD (ml)	91.3 ± 10.8	61.3 ± 18.5	81.7 ± 26.4

The ranges detailed in Table 6.1 fell within the ranges obtained by other groups carrying out similar work [5, 6]. Inter-observer reproducibility between segmenters, for each parameter, demonstrated a strong positive Pearson correlation (t-test), as detailed in Table 6.2.

Table 6.2 Inter-observer Reproducibility.

Inter-Observer	NHV	CHF	LVH
LV EF (P-Value)	0.98	0.89	0.91
RV EF (P-Value)	0.80	0.91	0.96
LV SV (P-Value)	0.96	0.80	0.96
RV SV (P-Value)	0.87	0.79	0.95

In all but one parameter, the diseased hearts displayed a larger range of values than those of the normal healthy volunteers. Ejection fraction values clearly varied to a much greater extent with disease than stroke volume values, as demonstrated in Table 6.1.

When compared to the NHV group, patients with congestive heart failure exhibited a reduction in ejection fraction and stroke volume values for both left and right ventricles, whilst patients with left ventricular hypertrophy displayed elevated ejection fraction values but reduced stroke volume values for both ventricles.

It was established that the CHF cohort demonstrated a significant reduction in ejection fraction and stroke volume values for both left and right ventricles

when compared to the NHV. The LVH cohort demonstrated a significant increase in ejection fraction values but no significant change in stroke volume values for both ventricles (Table 6.3).

Table 6.3 The differences in the values obtained for the cardiac parameters of each cohort were compared using a student's t-test.

t-test values (LV)	LV EF	LV EDV	LV ESV	LV SV
NHV v CHF	<0.001	<0.005	<0.001	<0.001
NHV v LVH	<0.05	0.1	<0.05	0.6
CHF v LVH	<0.001	<0.001	<0.001	<0.05
t-test values (RV)	RV EF	RV EDV	RV ESV	RV SV
NHV v CHF	<0.05	0.01	0.28	<0.001
NHV v LVH	<0.05	<0.05	<0.05	0.34
CHF v LVH	<0.001	0.74	0.1	0.06

Overall, the most significant change in parameter was the reduction in CHF LV EF which, when compared to the NHV cohort, showed a dramatic reduction of $p = 0.00000000002$. This significant change led to the CHF patients in this study typically displaying a greater RV ejection fraction than LV ejection fraction (Figure 6.2). The increase in EF values for the LVH cohort was more significant for the right ventricle than for the left.
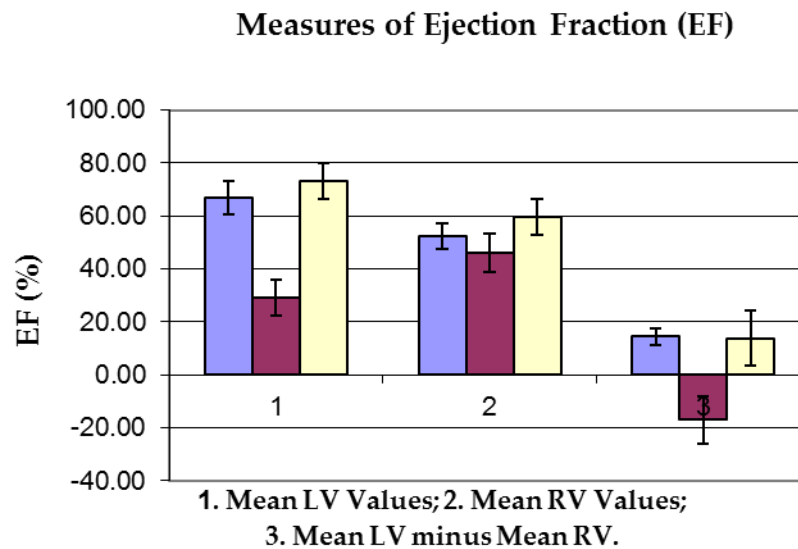
Figure 6.2: Displays: (1) Measures of LV EF, (2) Measure of RV EF, (3) LV minus RV EF. Blue = NHV; purple = CHF, white = LVH.

6.8 Discussion

Individuals were selected for each cohort based on their previous medical history. Although CHF patients can present with normal LV EF, the CHF patients selected for this study all had ejection fractions < 40%.

6.8.1 Reproducibility

Inter-observer reproducibility between segmenters was sufficiently low for a clinical study. Ejection fraction values proved more robust to inter-observer variation than stroke volume values. This was particularly evident when there was a discrepancy between segmenters as to the appropriate choice of basal slice selection in n = 4 datasets. Also, the majority of data sets used in this study were of good diagnostic quality, however in n = 3 cases poor image quality led to a slightly larger than expected variation in values between segmenters. A

decision was made to include these data sets in this study as it was believed that it led to a more realistic interpretation of a true clinical setting.

6.8.2 Significant Changes in Cardiac Parameters

The parameter of SV changed equally in the left and right ventricles of the CHF cohort when compared to the NHV cohort, with both ventricles showing significant changes. Significant changes in EF were also found in this cohort; however the change in EF was much more significant in the left ventricle than the right ventricle. The small reduction found in SV for the LVH cohort was not significant when compared to the NHV. The changes in EF in LVH cohort were found to be significant with the RV changing more significantly than the LV when compared to the NHV.

6.9 Conclusion

Our investigation has shown that ventricular analysis is accurate and reproducible even for the novice segmenter. It has also demonstrated that in addition to LV changes, RV function can display a more significant change than LV function in different clinical conditions. This finding provides further information on the simultaneous function of both ventricles that may be of assistance in guiding appropriate clinical intervention.

References

1. Koskenvuo JW, Karra H, Lehtinen J, Niemi P, Pärkkä J et al. Cardiac MRI: accuracy of simultaneous measurement of left and right ventricular parameters using three different sequences. *Clinical Physiology and Functional Imaging* 2007; **27:** 385–93.

2. Catalano O, Corsi C, Antonaci S, Moro G, Mussida M et al. Improved reproducibility of right ventricular volumes and function estimation from cardiac magnetic resonance images using level-set models. *Magnetic Resonance in Medicine* 2007; **57:** 600–5.

3. Beygui F, Furber A, Delépine S, Helft G, Metzger JP et al. Routine breath-hold gradient echo MRI-derived right ventricular mass, volumes and function: accuracy, reproducibility and coherence study. *The International Journal of Cardiovascular Imaging* 2004; **20:** 509–16.

4. Haddad F, Hunt SA, Rosenthal DN, Murphy DJ. Right Ventricular Function in Cardiovascular Disease, Part I: Anatomy, Physiology, Aging, and Functional Assessment of the Right Ventricle. *Circulation* 2008; **117:** 1436–48.

5. Alfaki K, Plein S, Thiele H, Jones T, Ridgway JP et al. Normal Human Left and Right Ventricular Dimensions for MRI as Assessed by Tirbo Gradient Echo and Steady-State Free Precession Imaging Seqences. *Journal of Magnetic Resonance Imaging* 2003; **17:** 323–9.

6. Hudsmith LE, Petersen SE, Francis JM, Robson MD, Neubauer S. Normal human left and right ventricular and left atrial dimensions using steady state free precession magnetic resonance imaging. *Journal of Magnetic Resonance Imaging* 2005; **7:** 775–82.

7. Coghlan JG, Davar J. How should we assess right ventricular function in 2008? *European Heart Journal Supplements* 2007; **9:** H22–H28.

7. Normal Ranges of Left Ventricular Functional Parameters at 3 Tesla

7.1 Part 1

The prevalence of heart disease in the general population rises with increasing age. Consequently, disease-related functional changes generally become problematic in individuals over the age of 60 years. In the research setting, it is common practice to quantify the magnitude of these changes by post-processing the patient or volunteer's CMRI short-axis cine images (Chapter 5) and comparing the calculated values with those of 'normal healthy' volunteers.

Volunteers are considered to be normal and healthy if their calculated values of cardiac function fall within the ranges provided by the scanner manufacturer (Siemens Medical Solution, Erlangen, Germany) (Table 7.1). Any values that fall out with these ranges are considered abnormal and will therefore, be taken into consideration for the diagnosis, management and prognosis of the individual.

The ranges provided by Siemens are generous. They are stratified for gender but not for age or field strength. This may be considered a limitation as a recent large (n = 400) multi-centre study, in which volunteers were divided by age, gender and ethnicity, [1] detected natural age related changes in cardiac function, which varied between race and gender. These findings highlighted a need to accurately determine age- and gender-specific normal ranges of cardiac

function for local populations, as this may allow a more accurate assessment of cardiac function in patient and volunteer groups.

Table 7.1 The normal ranges of cardiac function provided by Siemens Medical Solutions for images acquired at 1.5T and 3.0T.

Calculated Parameter	1.5T Female	1.5T Male	3.0T Female	3.0T Male
Ejection Fraction (%)	56–78	56–78	56–78	56–78
End-diastolic Volume (ml)	52–141	77–195	52–141	77–195
End-systolic Volume (ml)	13–51	19–72	13–51	19–72
Stroke Volume (ml)	33–97	51–133	33–97	51–133
Cardiac Output (l/min)	2.65–5.98	2.82–8.82	2.65–5.98	2.82–8.82
LV Mass at End-diastole (g)	75–175	118–238	75–175	118–238

Several other single-centre studies have produced normal ranges of cardiac function (Table 7.2). But these studies have been limited by their small cohort size [2–5] and/or limited age stratification [6–9].

Hence, the initial aim of this study was to acquire and post-process the short-axis cine images for 100 normal healthy volunteers (NHV) at 3.0T with the aim of:

- highlighting age and gender specific trends in the normal ranges of left ventricular (LV) ejection fraction (EF), end diastolic volume (EDV), end systolic volume (ESV), stroke volume (SV) and LV mass at end diastole (LVM) for our local population;

- comparing the ranges obtained for our local population with the universal ranges provided by Siemens.

7.2 The Normal Healthy Volunteers

A total of 100 informed and consenting normal healthy volunteers were recruited for this study. Those aged 40 years and over were chosen from an 'at risk' population of healthy volunteers participating in a large single-centre study* whilst the younger volunteers were recruited from healthy members of staff.

7.2.1 Exclusion Criteria

Exclusion criteria included any previous cardiac event or recognised cardiac disease, known alcohol abuse, pregnancy, claustrophobia, and any other known contraindication to MRI.

7.2.2 The Cohorts

The healthy volunteers were sub-divided into the following age and gender specific cohorts (Table 7.2).

Table 7.2 The healthy volunteers were sub-divided into small age- and gender-specific ranges.

Cohort	Female NHV(n)	Male NHV (n)
20–39 years	10	10
40–49 years	10	10
50–59 years	10	10
60–69 years	10	10
70+ years	10	10

7.3 Imaging Parameters

Each volunteer was imaged using a 3T Magnetom Trio Scanner (Siemens, Erlangen, Germany) and a spine matrix and six element body array matrix coil. Multi-slice short-axis images (slice thickness 6mm, gap 4mm) were acquired from the base to the apex of the left ventricle using a cardiac-gated segmented cine TrueFISP sequence, 173×256 matrix, TR 3.2ms, TE 1.5ms, flip angle 50°, and average field of view 140×171mm (depending on volunteer size) and a parallel imaging (GRAPPA) acceleration factor of 2.

7.3.1 Image Optimisation

Cardiac imaging proved more challenging at 3.0T than at 1.5T due to chemical shift artefact, SAR limitations, the magnetohydrodynamic effect and increased static field (B_0) and transmit radiofrequency field (B_1) in-homogeneities (Chapter 4). To enable images of good diagnostic quality to be obtained for this study, two additional techniques were introduced that are not required for cardiac imaging at 1.5T.

7.3.2 Localised Shimming

The increased field inhomogeneities at 3.0T demand a more precise shimming method. This was achieved by performing a localised volume (green box) shim over the heart region (Figure 7.1).
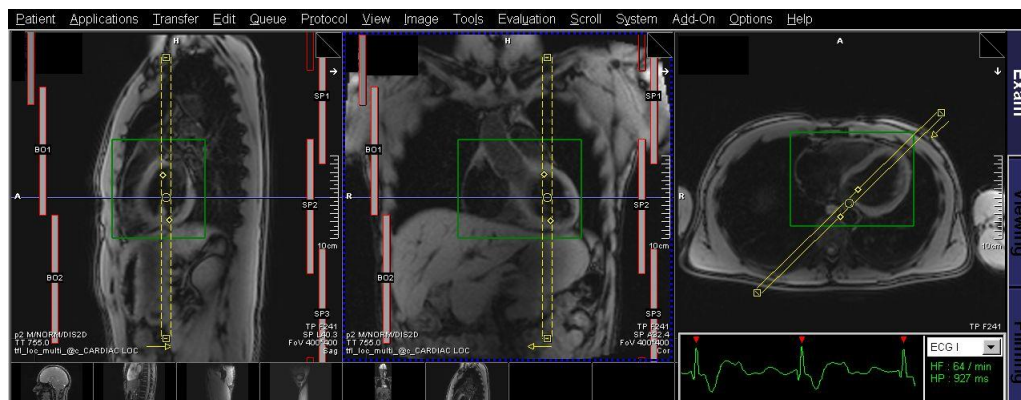
Figure 7.1 A volume shim is performed prior to the acquisition of all cardiac images at 3T.

7.3.3 Frequency Scout

Even after volume shimming the increased B_0 inhomogeneities proved particularly troublesome for steady-state sequences (Chapter 5). Small frequency shifts considerably reduced the transverse steady-state magnetisation, resulting in dark banding artefact across the images. It was not always possible to avoid these artefacts, but it was usually possible to move them out of the region of interest (ROI) by applying a frequency offset. The required frequency offset was chosen by performing a frequency scout to provide the operator with a series of images, each obtained at an incremental frequency (Figure 7.2). This allowed the centre frequency to be visually determined.
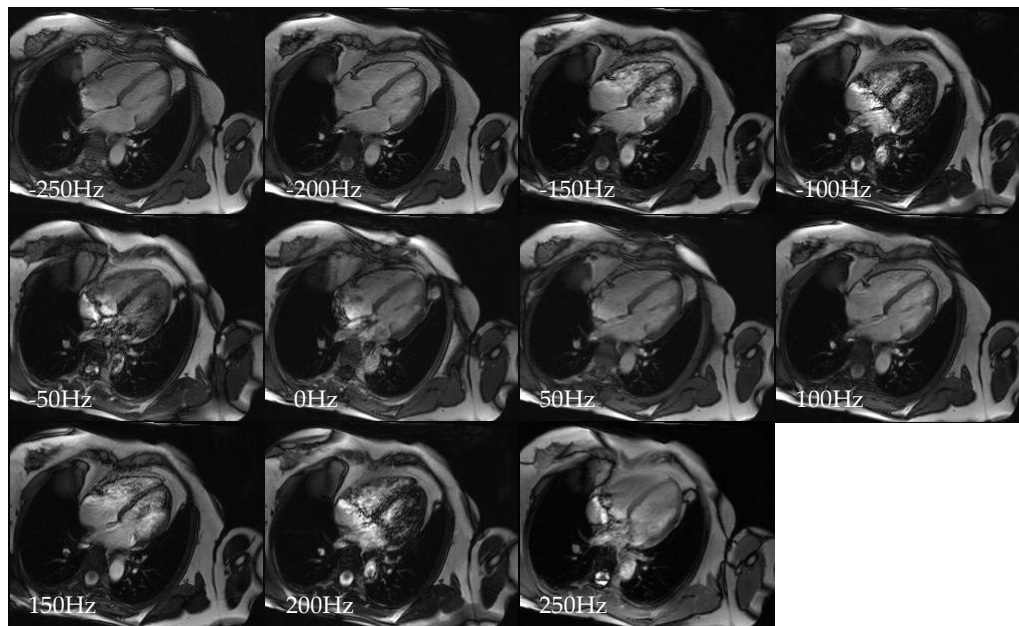
Figure 7.2 A frequency scout provides a series of images rapidly acquired at incremental frequencies.

7.4 Image Analysis

Image analysis was performed on a Siemens multi-modality work station using ARGUS software (Siemens, version VB15). Semi-automated placement of endocardial and epicardial borders was completed on all slices pertaining to end-diastole and end-systole. Statistical analysis was carried out using Sigma Plot 10.0 statistical analysis package (SSI, San Jose, California).

7.5 Calculated Values of Cardiac Function for the Age- and Gender-Defined Cohorts

All images were successfully acquired over an 18-month period. The mean quantitative values (± standard deviation (SD) of EF, EDV, ESV, SV and LVM for the healthy volunteers are listed in Tables 7.3 (age-defined females) and 7.4 (age defined males).

Table 7.3 Mean values ± SD for each age defined female cohort

Female (NHV)	20–39 years	40–49 years	50–59 years	60–69 years	70+ years
EF ± SD (%)	66.6 ± 6.2	67.9 ± 3.5	71.7 ± 7.0	72.2 ± 4.5	76.6 ± 4.51
EDV ± SD (ml)	131.9 ± 12.3	124.4 ± 23.3	119.1 ± 19.9	104.3 ± 13.6	92.5 ± 11.9
ESV ± SD (ml)	44.3 ± 10.9	39.8 ± 7.1	34.1 ± 11.6	29.0 ± 5.5	21.87 ± 5.8
SV ± SD (ml)	87.6 ± 9.6	84.6 ± 18.2	84.9 ± 13.5	75.3 ± 11.0	70.62 ± 8.0
LV mass ± SD (g)	89.7 ± 8.1	89.8 ± 22.4	88.61 ± 14.2	84.6 ± 13.0	89.11 ± 6.4

Table 7.4 Mean values ± SD for each age defined male cohort

Male (NHV)	20–39 years	40–49 years	50–59 years	60–69 years	70+ years
EF ± SD (%)	66.6 ± 6.2	68.4 ± 6.7	70.4 ± 6.1	68.8 ± 6.8	69.15 ± 6.8
EDV ± SD (ml)	131.9 ± 12.3	174.8 ± 19.2	158.0 ± 23.5	144.1 ± 29.6	128.9 ± 33.3
ESV ± SD (ml)	44.3 ± 10.9	55.5 ± 13.8	47.7 ± 15.3	46.1 ± 16.1	40.6 ± 16.5
SV ± SD (ml)	87.64 ± 9.6	119.3 ± 17.5	110.3 ± 11.9	98.0 ± 17.8	88.3 ± 20.0
LV Mass ± SD (g)	89.7 ± 8.1	147.7 ± 17.1	145.1 ± 32.5	124.2 ± 23.4	122.4 ± 23.4

7.6 Visual Analysis

An initial visual comparison of the images failed to highlight any significant structural differences between the age and gender defined cohorts (Figure 7.3).
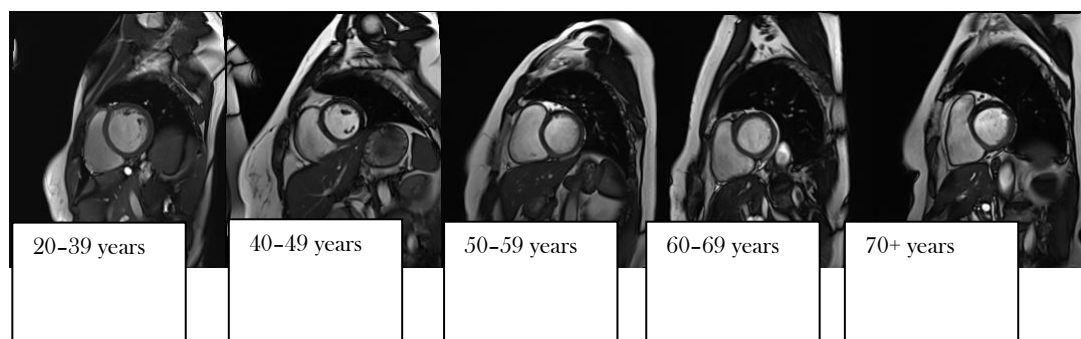
Figure 7.3 A visual assessment of the female cohorts with age.

7.7 Discussion

When the volunteers were defined into age- and gender-specific cohorts, the female volunteers displayed greater age-related reductions in their EDV and ESV than the male volunteers (30% v 22% and 50% v 25% respectively). However, all age- and gender-specific cohorts displayed similar reductions (20%) in stroke volume values over time. In addition to this, the female age-specific volunteers demonstrated a significant increase in ejection fraction values (66.7% to 76.6%, $p < 0.05$) throughout the ageing process whilst the EF values of the age-defined male cohorts remained relatively consistent (68.4% to 69.2%, $p \gg 0.05$).

Conversely, age- and gender-specific measures of LV mass remained stable throughout the aging process for the female cohorts but reduced significantly for male cohorts (133.6g to 122.4g, $p < 0.05$) over the same period. These observations closely reflect previous autopsy findings where males demonstrated decreasing left ventricular mass and progressive left ventricular myocyte loss with increasing age but female values remained constant [10].

7.8 Conclusion

This study demonstrated that, in addition to gender, age has a significant effect on the calculated mean LV quantitative parameters of our local population and

that these subtle age-related changes lie hidden in the generous ranges provided by Siemens.

7.9 Part 2

Armed with this information, the final part of this study aimed to determine if comparing the mean values obtained from age- and gender-matched patient and NHV cohorts would provide a more informative assessment of cardiac function than that of the gender-specific ranges currently used.

7.10 The Cohort

A small cohort of 7 female (mean age and range = 54, 39–62 years) systemic lupus erythematosus patients were selected for this investigation.

7.11 Image Analysis and Post-processing

A short-axis stack of cine images was obtained for each SLE patient using identical imaging parameters to those detailed above for the healthy volunteer cohort. The images were then post-processed to obtain the calculated values of cardiac function detailed in Table 7.5.

Table 7.5 The calculated values of cardiac function for the SLE cohort.

SLE Patient	EF (%)	EDV (ml)	ESV (ml)	SV (ml)	LV Mass (g)
1	66.0	107.6	36.6	71.0	89.7
2	70.7	127.5	37.4	90.1	88.6
3	73.7	138.1	36.4	101.8	107.3
4	72.8	105.4	28.7	76.7	95.7
5	73.0	86.9	23.5	63.5	85.1
6	80.4	82.1	16.1	66.0	109.8
7	77.1	108.8	24.9	83.9	93.9
Mean	73.4	108.1	29.1	79.0	95.7
SD	4.6	20.0	8.1	13.8	9.5
Maximum	80.4	138.1	37.4	101.8	109.8
Minimum	66.0	82.1	16.1	63.5	85.1

All values of EF, EDV, SV and LV mass for the patient SLE cohort fell within both the normal ranges of cardiac function provided by Siemens and those calculated using our local population.

7.12 Like for Like Comparison

The SLE cohort was then compared to specifically chosen age- and gender-matched cohort of seven NHV allowing their mean values of cardiac function to be compared. In addition to this, a student's t-test (assuming equal variances) was performed on the individual values obtained for each patient and volunteer to determine if significant differences in cardiac function existed between the SLE and NHV cohorts (Table 7.6).

Table 7.6 Age- and gender-matched values were compared using a paired t-test.

Parameter	SLE (n=7)	NHV (n=7)	p value
EF ± SD (%)	73.4 ± 4.6	70.7 ± 3.5	0.25
EDV ± SD (ml)	108.1 ± 20.0	108.2 ± 14.5	0.99
ESV ± SD (ml)	29.1 ± 8.1	31.5 ± 5.3	0.53
SV ± SD (ml)	79.0 ± 13.8	76.7 ± 14.6	0.77
LV Mass ± SD (g)	95.7 ± 9.5	87.8 ± 8.0	0.04

Comparing these age- and gender-matched cohorts revealed a significant increase in LV mass for the SLE cohort when compared to the NHV cohort ($p < 0.05$). Mean values of EF and SV were also mildly elevated for the SLE cohort in comparison the NHV cohort (2.7% and 2.3ml respectively, $p > 0.05$) whilst measures of EDV volume were almost identical. Measure of ESV were mildly reduced for the SLE cohort in comparison to the NHV cohort (2.4 ml, $p > 0.05$).

7.13 Conclusion

The second part of this study has highlighted a significant change in LV mass between age- and gender-matched cohorts of SLE patients and NHV at 3.0T. This is of particular interest as the individual mass values for the SLE cohort all fall within the normal ranges provided by both Siemens and our local population. Hence, these significant changes would remain undetected using normal post-processing procedures.

These findings suggest that age- and gender-matching patient groups to normal healthy volunteers may provide a more accurate assessment of cardiac function

and disease-related changes that potentially could assist early disease management and permit accurate tracking of disease progression over time.

7.14 Future work

This study was significantly limited by the size of the SLE cohort, which was out with the control of the department. Further investigations using larger patient groups are warranted to determine if this trend continues with larger patient numbers.

References

1. Natori S, Lai S, Finn JP, Gomes AS, Hundley WG et al. Cardiovascular function in Multi-Ethnic Study of Atherosclerosis: Normal Values by Age, Sex, and Ethnicity. *American Journal of Roentgenology* 2006; **186:** S357–S365.

2. Moon JCC, Lorenz CH, Frands JM, Smith GC, Pennell DJ. Breath-hold FLASH and FISP Cardiovascular MR Imaging: Left Ventricular Volume Differences and Reproducibility. *Radiology* 2002; **223:** 789–97.

3. Tseng W-YI, Liao T-Y, Wang J-L. Normal Systolic and Diastolic Functions of the Left Ventricle and Left Atrium by Cine Magnetic Resonance Imaging. *Journal of Cardiovascular Magnetic Resonance* 2002**; 4:** 443–57.

4. Koskenvuo JW, Karra H, Lehtinen J, Niemi P, Parkka J et al. Cardiac MRI: accuracy of simultaneous measurements of left and right ventricular parameters using three different sequences. *Clinical Physiology and Functional Imaging* 2007; **27:** 385–93.

5. Clay S, Alfakih K, Radjenovic A, Jones T, Ridgway JP, Sinvananthan MU. Normal ranges of human left ventricular volumes and mass using steady-state free precession MRI in the radial long axis orientation. *Magnetic Resonance Materials in Physics* 2006; **19:** 41–5.

6. Alfakih K, Plein S, Thiele H, Jones T, Ridgway JP, Sivananthan MU. Normal Human Left and Right Ventricular Dimensions for MRI as Assessed by Turbo Gradient Echo and Steady-State Free Precession Imaging Sequences. *Journal of Magnetic Resonance Imaging* 2003; **17:** 323–9.

7. Hudsmith LE, Petersen SE, Francis JM, Robson MD, Neubauer S. Normal left and right ventricular and left atrial dimensions using steady state free precession magnetic resonance imaging. *Journal of Cardiovascular Magnetic Resonance* 2005; **7:** 775–82.

8. Salton CJ, Chuang ML, O'Donnel CJ, Kupka MJ, Larson MG et al. Gender Diffrences and Normal Left Ventricular Anatomy in an Adult Population Free of Hypertension. *Journal of the American College of Cardiology* 2002; **39:** 1055–60.

9. Teo KSL, Carbone A, Piantadosi C, Chew DP, Hammett CJK et al. Cardiac MRI Assessment of Left and Right Ventricular Parameters in Healthy Australian Normal Volunteers. *Heart, Lung and Circulation* 2008; **17:** 313–17.

10. Olivetti G, Giordano G, Corradi D, Melissari M, Lagrasta C et al. Gender differences and aging: effects on the human heart. *Journal of the American College of Cardiology* 1995; **26:** 1068–79.

8. Left Atrial Dimensions as Determinants of Cardiac Dysfunction

Left atrial (LA) size and function are important prognostic factors for cardiovascular disease. An enlarged LA can be indicative of various pathologies, such as atrial fibrillation (AF) [1, 2], late gadolinium left-ventricular wall enhancement [3], cerebral ischemic events [4] and an increased risk of morbidity and mortality [5].

Many previous imaging investigations of the LA have involved the use of echocardiography techniques. Relatively simple assessments of LA dimensions have been derived by the measurement of length [6] or area [7], and these measures have previously been implemented to describe clinical associations of LA structure with AF and other cardiac disorders. These techniques can also be extended to derive an assessment of LA volume if the shape of the LA is roughly approximated to a sphere of volume $4/3\pi r^3$, where r is a single measure of the anterior-posterior (AP) radius [8]. Other model-based assumptions have also been reported, where the LA volume is calculated by area-length measures or by assumption of ellipsoid geometry [8–10]. Normalisation (to body surface area) of the resulting echo LA volumes enables 'cut-off' values to be derived, where individuals may be at an enhanced risk of cardiovascular adverse events if their LA volume is enlarged [11, 12].

Ultrasound echo has the obvious advantage of being relatively quick and cheap, but the aforementioned measurements of length, area and volume are generally based on assumptions of shape modeling and are susceptible to errors. The extent of this error is likely to be variable, but underestimated LA volumes of up to 37% relative to MRI have previously been reported [13]. The left atrium is known to be an asymmetric cavity and is therefore more accurately reflected by measurement of volume rather than area or linear dimension. Furthermore, LA dilation is unlikely to be evenly distributed in all planes, and measurement of the AP dimension is likely to be further insensitive to change for this reason [14].

MRI is recognised as the Gold Standard for atrial volumes, as the greater image resolution permits more accurate border detection of the left atrium as compared to 2D and 3D echo [15], and the accuracy of MRI measurement of left atrial volumes has also been validated against water displacement of cadaveric atrial casts [16]. The more recent use of CINE TrueFISP (SSFP) sequences are able to provide excellent depiction of the left atrium [17] and can be applied on either 1.5T or 3.0T machines [18]. However there are widespread variations in the different MRI methods used for quantitative LA volumetry, despite the clear suitability of the MRI technique.

A technical comparison of the MRI methods reported in the recent peer-reviewed literature is presented in Table 8.1 [17–31]. It is apparent that a 'standard' MRI method for LA evaluation is yet to be defined, with some preferring to acquire the data stack in the two-chamber (2ch) orientation [23] and others favoring the short axis view [24] or a standard transverse acquisition [25]. Other parameters such as the image slice thickness are also quite variable (reported slice thicknesses of 4–10mm). Finally, there has been little previous work reported on LA volume repeatability using MRI, and this is of obvious importance in the case of longitudinal studies where excellent repeatability is essential for consistency between 'baseline' and 'follow-up' examinations.

The objectives of this study were thus two-fold. Firstly the initial aim was to apply the chosen MRI LA volumetric technique on a cohort of healthy volunteers at two time points over the course of a single day (AM and PM) in order to establish baseline normal range data, along with 'single time-point' and 'scan-to-scan' intra- and inter-observer measurement repeatability. Following on from this, the second aim of the study was to utilise the same LA measurement technique in order to identify possible LA volume differences between healthy volunteers and groups of patients with carefully defined clinical cardiac conditions.

Table 8.1 Peer-reviewed image acquisition data, where Simpson's Rule has been used to define LA volume-based parameters.

Author/Year	Ref	Field	Pulse Seq	Slice/Gap	Matrix	FOV	View	LAA/PV	Cohort	LA Volume
		(T)	(gating)	(mm)		(cm)			(n)	Abs (ml) / Norm (ml/m^2)
Jarvinen/1996	19	1.0	GRE cine (P)	10/N	256	34	VLA	I/E	HV (8)	Abs 106±21
	19	1.0	GRE cine (P)	10/N	256	34	VLA	I/E	HCM (8)	Abs 142±44
	19	1.0	GRE cine (P)	10/N	256	34	VLA	I/E	DCM (8)	Abs 141±37
Poutanen/2000	20	1.5	FLASH (Y)	4-8/N	256	40	HLA	E/E	Juveniles (30)	Abs 26.7±7.4, Norm 22.1±5.3
Sievers/2004	17	1.5	TrueFISP (P)	7/3	N	N	SA	N	HV (15)	Abs 61.3±19
	17	1.5	TrueFISP (P)	7/3	N	N	SA	N	AF (18)	Abs 112.7±41.3
Hauser/2004	21	1.5	SSFP (P)	10/N	256	48	HLA	E/E	AF (18)	Abs 118±39
Raman/2005	22	1.5	SSFP/F-GRE	N/N	N	N	HLA	E/N	HV (15)	Norm 27±9
	22	1.5	SSFP/F-GRE	N/N	N	N	HLA	N	Paroxysmal AF (20)	Norm 31±8
	22	1.5	SSFP/F-GRE	N/N	N	N	HLA	N	HCCMD (12)	Norm 28±8
Therkelsen/2005	23	1.5	FLASH (Y)	6/0	256	35	VLA	N/E	HV (19)	Norm 49.7±6.0
	23	1.5	FLASH (Y)	6/0	N	35	VLA	N	Persistent AF (58)	Norm 78.5±18.5
	23	1.5	FLASH (Y)	6/0	N	35	VLA	N	Permanent AF (19)	Norm 77.4±19.1
Sievers/2005	24	1.5	SSFP (P)	6/4	256	38	SA	N	HV (18)	Abs 66.4±20.1
	24	1.5	SSFP (R)	6/4	192	38	SA	N	HV (18)	Abs 66.8±19.8
Germans/2007	25	1.5	SSFP (R)	5/5	N	N	VLA	I/E	HV (40)	Norm (O: 50±6.7, Y: 47±9.3)
Hudsmith/2007	18	Var	TrueFISP (R)	7/3	N	35	SA	I/E	HV (10)	Abs (1.5T:81±27, 3.0T 78±25)
	18	Var	FLASH (R)	7/3	N	35	SA	I/E	HV (10)	Abs (1.5T: 82±26, 3.0T: 77±26)
Marui 2008	26	1.5	FLASH (P)	8/2	N	N	Axial	N/N	AF (74)	Abs 361 +/- 74
Patel/2008	27	1.5	SSFP (R)	6/N	N	N	Axial	E/E	Patients (30)	Abs 107±36 range (51-188)
Nori 2009	28	1.5	TrueFISP (R)	6/0	256	400	HLA	N/N	Paroxysmal AF (16)	Norm (37.0+/-6.4)
	28	1.5	TrueFISP (R)	6/0	256	400	HLA	N/N	Permanent AF (13)	Norm (41.4+/-8/7)
	28	1.5	TrueFISP (R)	6/0	256	400	HLA	N/N	HV (12)	Norm (28.8+/-6.1)
Bastarrika/2010	29	1.5	SSFP (R)	5/0	192	32-38	Axial	I/E	HTP (29)	Abs 158.2 ± 72.5
Wen/2010	30	3.0	FIESTA (R)	5/N	224	35	VLA	E/E	Patients (49)	Norm 46.2±9.7
Sarikouch 2011	31	1.5	SSFP (Y)	5-6/N	168	N	Axial	I/E	HC & A (115)	Abs 64.7±26.1

Ref, reference as numbered in manuscript; T, Tesla; Var, variable field strength; GRE, gradient echo; FLASH, fast low-angle shot; TrueFISP, fast imaging with steady-state precession; SSFP, steady-state free precession; F-GRE, fast gradient echo; FIESTA, fast imaging employing steady-state acquisition; P, prospective gating; R, retrospective gating; Y, yes; N, data not provided; FOV, field of view; VLA, vertical long axis; HLA, horizontal long axis; SA, short axis; LAA, left atrial appendage; PV, pulmonary viens; I, included; E, excluded; HV, healthy volunteers; HCM, hypertrophic cardiomyopathy; DCM, dilated cardiomyopathy; HCCMD, heritable cardiac conduction and myocardial disease; HTP, heart transplant patient; HC & A, healthy children & adolescents; Abs, absolute value; Norm, normalised value; O, older group; Y, younger group.

8.1 Methods and Materials

The following three fully-informed and consenting study cohorts were recruited for MR imaging:

1. Fifteen healthy normal volunteers (HNV). Volunteers were selected if they were < 40 years of age, had no previous medical history of any cardiovascular problem and had no contraindication to MRI. The cohort comprised of eight males and seven females, age range 24–39 years (mean 31 years).

2. Fifteen patient volunteers with left ventricular hypertrophy and ischemic heart disease (LVHI). Inclusion criteria for the LVHI patients targeted those with known clinical history of ischemic heart disease or angina, together with the presence of left ventricular hypertrophy by M-Mode Echocardiography as defined by the American Society of Echocardiography ($115g/m^2$ for males, $95g/m^2$ for females), blood pressure <150/90 and no contraindication to MRI. The LVHI cohort comprised of 13 males and two females, age range 50–78 years (mean 64 years).

3. Fifteen patient volunteers with left ventricular hypertrophy and type II diabetes (LVHD). Inclusion criteria for the LVHD patients targeted those with clinical Type 2 diabetes, left ventricular hypertrophy (as defined above), blood pressure <150/90 and no contraindication to MRI. The LVHD cohort comprised of eight males and seven females, age range 45–81 years (mean 66 years).

The healthy volunteers were scanned at two time-points (AM and PM – each over the course of a single day) and patient volunteers were scanned once at a single time-point. MR imaging was performed on a 3T Magnetom Trio scanner (Siemens, Erlangen, Germany) using body array and spine matrix coils. A series of localizer TrueFISP images were initially obtained in the axial, coronal, sagittal, and 2-chamber (2ch), 4-chamber (4ch) and short-axis (SA) views. Subsequently, a set of 2D CINE segmented TrueFISP images were derived in the 2ch, 4ch and SA orientations from these initial localizers.

Using these 2ch, 4ch and SA images as new reference positions, a 2D ECG-gated segmented CINE TrueFISP sequence with retrospective gating was then implemented to acquire multi-slice '2ch' images from the lateral side of the left atrium to the atrial septum (perpendicular to the plane of the mitral valve; Figure 8.1). Two image slices were acquired per breath hold (5mm), with each breath hold (at end expiration) restricted to less than 15 sec. Other imaging parameters were TR/TE = 3.4/1.5ms, flip angle (FA) = 50°, parallel imaging (GRAPPA) factor of 3, and in-plane resolution of 173×256 over a targeted field of view of 360–420mm.
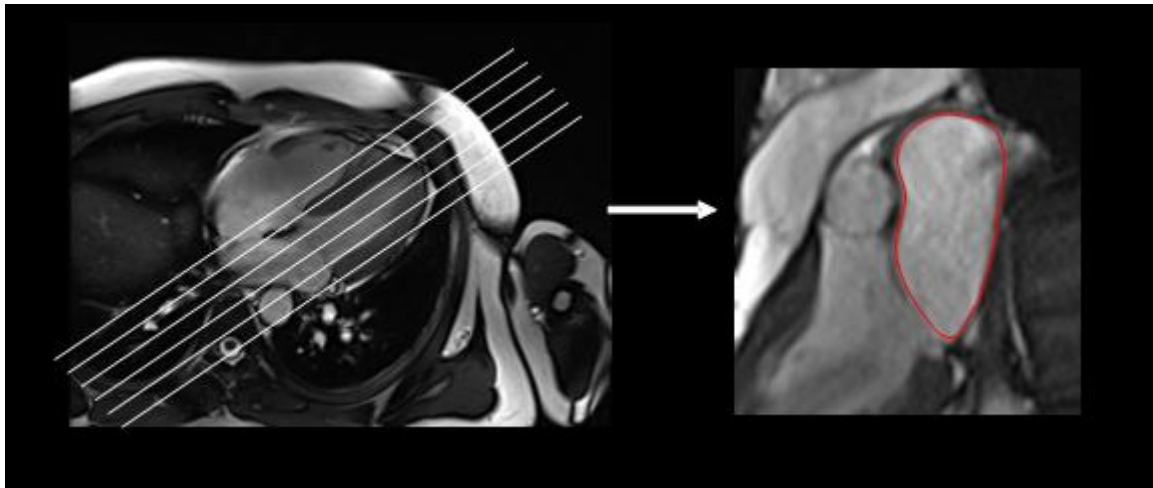
Figure 8.1 Image acquisition and segmentation of quantitative left atrial parameters.

Finally, a series of 2D CINE segmented TrueFISP images were also acquired as a short-axis stack across the entire left ventricle from the atrio-ventricular ring to the apex. The imaging parameters were TR 3.4ms, TE 1.5ms, and flip angle 50°. Two slices per breath hold were obtained, with a parallel imaging (GRAPPA) factor of two and slice thickness 6mm (4mm gap) for each patient. The in-plane resolution was 192 pixels, with a field-of-view range 340–450mm.

8.2 Image Analysis

Image segmentation of the entire atrial structure (see example in Figure 8.1) for all subjects was performed twice at atrial diastole and systole by an MRI Physicist observer with 8 years of cardiac MRI experience using commercial software ('Argus', Siemens Multi-Modality Work Platform, version VB15). Segmentation methods were carefully pre-defined in order to ensure that appropriate cardiac phases and slice ranges were analysed. Contours for all image slices across the left atrium were defined at diastole and systole by

measuring the blood volume contained by the atrial wall and the clearly delineated mitral valve (which formed the segmentation boundary with the left ventricle). The left atrial appendage was not included in the atrial volume measurements, and pulmonary vein structure was also excluded wherever possible. Repeated segmentations were completed over two time-points, with at least 1 month between each analysis to ensure that segmentation 'learning bias' was minimised. Additionally, a second MRI physicist observer with 5 years of cardiac MRI experience independently performed the segmentation process once for every subject in order to establish inter-observer variability. Left atrial ejection fraction (LA-EF), end-diastolic volume (LA-EDV), end-systolic volume (LA-ESV) and stroke volume (LA-SV) were all derived and indexed to body surface area, and test-retest intra- and inter-observer coefficients of repeatability were calculated for each parameter across all cohorts.

The segmentation process was also undertaken on the left ventricular (LV) short-axis data in order to derive measurements of left ventricular ejection fraction (LV-EF), end-diastolic volume (LV-EDV), end-systolic volume (LV-ESV), stroke volume (LV-SV) and LV mass. Left ventricular endocardial and epicardial borders were defined on all images corresponding to end-diastole (ED) and end-systole (ES) by the same MRI physicist observers in order to derive intra- and inter-observer variability. Again, segmentation rules describing the analysis of appropriate basal and apical slices, papillary muscles

and trabecular structures were pre-defined. Image slices were only considered if greater than 50% full-thickness myocardium was visible and papillary muscles were included within the LV mass if they were visibly indistinguishable from the endocardial wall.

Statistical testing for normality of all data was examined using the Shapiro-Wilks test (SPSS, IBM Corporation, Somers NY, USA) and subsequent analysis was performed using one way analysis of variance (ANOVA) with post-hoc analysis in order to test the null hypothesis that no structural or functional differences between any of the mean LA parameters were observable between any of the cohorts. Intra- and inter-observer repeatability of LA measurement techniques was examined by use of Bland-Altman statistics and described by the coefficient of repeatability (CoR). Correlations between left atrial volumes and the left ventricular parameters were also investigated.

8.3 Results

All MR data were acquired successfully except in the case of one healthy volunteer who was noted to have moved during the course of the PM LA acquisition. Consequently this dataset was removed from the LA AM-PM 'scan-to-scan' repeatability assessment, prior to the analysis phase.

Figure 8.1 above is mentioned previously as an example of an image identifying the left atrium in the chosen acquisition plane, together with contour

placement. Initial visual inspection of the LA in the patient populations revealed that the LA volumes in the LVHI cohort appeared enlarged relative to the other cohorts studied. An example is shown in Figure 8.2, where images at LA end-diastole and LA end-systole are illustrated for an LVHI example relative to a typical HNV example.
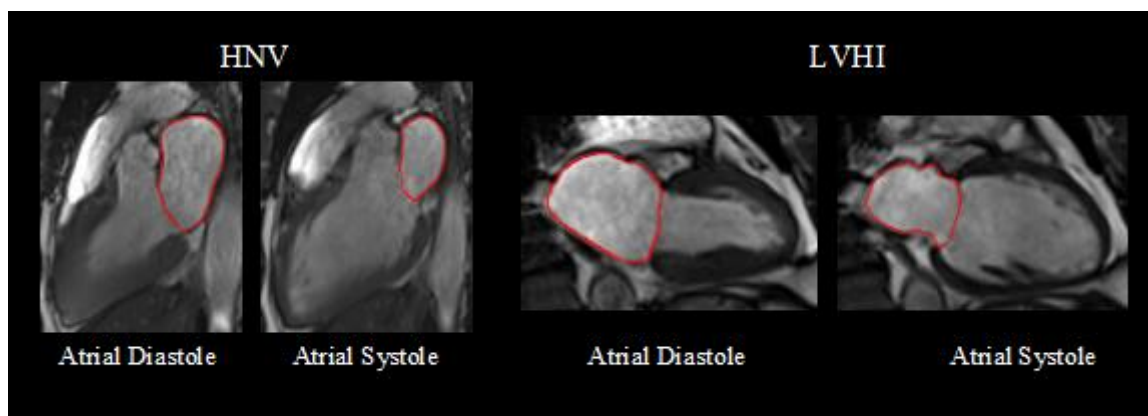
Figure 8.2 Example left atrial segmentation in (a) a healthy volunteer and (b) a patient volunteer with LVH and angina.

The mean quantitative LA parameters obtained are presented in Table 8.2, along with intra- and inter-observer coefficient of repeatability measurements (CoR). For volumetric data the CoRs ranged from 1.3 ml/m^2 to 3.9 ml/m^2, and for functional (LA-EF) data the CoRs ranged from 2.7% to 4.9%. The volume repeatability was typically 2–3 ml/m^2, although this was marginally elevated when AM-PM 'scan-to-scan' data were assessed, or when an inter-observer was used to perform one set of analyses.

Significant differences were identified between the LVHI cohort and the healthy volunteers (HNV) for mean LA-EDV (47.2 ml/m^2 v 39.0 ml/m^2 respectively,

p<0.05), LA-ESV (26.1 ml/m² v 17.9 ml/m² respectively, p < 0.05) and LA-EF

(44.3% v 54.5% respectively, p < 0.05).

Similar changes were also identified between the LVHI cohort and the LVHD

cohort for mean LA-ESV (26.1 ml/m² v 20.3 ml/m² respectively, p < 0.05) and

LA-EF (44.3% v 51.0% respectively, p < 0.05). The mean LA-EF was also found

to be slightly lower in the LVHD cohort relative to the healthy volunteers

(51.0% v 54.5% respectively, p<0.05), but otherwise there were no significant

differences measured between these two groups.

Aside from the differences noted above, the other striking observation was that

the mean LA-SV remained remarkably stable across all study groups (21.1 ± 3.9

ml/m² for HNV, 21.1 ± 6.1 ml/m² for LVHI, and 21.5 ± 7.3 ml/m² for LVHD),

suggesting that the blood volume delivery into the left ventricle remained

preserved – despite the clear structural differences identified.

Table 8.2 Left atrial volume data - for normal healthy volunteers (HNV – at AM and PM), patient volunteers with left ventricular hypertrophy and ischemia (LVHI) and patient volunteers with left ventricular hypertrophy and diabetes (LVHD). Data were acquired by two observers (1) and (2).

Left Atrial Volumetry/Function Parameters (Normalised to Body Surface Area)

Cohort	Observer	Scan	LAEF (%)	LAEDV (ml/m²)	LAESV (ml/m²)	LASV (ml/m²)
HNV	1	1 (AM)	54.3 ± 4.6	39.6 ± 7.5	18.2 ± 4.4	21.4 ± 3.9
	1	1 (AM)	54.5 ± 4.5	39.0 ± 7.1	17.9 ± 4.2	21.1 ± 3.7
	1	2 (PM)	54.7 ± 3.7	39.4 ± 6.8	17.9 ± 3.9	21.5 ± 3.6
	2	1 (AM)	54.5 ± 4.7	40.4 ± 7.4	18.4 ± 4.1	22.7 ± 3.6
LVHI	1	1 (AM)	44.6 ± 6.6	46.9 ± 9.2	25.8 ± 4.5	21.1 ± 6.1
	1	1 (AM)	44.3 ± 5.7	47.2 ± 9.7	26.1 ± 4.7	21.1 ± 6.0
	2	1 (AM)	43.5 ± 5.9	47.2 ± 9.2	26.4 ± 4.2	20.8 ± 6.1
LVHD	1	1 (AM)	51.0 ± 3.9	41.2 ± 14.0	20.2 ± 7.2	21.1 ± 7.3
	1	1 (AM)	51.0 ± 4.1	41.7 ± 13.8	20.3 ± 6.9	21.5 ± 7.5
	2	1 (AM)	49.7 ± 5.0	41.1 ± 14.0	20.5 ± 7.1	20.6 ± 7.6

Coefficient of Repeatability (CoR) Measurements

Cohort	Observer	Scan	LAEF	LAEDV	LAESV	LASV
HNV	Intra	1 (AM) v 1 (AM)	3.3	3.0	2.0	2.1
	Intra	1 (AM) v 2 (PM)	4.9	3.9	2.0	3.3
	Inter	1 (AM) v 1 (AM)	4.3	3.7	2.1	3.0
LVHI	Intra	1 (AM) v 1 (AM)	2.7	2.1	1.8	1.6
	Inter	1 (AM) v 1 (AM)	3.9	3.4	2.1	3.0
LVHD	Intra	1 (AM) v 1 (AM)	3.2	2.1	2.1	1.3
	Inter	1 (AM) v 1 (AM)	3.7	2.9	1.6	2.6

The corresponding mean left ventricular parameters are not described fully in this report because the main focus of the work was to examine the left atrium. However the relationship between mean left atrial size (LA-EDV and LA-ESV) and mean LVM was investigated for each of the cohorts studied, and these data are highlighted in Figure 8.3. The mean LVM values were found to be significantly raised in the LVHI cohort (72.2 g/m²) relative to the HNV cohort (59.5 g/m², $p < 0.05$) and the LVHD cohort (60.8 g/m², $p < 0.05$) , thus mimicking the same pattern of change as that observed for the mean LA-EDV and LA-ESV measurements.
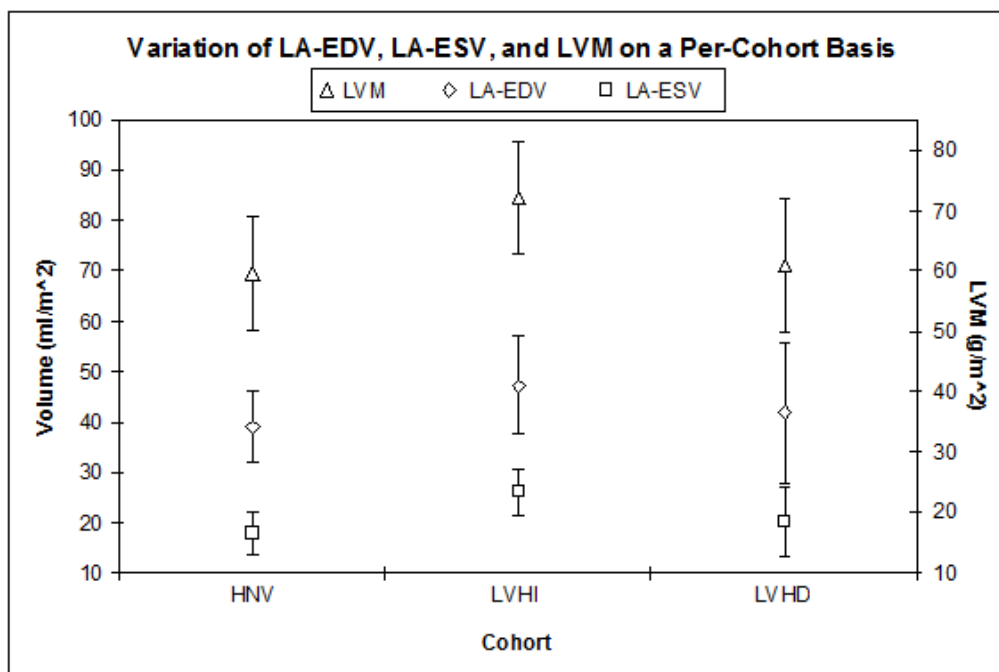
Figure 8.3 Relationship between mean LA-EDV, LA-ESV and LVM values for the three cohorts studied. Significant changes (increases) were noted in the LVHI cohort for mean LA-EDV, mean LA-ESV, and mean LVM relative to the HNV population.

When the relationship between the LA and the LV data were examined on an individual basis via use of the correlation coefficient, the best correlation was found between LA-ESV and LVM for the healthy volunteers (HNV); $R^2 = 0.71$. This correlation was notably reduced in both patient cohorts ($R^2 = 0.21$ for LVHI, and $R^2 = 0.28$ for LVHD). A similar pattern was evident when correlations between LA-EDV and LVM were investigated, with $R^2 = 0.58$ for HNV, $R^2 = 0.23$ for LVHI and $R^2 = 0.34$ for LVHD.

8.4 Discussion

This study has demonstrated that it is possible to use commercially available, carefully selected MRI sequence parameters to derive repeatable quantitative measures of human left atrial structure and function. Satisfactory repeatability can be achieved whether the data are derived by single or multiple observers from healthy volunteers (at single or multiple time-points) or from patients with cardiovascular disease. Further, clear differences in quantitative mean structural and functional left atrial volume parameters have been observed between healthy volunteers and patients with left ventricular hypertrophy and ischemia.

A notable finding of the initial literature review was the large array of methods by which the LA has previously been quantified using MRI, a summary of which is contained in Table 8.1.

We set out with the initial aim to concentrate on volumetric assessments, as simple calculations of length or area were considered less sensitive for possible future use in monitoring small changes over time. Attempts at conducting LA volumetry using MR have mostly been made using spoiled gradient echo (SPGR) or (more recently) SSFP acquisitions in the 2ch, 4ch, short-axis or straight axial plane by using Simpson's rule. In particular it has been quite common for short-axis data to be acquired as an 'extension' of a standard left ventricular assessment, although our initial experience was that this is difficult to quantify in regions around the mitral valve. We elected to use the 2ch orientation as recommended initially by Jarvinen et al [16], as the mitral valve plane separating the LA from the LV can be very clearly identified in this plane. Our choice to implement slice coverage every 5mm was generally successful – leading to the acquisition of clear LA boundaries with little problem from partial volume artefacts. However the limitation of this method is that it requires the volunteer/patient to remain extremely still in order to ensure that each image slice within the LA 'stack' corresponds to the correct intended anatomy. The complete LA acquisition itself took typically 5 minutes to acquire data sequentially from the lateral side of the LA to the atrial septal wall. The number of slices required to cover this volume was variable (dependent upon patient size) but was typically 10–14 slices. The segmentation process was generally straightforward, although we chose to exclude the LA appendage because this was deemed to be a potential source of repeatability error – again

an important consideration if the method is to be used for monitoring subtle longitudinal changes over time.

A number of difficulties were encountered with the study. The use of 3T imaging was chosen because of the potential to utilise the 'additional signal' to acquire data faster (i.e. to obtain more 'slices per breath hold') than possible at 1.5T. However the downside was that it was necessary to invest extra time to ensure successful patient-specific targeted shimming in order to minimise resonance-offset and flow-related artefacts that are known to be associated with the SSFP sequence at 3T. We did not use 1.5T for this work, although LA assessments have been reported by Hudsmith et al [18] previously, and are reported as valid at either field strength.

The mean LA-EDV volume indices (39.0–40.4 ml/m^2) for the HNV cohort in this work are very similar to those acquired by Macieira et al [32] who have reported a mean of 40 ml/m^2 across 120 healthy volunteers. This is encouraging, as it has provided inter-site consistency of the LA volume index for healthy volunteers in different UK populations. Our HNV cohort was far smaller (n=15), but we did extend the volume assessment to observe two distinct time-points (AM and PM) per individual, which resulted in no detectable change to the measured volumes – suggesting that the LA volume is stable over short-term investigations.

Other consistent findings worthy of comment in this work include the identification of significantly lower mean LA-EF in both patient cohorts relative to the healthy volunteers, together with very stable mean LA-SV. These observations are in keeping with similar reported findings elsewhere [19].

Measurement reproducibility was assessed by measuring intra- and inter-observer coefficients of repeatability. With relatively easy LA boundary detection resulting in typical volumetric CoRs of 2–3 ml/m^2, the measurements can be considered as stable – even when different scan (AM-PM) time-points or inter-observers are involved.

The time taken for completion of a typical LA segmentation in this work was about 15 minutes. We acknowledge that quicker methods are available, particularly those that have described the use of the biplane area-length method for deriving LA volume [17]. However the limitation with this method is that quicker methods often rely upon geometric assumptions, which may be valid for healthy volunteers but less so for cohorts with cardiovascular disease where atrial remodelling has taken place. We share the same opinion as Hudsmith et al [18], who recommend that traditional MR volumetry should be used for research studies where precise LA measures are required.

The LA differences (and similarities) noted between the healthy volunteers and the two clinical cohorts may be considered as interesting observations, although

clinical interpretation of these data should be approached with caution because the initial inclusion criteria for each cohort were different (e.g. age, gender, exact blood pressure matching etc.). An initial hypothesis favoured by some cardiologists is that LA remodelling may occur as an 'early stage process' (i.e. potentially prior to left ventricular change) as a result of local blood pressure changes associated with developing cardiovascular disease. We are unable to support this theory with our clinical 'snapshot data', as for the LVHI cohort in particular it is apparent that structural and function LA and LV changes are both present simultaneously (Figure 8.3). Nevertheless, the existence of clear LA volumetric differences relative to healthy volunteers (that also follow a similar pattern to LV changes) suggest that LA volumetry may provide important additional information to support the analysis of LV function in clinical cohorts with developing cardiovascular disease.

This study has several acknowledged limitations. In addition to the added time taken for removal of '3T flow artefacts' during the data acquisition, and the time taken for subsequent quantitative analysis, the number of volunteers and patients involved is such that the study only takes on the form of a pilot investigation. Accurate clinical interpretation of the data is difficult due to this fact, and also due to the fact that the clinical cohorts selected were known to have symptomatic change associated with the left ventricle. In future work it would be interesting to use the same protocol and analysis techniques on a

cohort of patients or volunteers with no clinical evidence of cardiovascular disease, but with possible high risk as a result of other physiological indicators such as blood test markers. This would have the potential to allow a clearer test of the hypothesis that LA remodelling occurs prior to LV structural change in individuals with developing early cardiovascular disease.

8.5 Conclusion

This pilot study has demonstrated that MRI-derived quantitative measurements of LA are reproducible and able to distinguish clear structural and functional differences between healthy individuals and patients with left ventricular hypertrophy. The acquisition protocol and analysis method shows promise for possible future identification of early cardiac remodelling in clinical cohorts with non-diagnosed but 'high risk' cardiovascular disease. These LA endpoints may also be useful for monitoring of cardiac structure and function in response to intervention.

References

1. Vaziri SM, Larson MG, Benjamin EJ, Levy D. Echocardiographic predictors of nonrheumatic atrial fibrillation. The Framingham heart study. *Circulation* 1994; **89:** 724–730.

2. Tsang TSM, Barnes ME, Bailey KR, Leibson CL, Montgomery SC et al. Left Atrial Volume: Important Risk Marker of Incident Atrial Fibrillation in 1655 Older Men and Women. *Mayo Clinic Proceedings* 2001; **76:** 467–475.

3. Papavassiliu T, Germans T, Flücher S, Doesch C, Suriyakamar A et al. CMR findings in patients with hypertrophic cardiomyopathy and atrial fibrillation. *Journal of Cardiovascular Magnetic Resonance* 2009; **11:** 34.

4. Benjamin EJ, Agostino RB, Belanger AJ, Wolf PA, Levy D. Left atrial size and risk of stroke and death. The Framingham heart study. *Circulation* 1995; **92:** 835–841.

5. Rossi A, Cicoira M, Zanolla L, Sandrini R, Golia G et al. Determinants and prognostic value of left atrial volume in patients with dilated cardiomyopathy. *Journal of the American College of Cardiology* 2002; **40:** 1425.

6. Henry WL, Morganroth J, Pearlman AS, Clark CE, Iscoitz SB, Epstein SE. Relation between echocardiographically determined left atrial size and fibrillation. *Circulation* 1976; **53:** 273–279.

7. Waggoner AD, Barzilai B, Miller JG, Perez JE. On-line assessment of left atrial area and function by echocardiographic automatic boundary detection. *Circulation* 1993; **88:** 1142–1149.

8. Lester SJ, Ryan EW, Schiller NB, Foster E. Best method in clinical practice and in research studies to determine left atrial size. *American Journal of Cardiology* 1999; **84:** 829–32.

9. Pritchett AM, Jacobsen SJ, Mahoney DW, Rodeheffer RJ, Bailey KR, Redfield MR et al. Left atrial volume as an index of left atrial size: a population-based study. *Journal of the American College of Cardiology* 2003; **41:** 1036–1043.

10. Ujino K, Barnes ME, Cha SS, Langins AP, Bailey KR et al. Two-dimensional echocardiographic methods for assessment of left atrial volume. *American Journal of Cardiology* 2006; **98:** 1185–1188.

11. Osranek M, Bursi F, Bailey KR, Grossardt BR, Brown RD et al. Left atrial volume predicts cardiovascular events in patients originally diagnosed with lone atrial fibrillation: three-decade follow up. *European Heart Journal* 2005; **26:** 2556–2561.

12. Lang RM, Bierig M, Devereux RB, Flachskampf FA, Foster E et al. Recommendations for chamber quantification: A report from the American Society of Echocardiography's Guidelines and Standards Committee and the Chamber Quantification Writing Group, developed in conjunction with the European Association of Echocardiography, a branch of the European Society of Cardiology. *Journal of the American Society of Echocardiography* 2005; **18:** 1440–1463.

13. Rodevand O, Bjornerheim R, Ljosland M, Maehle J, Smith HJ, Ihlen H. Left atrial volumes assessed by three- and two-dimensional echocardiography compared to MRI estimates. *International Journal of Cardiac Imaging* 1999; **15:** 397–410.

14. Tsang TS, Abhayaratna WP, Barnes ME, Miyasaka Y, Gersh BJ, Bailey KR et al. Prediction of cardiovascular outcomes with left atrial size: is volume superior to area or diameter? *American Journal of Cardiology* 2006; **47:** 1018–23.

15. Artang R, Migrino RQ, Harmann L, Bowers M, Woods TD: Left atrial volume measurement with automated border detection by 3-dimensional echocardiography: comparison with magnetic resonance imaging. *Cardiovascular Ultrasound* 2009; **7:** 16

16. Jarvinen VM, Kupari MM, Hekali PE, Poutanen VP. Right atrial MR imaging studies of cadaveric atrial casts and comparison with right and left atrial volumes and function in healthy subjects. *Radiology* 1994; **191:** 137–42.

17. Sievers B, Kirchberg S, Addo M, Bakan A, Brandts B, Trappe H-J. Assessment of left atrial volumes in sinus rhythm and atrial fibrillation using the biplane area-length method and cardiovascular magnetic resonance imaging with TrueFISP. *Journal of Cardiovascular Magnetic Resonance* 2004; **6:** 855–863.

18. Hudsmith LE, Cheng ASH, Tyler DJ, Shirodaria C, Lee J et al. Assessment of left atrial volumes at 1.5 Tesla and 3 Tesla using FLASH and SSFP cine imaging. *Journal of Cardiovascular Magnetic Resonance* 2007; **9:** 673–679.

19. Jarvinen VM, Kupari MM, Poutanen V-P, Hekali PE. Right and left atrial phasic volumetric function in mildly symptomatic dilated and hypertrophic cardiomyopathy: CINE MR imaging assessment. *Radiology* 1996; **198:** 487–495.

20. Poutanen T, Ikonen A, Vainio P, Jokinen E, Tikanoja T. Left atrial volume assessed by transthoracic three-dimensional echocardiography and magnetic resonance imaging: dynamic changes during the heart cycle in children. *Heart* 2000; **83:** 537–542.

21. Hauser TH, McClennen S, Katsimaglis G, Josephson ME, Manning WJ, Yeon SB. Assessment of left atrial volume by contrast enhanced magnetic resonance angiography. *Journal of Cardiovascular Magnetic Resonance* 2004; **6:** 491-497.

22. Raman SV, NG VY, Neff MA, Sayar S, Sparks EA et al. Volume cine CMR to quantify atrial structure and function in patients with atrial dysrhythmias. *Journal of Cardiovascular Magnetic Resonance* 2005; 7: 539–543.

23. Therleksen SK, Groenning BA, Svendsen JH, Jensen GB. Atrial and ventricular volume and function in persistent and permanent atrial fibrillation, a magnetic resonance imaging study. *Journal of Cardiovascular Magnetic Resonance* 2005; 7: 465–473.

24. Sievers B, Addo M, Kirchberg S, Bakan A, Puthenveettil BJ et al. How much are atrial volumes and ejection fractions assessed by cardiac magnetic resonance imaging influenced by the ECG gating method? *Journal of Cardiovascular Magnetic Resonance* 2005; 7: 587–593.

25. Germans T, Gotte MJW, Nijveldt R, Spreeuwenberg MD, Aernout MB et al. Effects on aging on left atrioventricular coupling and left ventricular filling assessed using cardiac magnetic resonance imaging in healthy subjects. *American Journal of Cardiology* 2007; 100: 122–127.

26. Marui A, Saji Y, Nishina T, Tadamura E, Kanao S et al. Impact of left atrial volume reduction concomitant with atrial fibrillation surgery on left atrial geometry and mechanical function. *Journal of Thoracic and Cardiovascular Surgery* 2008; **135:** 1297–1305.

27. Patel AR, Fatemi O, Norton PT, West JJ, Helms AS et al. Cardiac cycle dependent left atrial dynamics: implications for catheter ablation of atrial fibrillation. Heart Rhythm 2008; **5:** 787–793.

28. Nori D, Raff G, Gupta V. Cardiac magnetic resonance imaging assessment of regional and global left atrium function before and after catheter ablation for atrial fibrillation. *Journal of Interventional Cardiac Electrophysiology* 2009; **26:** 109–117.

29. Batistarrika G, Zudaire B, Ferreira M, Arraiza M, Saiz-Mendiguren R, Rabago G. Assessment of left atrial volumes and function in orthotopic heart transplant recipients by dual-source CT. *Investigative Radiology* 2010; **45:** 72–76.

30. Wen Z, Zhang Z, Yu W, Fan Z, Du J, Lv B. Assessing the left atrial phasic volume and function with dual-source CT: comparison with 3T MRI. *International Journal of Cardiovascular Imaging* 2010; **26:** 83–92.

31. Sarikouch S, Koerperich H, Boethig D, Peters B, Lotz J et al. Reference values for atrial size and function in children and young adults by cardiac MR: a study of the German competence network congenital heart defects. *Journal of Magnetic Resonance Imaging* 2011; **33:** 1028–1039.

32. Maciera AM, Cosin-Sales J, Roughton M, Prasad SK, Pennell DJ. Reference left atrial dimensions and volumes by steady state free precession cardiovascular magnetic resonance. *Journal of Cardiovascular Magnetic Resonance* 2010; **12:** 65.

9. The Impact of Contrast Agents on Quantitative Parameters in Cardiac MRI

9.1 Introduction

It is possible to obtain cardiac images of good diagnostic quality in high-field Cardiac MRI (CMRI) without the need for gadolinium-based contrast agents; however as previously discussed in this thesis, contrast agents are required during cardiac perfusion to aid the evaluation of different patterns of myocardial scarring seen in myocardial infarctions and cardiomyopathies [1]. Normally, the short-axis stack of images used to derive ventricular volumes and mass measurements is acquired before the administration of contrast agent. However, in studies where perfusion analysis is required, there is a temporal window of approximately 10 minutes available between 'first pass' and 'delayed enhancement' acquisitions. This could potentially provide the opportunity to obtain short-axis left ventrical (LV) datasets during this period, thus minimising the length of time that the patient is in the scanner.

Previous comparisons of spoiled-gradient echo and steady-state gradient echo sequences (e.g. FLASH and TrueFISP) for the assessment of LV function [2] have identified significant differences in the resulting LV variables on the basis of these different sequences and contrast mechanisms. More specific studies have also investigated the use of inversion recovery gradient-echo (IR-GRE) techniques for combined post-contrast perfusion and LV mass analysis in

children and patients (with and without previously documented myocardial infarcts) and these have been compared to pre-contrast steady state free precession (SSFP) methods [3, 4]. In this latter report, significant LV mass differences were identified between IR-GRE and SSFP for pre- and post-contrast LV mass assessment, with the SSFP sequence being validated as the more accurate measure of LV mass using ex-vivo methods.

To date, previous assessments of pre- and post-contrast LV parameters have been undertaken using different pulse sequences only. Hence, this provided the motivation to examine possible perfusion differences using a single pulse sequence (SSFP) to establish if differences between LV variables might exist on the basis of whether the SSFP data were collected before or after the delivery of a gadolinium contrast agent. This research study specifically addresses left ventricular analysis at 3T in order to determine what effect the administration of contrast agent has on the calculated measurement of ejection fraction (EF), end diastolic volume (EDV), end systolic volume (ES), stroke volume (SV) and LV mass. A correct understanding of any such differences is deemed important, as MRI-derived normal human left and right ventricular ranges are routinely defined from pre-contrast short-axis images [5]. Identifying and acknowledging such differences may also allow the most appropriate post-scan clinical management of patients with LV dysfunction.

9.2 Methods and Materials

Fifteen healthy volunteers, 8 females (average age 48 years, range 41–61 years), and 7 males (average age 59 years, range 48–71 years), with no previous history of atherosclerotic disease, primary muscle disease, statin therapy or serious illness were selected for imaging from a large database of individuals who were participating in a separate local MRI cardiovascular screening study known as TASCFORCE. Exclusion criteria included: age less than 40 years, known alcohol abuse, pregnancy, claustrophobia, and any other known contraindication to MRI. Approval for this study was obtained from the local ethics committee and volunteers provided written informed consent.

This study was completed over a 5 month period with the pre- and post-contrast stacks of short-axis images (slice thickness 6mm, inter-slice gap 4mm) for each volunteer being obtained during a single imaging session using a 3T Magnetom Trio MRI scanner (Siemens, Erlangen, Germany). Initially, pre-contrast images were acquired (during end-expiration breath hold) from the atrio-ventricular ring to the apex of the heart, using a two-dimensional retrospectively-gated segmented 25 CINE frame TrueFISP sequence with spine matrix and six element body array matrix radio frequency (RF) coils. One or two slices were imaged per breath hold, depending on the R-R interval of the volunteer. Imaging parameters included an in plane data acquisition matrix of 173 × 256 and a field of view ranging from 320 to 420mm, (depending on patient

size), TR 3.4ms, TE 1.5ms and flip angle 50°. Post-contrast images (using the same imaging parameters) were subsequently obtained after intravenous injection of 10ml of gadolinium-based contrast agent (Dotarem, Villepinte, France) via a power injector (Spectris Solaris EP, MedRad Inc., Indianola, USA) followed by a saline flush of 20ml. Contrast was administered at a consistent rate (1.5ml/s) for all volunteers. The elapsed time between the administration of contrast agent and the acquisition of the mid-slice at end-diastole in the post-contrast short-axis stack consistently fell between 4 and 5 minutes for each volunteer.

9.3 Image Analysis

Image analysis was performed on a remote Siemens multi-modality workstation using ARGUS software (version VB15). An MRI physicist with 4 years' experience of quantitative cardiac MRI analysis (segmenter 1) performed semi-automated placement of endocardial and epicardial myocardial borders, from base to apex, on all slices pertaining to end-diastole (Figure 1) and end-systole. Each contour was defined by manually placing a circular region of interest (ROI) over each myocardial border and then invoking an automated edge-detection algorithm to optimise the placement of these contours. Finally, manual adjustment of each epicardial and endocardial contour was undertaken where required – thus ensuring optimised precision and consistency of contour placement. Papillary muscles and trabeculae were included in the left

ventricular mass when they were indistinguishable from the endocardial border, but otherwise they were assigned to the blood pool volume. Care was taken to ensure that slice selection at end-diastole and end-systole was consistent between the pre- and post-contrast images of each volunteer selected for this study, and images were retrospectively reviewed to ensure that the inclusion or exclusion of papillary muscles was consistent between the pre- and post-contrast images of each volunteer.
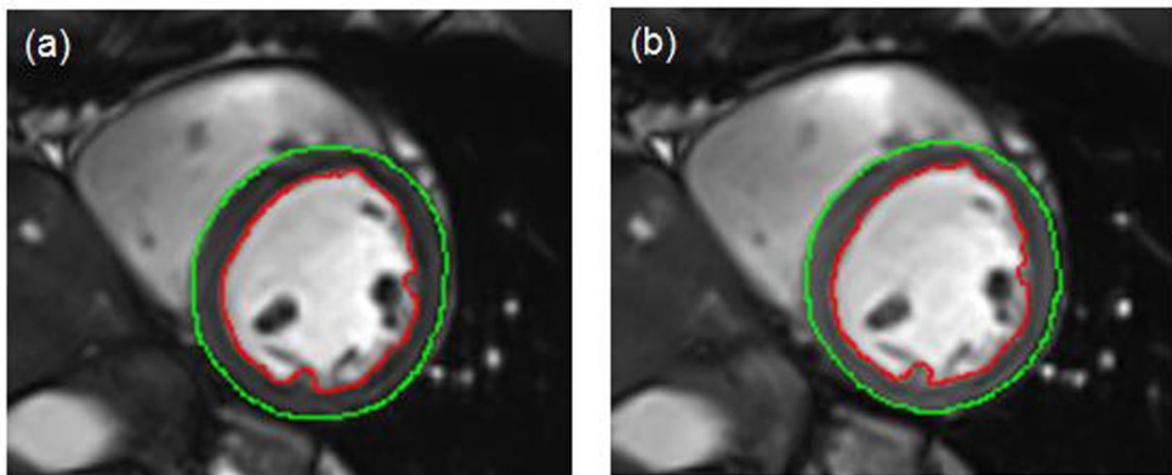
Figure 9.1 A comparison of pre- and post-contrast short-axis images (at end-diastole) of one volunteer showing (a) pre-contrast administration and (b) post-contrast administration.

Segmenter 1 repeated the analysis of ten randomly selected short-axis data-sets to establish intra-observer reproducibility. A second MR physicist segmenter with 6 years of cardiac MRI analysis experience (segmenter 2) repeated the analysis on seven data-sets from the study in order to establish inter-observer reproducibility. Segmenter knowledge/memory effects were minimised by

ensuring that no individual segmentations were repeated within a 1 month period.

9.4 Statistical Testing

Statistical testing for normality of data was undertaken using the Shapiro-Wilks test (SPSS, IBM Corporation, Somers, NY, USA), and subsequently the original and repeat values of each parameter were compared using a paired t-test (assuming equal variances) (Sigma Plot, version 10; Systat Software, Inc., San Jose, CA, USA). Results of the t-tests were deemed significant if $p < 0.05$.

9.5 Results

Initial inspection of the images showed subtle qualitative differences between the contrast of the myocardium, the blood pool and other surrounding tissues (Figure 1). Tables 9.1 & 9.2 contain the individual pre- and post-contrast measures of cardiac function calculated for each volunteer.

Table 9.1 The pre-contrast measures of cardiac function for each volunteer

	EF (%)	EDV (ml)	ESV (ml)	SV (ml)	LV Mass (g)
1	76.54	102.95	24.16	78.79	70.49
2	71.40	105.80	30.20	75.60	79.40
3	65.73	104.91	35.95	68.96	69.93
4	59.20	183.10	74.70	108.30	121.60
5	63.20	176.60	65.00	111.70	125.00
6	75.30	158.80	39.30	119.70	123.30

7	68.60	153.80	48.30	105.50	123.80
8	62.60	138.70	51.80	86.90	94.20
9	72.67	174.66	47.73	126.92	126.95
10	72.02	120.27	33.66	86.62	94.21
11	66.20	112.40	38.10	74.40	95.80
12	79.40	104.10	21.50	82.50	92.40
13	68.10	119.00	37.90	81.10	94.20
14	70.60	166.30	49.20	118.10	146.50
15	69.60	214.80	65.20	149.50	163.30

Table 9.2 The post-contrast measures of cardiac function for each volunteer

Post Contrast (n)	EF (%)	EDV (ml)	ESV (ml)	SV (ml)	LV Mass (g)
1	75.16	105.24	26.14	79.10	63.71
2	70.40	107.50	31.60	75.80	77.80
3	65.16	107.92	37.59	70.32	65.34
4	60.51	182.89	72.22	110.66	116.10
5	62.40	180.20	67.70	112.50	121.50
6	73.55	157.21	41.57	115.63	119.06
7	66.20	149.50	50.50	99.00	115.80
8	61.80	138.70	53.00	85.70	89.80
9	73.55	176.74	46.75	129.98	122.77
10	70.80	122.44	35.75	86.69	84.74
11	67.50	116.50	37.90	78.70	85.90
12	78.40	107.60	23.20	84.40	83.00
13	66.90	121.40	40.10	81.20	89.20
14	69.70	165.00	49.90	115.00	135.20
15	68.20	216.70	68.90	147.80	160.10

A significant reduction to the mean EF and LV mass parameters was noted following delivery of gadolinium contrast agent (Table 9.3). Additionally, a small but significant increase to the mean EDV and ESV parameters was also noted after contrast agent delivery. Individual values (i.e. on a per-volunteer basis) for LV mass were consistently lower for every volunteer following contrast agent, with reductions ranging from 1.6g to 11.3g (mean/median: -6.1g/-5.0g). The EF in 12 out of 15 volunteers was also reduced, with post-minus pre-contrast values of all volunteers ranging from -2.4% to 1.3%, (mean/median: -0.7%/-1.0%). In contrast, the majority (n = 10) of calculated EDV and calculated ESV (n = 12) parameters displayed a small but significant increase with the administration of contrast agent, post-minus pre-contrast values ranged from -4.3ml to 4.1ml (mean/median: 1.3ml/2.1ml) and -2.5ml to 3.7ml (mean/median: 1.3ml/1.7ml) respectively. Stroke volume was found to be particularly stable; no mean pre- versus post-contrast change of any significance was noted.

There was no correlation found between the age, sex, and body mass index of the volunteers and the extent of change between the calculated pre- and post-contrast values obtained for each cardiac parameter.

Table 9.3 Results of analysis performed on pre- and post-contrast datasets by segmenter 1.

Parameter	Pre-contrast	Post-contrast
EF ± SD (%)	69.4 ± 5.3	68.7 ± 5.0*
EDV ± SD (ml)	142.4 ± 34.5	143.7 ± 33.7*
ESV ± SD (ml)	44.2 ± 14.9	45.5 ± 14.6*
SV ± SD (ml)	98.3 ± 22.6	98.2 ± 21.9
LV mass ± SD (g)	108.1 ± 26.5	102.0 ± 26.6*

Mean values ± SD for all pre- and post-contrast cardiac parameters of ejection fraction (EF), end diastolic volume (EDV), end systolic volume (ES), stroke volume (SV) and left ventricular mass (LV mass). *denotes significant difference at $p < 0.05$ level.

9.5.1 Reproducibility

Segmenter 1 carried out repeat analysis on four pre-contrast and six post-contrast datasets in order to provide measurements of intra-observer reproducibility. Segmenter 2 performed repeat analysis on seven randomly selected pre-contrast datasets, previously analysed by segmenter 1, in order to determine inter-observer reproducibility. Full data for single time-point, test re-test, repeated measures for each parameter made by segmenter 1 and segmenter 2 are included in Table 9.4.

Table 9.4 Intra- and inter-observer reproducibility of pre- and post-contrast datasets.

Parameter	Intra-observer analysis (n=10)		Inter-observer analysis (n=7)	
	First analysis	Second analysis	Segmenter 1	Segmenter 2
EF $\pm$ SD (%)	70.0 $\pm$ 6.2	69.0 $\pm$ 5.4	71.9 $\pm$ 4.4	72.1 $\pm$ 4.8
EDV $\pm$ SD (ml)	141.6 $\pm$ 28.5	142.1 $\pm$ 28.0	126.7 $\pm$ 25.3	128.5 $\pm$ 27.6
ESV $\pm$ SD (ml)	44.3 $\pm$ 13.0	44.4 $\pm$ 12.2	35.7 $\pm$ 8.5	35.9 $\pm$ 9.7
SV $\pm$ SD (ml)	97.3 $\pm$ 19.8	97.8 $\pm$ 19.9	91.2 $\pm$ 19.4	92.6 $\pm$ 20.1
LV mass $\pm$ SD (g)	108.7 $\pm$ 19.7	108.4 $\pm$ 19.6	103.7 $\pm$ 23.0	105.0 $\pm$ 20.7

Segmenter 1 analysed 10 data sets twice whilst segmenter 2 performed repeat analysis on seven data sets previously analysed by segmenter 1. Data are presented for ejection fraction (EF), end diastolic volume (EDV), end systolic volume (ESV), stoke volume (SV) and left ventricular mass (LV mass) as mean $\pm$ SD. No significant differences between the means of any of the parameters were identified.

Bland Altman plots displaying the correlation in pre- and post-contrast measures of SV (Figure 2) and EF (Figure 3) highlight the stability between pre- and post-contrast stroke volume values and the downward trend in ejection fraction values. Bland Altman plots also highlight the variation between pre- and post-contrast LV mass variables (Figure 4), and also the correlation between intra-observer measurement 1 and measurement 2 (Figure 5) and inter-observer variation on measurement 1 (Figure 6). It can be seen that the spread of data in Figure 4 is greater than that in Figure 5, with the mean 'shift from zero' in Figure 4 highlighting the consistent post-contrast reduction in the LV mass values.
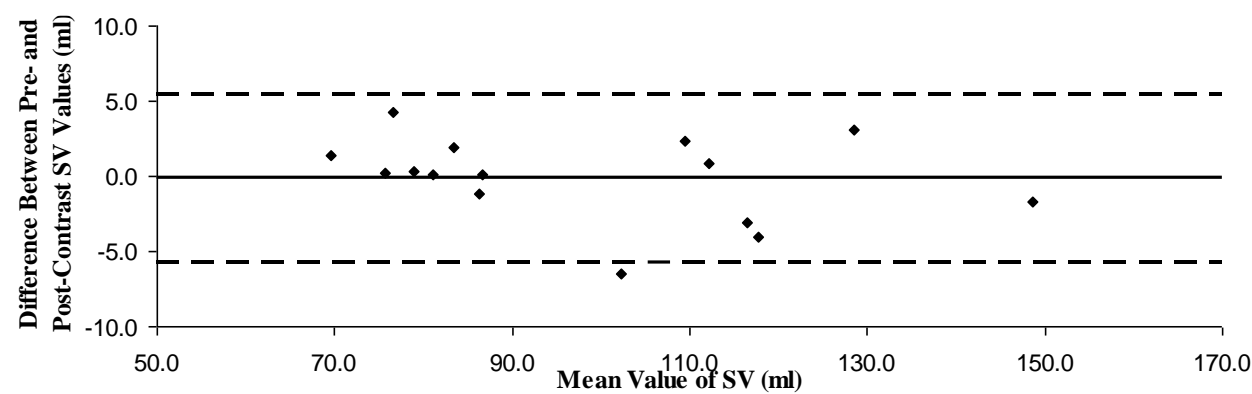
Figure 9.2 Correlation between pre- and post-contrast measures of SV values.
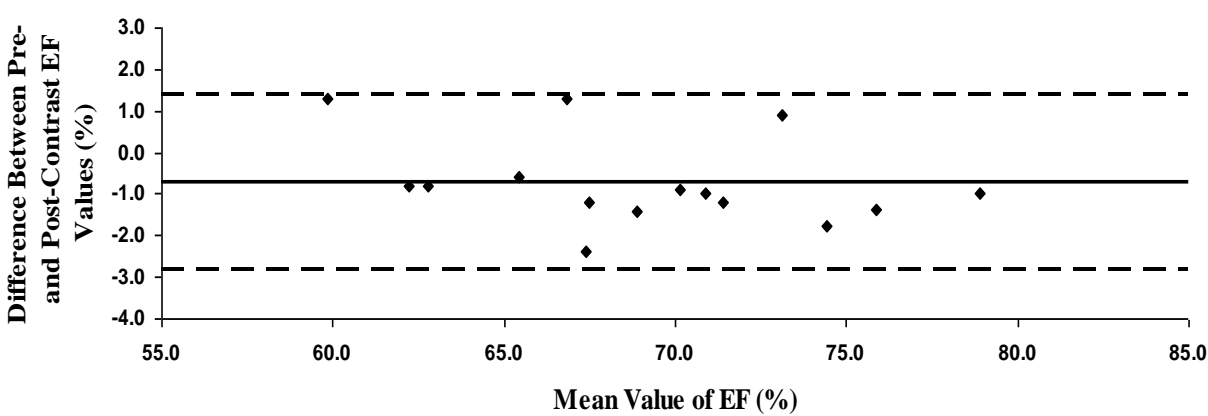
Figure 9.3 Correlation between pre- and post-contrast measures of EF.
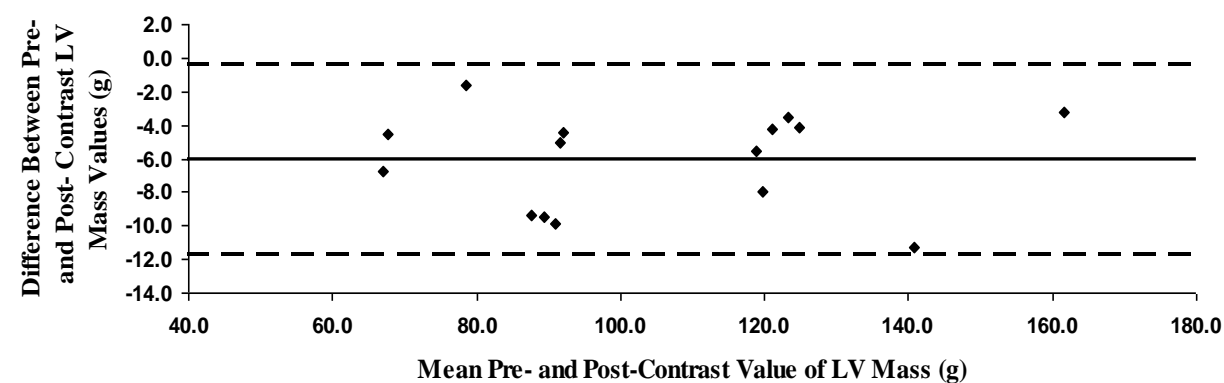
Figure 9.4 Correlation between pre- and post-contrast measures of LV mass.
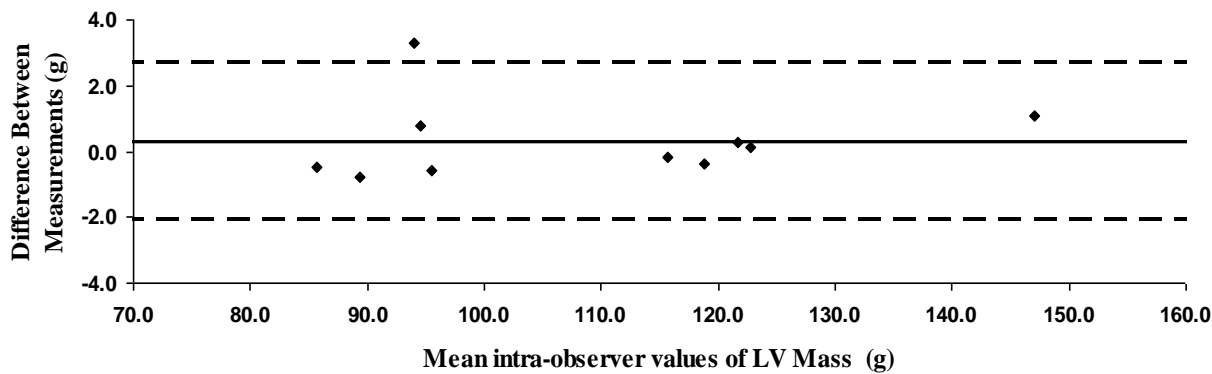
Figure 9.5 Intra-observer reproducibility of LV mass measurements.
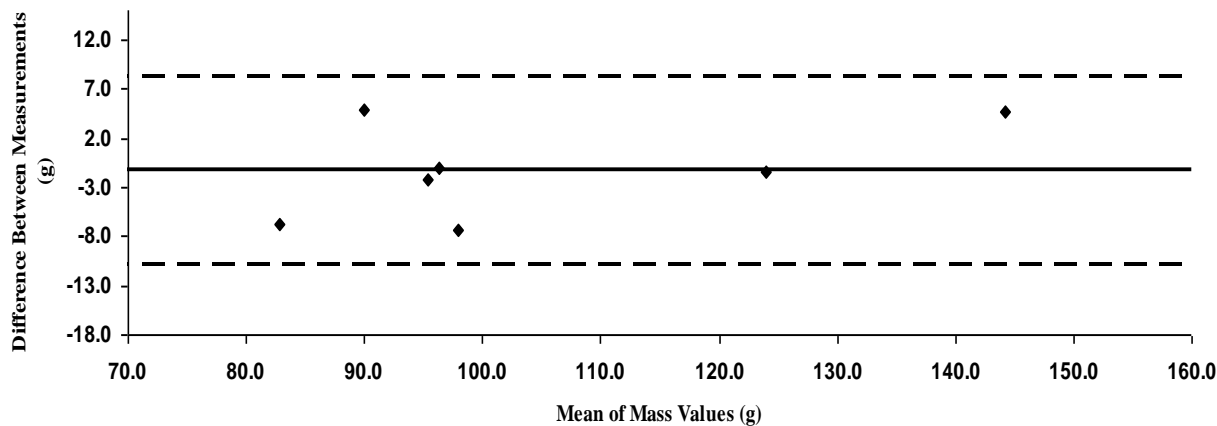
Figure 9.6 Inter-observer reproducibility of LV mass measurements.

9.6 Discussion

This study has demonstrated that significant changes to cardiac MRI values of EF, EDV, ESV and LV mass have been measured in this cohort of healthy volunteers, with the calculated values of EF and LV mass decreasing after contrast delivery, and EDV and ESV increasing after contrast delivery. The most significant of these changes was found between the pre-and post-contrast values of LV mass.

These data appear to be consistent with the hypothesis that the administration of contrast agent leads to a change in the visual detection of the endocardial and epicardial borders during image analysis. The presence of contrast agent in the left ventricle improves the high-contrast detection of the endocardial border, and this appears to result in an LV mass reduction together with increased blood pool volumes during segmentation. However we do acknowledge that this has not been independently measured and it is not possible to eliminate other possible covariate effects.

The relative differences between our pre-contrast and post-contrast LV mass measurements are very similar to those reported by Stephensen et al. [4]. This is reassuring from the point of view of study consistency, although our data suggest that LV mass differences arise from the presence of the contrast agent as opposed to the particular pulse sequence used.

The findings vary in their clinical significance. For example, if precise follow-up data are being assessed as part of a quantitative longitudinal study, then a 7g drop in LV mass is highly likely to be regarded as significant. However, if the data are being used for a quick single time-point quantitative assessment of a particular cardiac condition then these differences may be less important. We do acknowledge that the pre- and post-contrast differences between other parameters such as EF, EDV, etc. are far smaller, and as such we have reported these more from the perspective of an interesting and consistent observation.

Care was taken to eliminate systematic errors and maintain consistency in the acquisition and analysis of all datasets – resulting in minimal intra- and inter-observer variation. A single experienced segmenter carried out the analysis of all data sets for this study, as cardiac analysis (in particular LV mass) is known to be more reproducible for intra-observer assessments [6].

It is acknowledged that this study has some limitations. It is possible that a larger sample size might have resulted in the detection of more significant changes to each parameter, as the systematic differences reported in our work were rather small. It would also be advantageous to see whether the changes found could be replicated in patient groups. However, our sample size is consistent with other cardiac MRI studies of a similar nature [7, 8] and this was considered as part of the design phase of this work.

We acknowledge the fact that our 'standard dose' approach for contrast agent delivery is different from routine clinical practice in cardiac MRI perfusion where a weight-corrected dose would normally be delivered. The reason for this design compromise was due to the fact that this cardiac imaging was performed within the framework of a larger whole-body MRA investigation where a standard dose approach was required as part of this study design. Furthermore, from a clinical perspective the inclusion criteria for our subjects (see the Methods and Materials section) was such that a formal clinical assessment of cardiac perfusion involving weight-corrected dose was not deemed essential for this cohort.

9.7 Conclusion

In conclusion, this study has demonstrated that the administration of contrast agent in this cohort of healthy volunteers has significantly altered the calculated cardiac parameters of EF, EDV, ESV and particularly LV mass. Such changes should be considered correctly in the context of clinical decision-making in cardiac patients after CMRI perfusion examination when future therapy or intervention may be required. It is also recommended that image analysis is undertaken on either pre- or post-contrast datasets and that this choice is kept consistent for the case of repeat scans or longitudinal studies.

References

1. Knowles BR, Batchelor PG, Parish V, Ginks M, Plein S et al. Pharmacokinetic modeling of delayed gadolinium enhancement in the myocardium. *Magnetic Resonance in Medicine* 2008; **60:** 1524–30.

2. Alfakih K, Plein S, Thiele H, Jones T, Ridgway JP, Sivananthan MU. Normal human left and right ventricular dimesnsions for MRI as assessed by Turbo Gradient Echo and Steady-State Free Precession imaging sequences. *Journal of Magnetic Resonance Imaging* 2003; **17:** 323–9.

3. Grothues F, Boenigk H, Ghanem A, Schwerdtfeger A, Bartels D et al. Comparison of SSFP and IR-GRE techniques for measurement of total myocardial mass – influence of applied contrast dosage and implications for relative infarct size assessment. *Journal of Cardiovascular Magnetic Resonance* 2007; **9:** 607–14.

4. Stephensen SS, Carlsson M, Ugander M, Engblom H, Olivecrona G et al. Agreement of left ventricular mass in steady state free precession and delayed enhancement MR images: implications for quantification of fibrosis in congenital and ischemic heart disease. *BMC Medical Imaging* 2010; **10:** 4.

5. Lorenz CH, Walker ES, Morgan VL, Klein SS, Graham TP. Normal human right and left ventricular mass, systolic function, and gender differences by cine magnetic resonance imaging. *Journal of Cardiovascular Magnetic Resonance* 1999; **1:** 7–21.

6. Gandy SJ, Waugh SA, Nicholas RS, Simpson HJ, Milne W, Houston JG. Comparison of the reproducibility of quantitative cardiac left ventricular assessments in healthy volunteers using different MRI scanners: A multicentre simulation. *Journal of Magnetic Resonance Imaging* 2008; **28:** 359–65.

7. Grothues F, Smith GC, Moon JCC, Bellenger NG, Collins P et al. Comparison of inter-study reproducibility of cardiovascular magnetic resonance with two dimensional echocardiography in normal subjects and in patients with heart failure or left ventricular hypertrophy. *American Journal of Cardiology* 2002; **90:** 29–34.

8. Hudsmith LE, Petersen SE, Tyler DJ, Francis JM, Cheng ASH et al. Determination of cardiac volumes and mass with FLASH and SSFP CINE sequences at 1.5 versus 3.0Tesla: A validation study. *Journal of Magnetic Resonance Imaging* 2006; **24:** 312–18.

10. Conclusion

This first half of this thesis reports on many of the key developments that have transformed cardiac magnetic resonance imaging (CMRI) from a slow, artefact-prone technique that was difficult to master, into the clinically accepted gold standard modality for the assessment of cardiac function, mass and viability. Particular attention was given to the rapid increase in the magnitude of the main magnetic field, as high-field MRI provided the essential signal-to-noise (SNR) ratio essential for cardiac magnetic resonance imaging. The challenges and limitations associated with imaging at higher field strengths were also highlighted in a discussion on cardiac imaging at 3.0T in comparison to 1.5T.

The second half of this thesis actively contributes to the continuing development of CMRI by presenting a number of novel studies that demonstrate the accuracy and sensitivity of CMRI to highlight age- and disease-related changes in the human heart. The first of these studies was performed at 1.5T and effectively validates that ventricular analysis is accurate and reproducible, even for the novice segmenter. This study also establishes that in addition to LV changes, RV function can display a more significant change than LV function in different clinical conditions. These findings provide further information on the simultaneous function of both ventricles that may be of assistance in guiding appropriate clinical intervention.

(Oral Presentation 1 and 4; Poster Presentation 1 and 5).

The focus of the thesis then shifts to a newly installed 3.0T system. The initial aim of this work was to provide age- and gender-specific normal ranges of cardiac function for our local population. This study revealed that in addition to gender stratification, age stratification can provided a more accurate assessment of cardiac function.

A subsequent investigation at 3.0T established that the MRI-derived quantitative measurements of LA function are reproducible and able to distinguish clear structural and functional differences between healthy individuals and patients with left ventricular hypertrophy. This holds promise for possible future identification of early cardiac remodelling in clinical cohorts with non-diagnosed but 'high risk' cardiovascular disease. These LA endpoints may also be useful for monitoring of cardiac structure and function in response to intervention.

(Poster Presentation 4; Publication Submission 1)

Finally, research into the administration of contrast agent on the quantitative parameters of a cohort of healthy volunteers demonstrated that it significantly alters the calculated cardiac parameters of ejection fraction (EF), end-diastolic volume (EDV), end-systolic function (ESV) and particularly left ventricular

mass (LV mass). These changes should be considered correctly in the context of clinical decision-making in cardiac patients after CMRI perfusion examination when future therapy or intervention may be required. Further, they highlight that image analysis should be undertaken on either pre- or post-contrast datasets and that this choice be kept consistent for the case of repeat scans or longitudinal studies.

(Poster Presentation 2 and 3; Publication 1)

10.1 Future Developments

Cardiac magnetic resonance imaging is still an area of intensive research. For example, there is substantial interest in the evaluation of the coronary arteries, as the non-ionising, non-invasive nature of CMRI makes it ideally suited to assess disease progression over decades in 'at risk' populations. This has the potential to improve patient outcome as it would permit active disease management. However, the coronary arteries are tiny vessels and accurate imaging on this scale is presently limited by inadequate spatial and temporal resolution, even at 3.0T. However, ultra-high field 7T systems are being optimised in the research setting and ultimately promise to provide even greater speed and efficiency than today's 1.5T and 3.0T clinical scanners. The additional SNR available at this field strength can be used to improve and streamline structural and functional imaging and to potentially bring us one step closer to real-time, high resolution cardiac imaging. Real time imaging

would eliminate the need for cardiac gating, reduce breath-holds and permit faster patient throughput, making CMRI less challenging, more patient-friendly and more cost-effective.

Current research is also actively focused on novel contrast agents. These agents have targeting capabilities considered superior to conventional contrast agents as they have the potential is to provide atherosclerotic plaque characterisation to distinguish between fatty plaque (which is more likely to rupture) and calcified, fibrous plaque (which tends to be more stable).

We have established that CMRI can accurately detect subtle disease-related changes in the human heart. If we can also achieve the goals discussed in future developments, then CMRI would have the unique ability to offer a non-invasive, non-ionising full cardiac assessment of morphology, function, viability and coronary artery patency (with plaque characterisation) within a single imaging session. This would ultimately set CMRI above all other cardiac imaging modalities, including CT angiography.

10.2 Present and Future Work

The experience gained during this research has provided a sound platform for current work. This includes a study that complements the research detailed in chapter 9 of this thesis by providing a semi-quantitative assessment of the first pass of contrast agent as it passes through the cardiac chambers and myocardium of 67 clinical patients, imaged at 1.5T. This work will highlight the impact of cardiac disease on the transit time of contrast agent (Dotarem, Guerbet, Paris, France) and the 'time to peak' and peak signal intensity in the myocardium during first pass.

Delayed enhancement imaging was also performed on all 67 volunteers. These images will be used to assess myocardial viability [myocardium that still has the ability to contract (viable) versus myocardium that is replaced by fibrosis or scar tissue (non-viable)]. Delayed enhancement images are acquired between 10 and 15 minutes after the administration of the contrast agent. This time delay is an essential requirement as it allows the contrast agent to exit the blood vessels and diffuse freely through the extravascular, extracellular space. As gadolinium is hydrophilic, it cannot pass through the intact membranes of healthy myocytes. However, in areas of scarring and fibrosis, the membrane integrity is often compromised allowing the contrast agent to enter the cell, where is becomes trapped for a short period of time. Hence, by nulling the signal from

normal myocardium, areas of scarring and fibrosis will appear hyper-enhanced on delayed enhancement images.

The final part of this project aims to investigate the correlation between initial myocardial enhancement during first pass and any areas of focal hyper-enhancement in the delayed enhancement images of our patient groups.

(Conflict of interest: This study is funded by Guerbet.)

The research detailed in Chapter 6 of this thesis demonstrated that CMRI can accurately define disease related changes in the right ventricle of the human heart. Following on from this research, a CMRI pilot study is underway to test the hypothesis that a widely available and economical licenced drug can reduce inflammation in the pulmonary vessels of a distinct patient cohort and ultimately, reverse right ventricular hypertrophy commonly found in such patients.

10.2.1 Novel Work

In addition to the studies discussed above, a novel, multi-centre research study is underway that aims to quantify the phosphocreatine (PCr) and adenosine triphosphate (ATP) ratios of certain patient groups, as this will provide important information on myocardial energetics. Patient groups, such as renal patients, are known to have particularly low PCr/ATP ratios and hence, poorer outcomes. Providing an accurate, non-invasive, non-ionising way of measuring

cardiac energetics will allow the impact of pharmaceutical intervention or enhanced treatment plans to be assessed over prolonged periods of time.

10.2.2 Present Challenges

Phosphorus imaging is a relatively new technique with many challenges. Presently, Siemens do not manufacture phosphorus array coils, and therefore these coils have to be purchased from an independent manufacturer. The current multi-centre- study, in collaboration with Siemens Medical Solutions and RAPID Biomedical, has highlighted an incompatibility between the RAPID phosphorus coils and the Siemens MRI systems resulting from a hardware restriction on power and a software restriction on pulse duration. Collaborative work is underway to resolve this issue.

10.3 Presentations, Posters and Publications

10.3.1 Oral Presentations

1. European Society for Magnetic Resonance in Medicine and Biology (ESMRMB). Assessment of Clinical Differences at 1.5T between Quantitative Right and Left Ventricular Volumes and Ejection Fractions Using MRI: Valencia 2008.

2. Medical Physics Journal Club, Ninewells Hospital. Cardiac magnetic Resonance Imaging: Dundee 2010.

3. Scottish Universities and Stanford University Collaboration (SU²P). The Challenges of Cardiac Magnetic Resonance Imaging. Glasgow, February 2012.

4. Scottish Imaging Network (SINAPSE) Annual scientific meeting, Assessment of Clinical Differences at 1.5T between Quantitative Right and Left Ventricular Volumes and Ejection Fractions Using MRI: Glasgow May 2012.

5. Image Analysis in Life Science. The Effectiveness and Limitations of CMRI Analysis Techniques: Dundee August 2012.

10.3.2 Posters

1. ESMRMB. Assessment of Clinical Differences at 1.5T between Quantitative Right and Left Ventricular Volumes and Ejection Fractions Using MRI: Valencia 2008.

2. International Society for Magnetic Resonance (ISMRM) Quantitative Analysis of Cardiac Left Ventricular Variables Obtained by Magnetic Resonance Imaging at 3Tesla: A Pre- and Post-Contrast Comparison. Honolulu 2010.

3. SINAPSE. Quantitative Analysis of Cardiac Left Ventricular Variables Obtained by Magnetic Resonance Imaging at 3Tesla: A Pre- and Post-Contrast Comparison. Edinburgh 2010.

4. SINAPSE. Measurement of Cardiac Left Atrial Volumes in Healthy Volunteers and Patients with Left Ventricular Hypertrophy and Angina using MRI. Edinburgh 2010.

5. University of St Andrews, Postgraduate Day. Cardiac Magnetic Resonance Imaging. Department of Physics and Astronomy 2010.

6. Scottish Society for Experimental Medicine (SSEM). Assessment of Clinical Differences at 1.5T between Quantitative Right and Left Ventricular Volumes and Ejection Fractions Using MRI. Dundee May 2012.

10.3.3 Publications

1. *British Journal of Radiology* (BJR). Quantitative Analysis of Cardiac Left Ventricular Variables Obtained by Magnetic Resonance Imaging at 3Tesla: A Pre- and Post-Contrast Comparison. July 2012

[1,2S]Matthew, BSc, Hons, [2,3]S J Gandy, PhD, [2,3]R S Nicholas, PhD, [2]S A Waugh, MSc, [3]E A Crowe, DCR(D), [2]R A Lerski, PhD, [1]M H Dunn, PhD and [4]J G Houston, MD, FRCR

[1]Department of Physics and Astronomy, University of St Andrews, St Andrews, UK
[2]Department of Medical Physics, NHS Tayside, Ninewells Hospital and Medical School, Dundee, UK
[3]Department of Clinical Radiology, NHS Tayside, Ninewells Hospital and Medical School, Dundee, UK, and [4]Clinical Imaging, University of Dundee, Dundee, UK

10.3.4 Submissions – Under peer review:

1. Quantitative MRI Measures of Left Atrial Dimensions as Determinants of Cardiac Dysfunction – Technical Evaluation and Validation in Cardiac Patients and Healthy Volunteers

Stephen J Gandy[1,2], Shona Matthew[3], Sushma Rekhraj[4], Benjamin Szwejkowski[4], Patricia Martin[2], Allan D Struthers[4], J Graeme Houston[4]

[1]NHS Tayside Medical Physics, Ninewells Hospital, Dundee, DD1 9SY, UK.
[2]NHS Tayside Clinical Radiology, Ninewells Hospital, Dundee DD1 9SY, UK
[3]Department of Physics and Astronomy, University of St Andrews, The North Haugh, St Andrews, Fife KY16 9SS, UK
[4]Division of Medical Sciences, University of Dundee, Ninewells Hospital Dundee DD19SY, UK

10.3.5 Prizes

Poster Prize (2nd Place), 3rd Year Post Graduate Assessments, University of

St Andrews 2010.

Appendix A. Quality Assurance Testing: T1, T2 and Flip Angle

A1 The Bloch equations

The Bloch equations discussed in this thesis are modified below to provide explicit forms of the longitudinal and transverse magnetisation vectors (M_z, M_x and M_y) [Eqs. 21, 22 and 25 respectively].

$$\frac{dM_x(t)}{dt} = \gamma(B_0 M_y(t) + B_1 \sin(\omega t) M_z(t)) - \frac{M_x(t)}{T_2} \tag{1}$$

$$\frac{dM_y(t)}{dt} = \gamma(B_1 \cos(\omega t) M_z(t) - B_0 M_x(t)) - \frac{M_y(t)}{T_2} \tag{2}$$

and

$$\frac{dM_z(t)}{dt} = \gamma(B_1 \sin(\omega t) M_x(t) - B_1 \cos(\omega t) M_y(t)) - \frac{M_z(t) - M_0}{T1} \tag{3}$$

Immediately after the application of the RF pulse, $B_1 = 0$. This allows us to simplify our system of equations to

$$\frac{dM_x(t)}{dt} = \gamma B_0 M_y(t) - \frac{M_x(t)}{T2} \tag{4}$$

$$\frac{dM_y(t)}{dt} = \gamma B_0 M_x(t) - \frac{M_y(t)}{T2} \tag{5}$$

and

$$\frac{dM_z(t)}{dt} = \frac{M_z(t) - M_0}{T1} \tag{6}$$

M_x and M_y components

We derive the general solution for $M_x(t)$ and $M_y(t)$ and solve for $t = 0$. For brevity the full derivation is shown for $M_x(t)$. The y component follows similarly.

Solving for Eq. (4)

$$\frac{d^2 M_x(t)}{dt^2} = \gamma B_0 \frac{dM_y(t)}{dt} - \frac{1}{T}\frac{dM_x(t)}{dt} \tag{7}$$

Substituting Eq.(5) into the RHS of Eq.(7)

$$\frac{d^2 M_x(t)}{dt} = \gamma B_0 \left[\gamma B_0 M_x(t) + \frac{M_y(t)}{T2} \right] - \frac{1}{T}\frac{dM_x(t)}{dt} \tag{8}$$

and rearranging gives

$$\frac{d^2 M_x(t)}{dt^2} + \frac{1}{T2}\frac{dM_x(t)}{dt} + \gamma^2 B_0^2 M_x(t) = -\frac{B_0 \gamma M_x(t)}{T2} \tag{9}$$

Now substituting Eq.(4) into RHD of Eq.(9) yields

$$\frac{d^2 M_x(t)}{dt^2} + \frac{1}{T2}\frac{dM_x(t)}{dt} + \gamma^2 B_0^2 M_x(t) = \frac{1}{T2}\left(\frac{dM_x(t)}{dt} + \frac{M_x(t)}{T2} \right) \tag{10}$$

which reduces to

$$\frac{d^2 M_x(t)}{dt^2} + \frac{2}{T2}\frac{dM_x(t)}{dt} + \left(\omega_0 + \frac{1}{T2^2} \right) M_x(t) = 0 \tag{11}$$

where $\omega_0 = \gamma B_0$. Note that is the the form of a damped simple harmonic oscillator (SHO). The solution of the damped SHO is well known and so our general solution has the form

$$M_x(t) = \left(Ae^{i\omega_0 t} + Be^{-i\omega_0 t} \right) e^{-t/T2} \tag{12}$$

and M_y component is also given by

$$M_y(t) = \left(A'e^{i\omega_0 t} + B'e^{-i\omega_0 t} \right) e^{-t/T2} \tag{13}$$

where A, B, A$'$, and B$'$ are constants. The constants are found by imposing a boundary condition on our general solution. Here we find the solution at $t = 0$, then Eq.(12) reduces to

$$M_x(0) = A + B \tag{14}$$

We require another expression to solve for A and B and this is provided through the first derivative of M_x at $t = 0$

$$\frac{dM_x(0)}{dt} = i\omega_0 (A - B) - \frac{1}{T2}(A + B) \tag{15}$$

Equating with Eq.(4) at $t = 0$

$$i\omega_0 (A - B) - \frac{1}{T2}(A + B) = \gamma B_0 M_y(0) - \frac{M_x(0)}{T2} \tag{16}$$

Now we can solve for A by noting that Eq.(14) gives $B = M_x(0) - A$. Then Eq.(16) becomes

$$i\omega_0 (2A - M_x(0)) - \frac{M_x(0)}{T2} = \gamma B_0 M_y(0) - \frac{M_x(0)}{T2} \tag{17}$$

Rearranging, we find the A coefficient

$$A = \frac{1}{2}(M_x(0) - iM_y(0)) \tag{18}$$

then substituting our expression for A into Eq. (14) we find

$$B = \frac{1}{2}(M_x(0) + iM_y(0)) \tag{19}$$

Having found the A and B coeffiecients we can write the general solution as

$$M_x(t) = \frac{1}{2}(M_x(0)e^{i\omega_0 t} - iM_y(0)e^{-i\omega_0 t}) + \frac{1}{2}(M_x(0)e^{i\omega_0 t} + iM_y(0)e^{-i\omega_0 t})e^{-t/T2} \tag{20}$$

Grouping together term of $M_x(0)$ and $M_y(0)$, we can write (20) in its final form

$$M_x(t) = (M_x(0)\cos(\omega_0 t) + M_y(0)\sin(\omega_0 t))e^{-t/T2} \tag{21}$$

We find A' and B' in a similar manner. hence it follows that $M_y(t)$ is given by

$$M_y(t) = (M_y(0)\cos(\omega_0 t) - M_x(0)\sin(\omega_0 t))e^{-t/T2} \tag{22}$$

$M_z(t)$ component

Now we turn to the $M_z(t)$ term which is found through direct integration of Eq.(6).

$$\int_{M_z(0)}^{M_z(t)} \frac{dM_z(t)}{M_z}(t) - M_0 = \int_{t=0}^{t=t} \frac{-dt}{T1} \qquad (23)$$

Interating yields

$$\left[\ln(M_z(t) - M_0\right]_{M_z(0)}^{M_z(t)} = \left[\frac{-t}{T1}\right]_{t=0}^{t-t} \qquad (24)$$

Finally solving for $M_z(t)$ we find

$$M_z(t) = M_z(0)e^{-t/T1} + M_0(1 - e^{-t/T1}) \qquad (25)$$

A1.1 FLASH and TrueFISP

FLASH is a steady-state incoherent imaging technique as all the transverse magnetisation is essentially zero before the application of the next excitation pulse. The following analysis provides a valid solution to the steady-state longitudinal magnetisation for a given T1, T2, TR and flip angle and where there are no T2* effects (Eq 33) and for an isochromat of spins where M_0 is replaced by the voxel spin density and T2* replaces T2 (Eq 34) [1].

$$M_{\perp}(t_n) = M_{\perp}(0^+)e^{-t_n/T_2} \quad 0 < t_n < TR \tag{26}$$

Where $M_{\perp}(0^+)$ represents $M_{\perp}$ when $t_n = 0^+$

The total time from the first excitation pulse is t, and the relative time within each cycle is defined as

$$t_n \equiv t - nTR$$

The regrowth of M_z during this period is

$$M_z(t_n) = M_0(1 - e^{-t_n/T_1}) + M_z(0^-)e^{-t_n/T_1} \tag{27}$$

Where $M_z(t_n)$ represents M_z when $(t_n = 0^-)$

By inroducing the total time, equations (26) and (27) can be rewritten as

$$M_{\perp}((n+1)TR^-) = M_{\perp}(nTR^+)E_2 = M_z(nTR^-)\sin\theta E_2 \tag{28}$$

Equation (28) goes to zero as E_2 goes to zero. Under these circumstances

$$M_z((n+1)TR^-) = M_z(nTR^-)\cos\theta E_1 + M_0(1 - E_1) \tag{29}$$

Where $E_1 \equiv e^{-TR/T_1}$ and $E_2 \equiv e^{-TR/T_2}$

To acheive a steady-state by the Nth excitation pulse, M_z must be of equal value prior to each subsequent excitation pulse

$$M_z(mTR^-) = M_{ze} \quad m \geq N \tag{30}$$

From equations (29) and (30), M_{ze} must satisfy

$$M_{ze} = M_{ze}E_1 \cos\theta + M_0(1-E_1) \tag{31}$$

This provides the steady-state or equilibrium value

$$M_{ze} = \frac{M_0(1-E_1)}{(1-E_1 \cos\theta)} \tag{32}$$

Inserting these results into equation (26) gives

$$M_\perp(\theta, t_n) = M_{ze} \sin\theta e^{-t_n/T_2} = \frac{M_0 \sin\theta(1-E_1)}{(1-E_1 \cos\theta)} e^{-t_n/T_2} \quad 0 < t_n < TR \tag{33}$$

Considering a voxel containing several isochromats, equation (33) becomes

$$\rho_0(\theta, TE) = \rho_0 \sin\theta \frac{(1-E_1)}{(1-E_1 \cos\theta)} e^{-TE/T_2^*} \tag{34}$$

Where ρ_0 is the spin density of the voxel.

TrueFISP is a coherent imaging technique as the residual transverse magnetisation is 'recycled'. The magnetisation from TrueFISP [2] is given here without proof as:

$$S = \frac{K.M_0 \sin\alpha}{\left(T_1/T_2\right)(1-\cos\alpha)+(1+\cos\alpha)} e^{-TE/T_2} \tag{35}$$

Where K is a scaling factor (a.u.).

A2 Quality Assurance Checks on Contrast Measurements in MRI

During the installation of the 1.5T Avanto and the 3.0T Trio, a number of acceptance and quality assurance tests were routinely performed to ensure that both systems met the manufacturer's specifications and that the images produced by them were of a sufficient quality to provide relevant diagnostic information. During these tests, a set procedure was adhered to so that the results obtained could be used for comparative purposes in future quality assurance (QA) testing.

A2.1 Signal Intensity Measurements

Signal intensity measurements in MRI provide a sound understanding of the effects of field strength, flip angle (FA), repetition time (TR) and echo time (TE) on inherent T1 and T2 relaxation parameters of different tissues and are therefore, fundamental to understanding image optimisation in MRI. Hence, it is an essential requirement for any MRI novice to perform these measurements at 1.5T and 3.0T using FLASH and TrueFISP pulse sequences (chapter 5). As part of this research, signal intensity measurements were performed on the 3.0T Trio as part of its installation process, and on the 1.5T Avanto as part its regular quality assurance testing.

A2.2 The Images

Thorough signal intensity measurements require the acquisition of a very large volume of images as the T1 and T2 relaxation rates need to be calculated

over a range of TRs (TR = 100–500 in steps of 50; TR = 500–1000 in steps of 100; and TR = 1500, 2000, 3000, 5000, 10000) and TEs (TE = 20–640 in steps of 20) respectively. Added to this, examining the effect of flip angle on image contrast requires the incremental acquisition of phantom images, starting at FA = 2° and going on through to FA = 88° or 90° in steps of 2°. These acquisitions are acquired using cardiac-gated cine sequences at both field strengths and with both pulse sequences.

Figure A1 The agarose gel phantoms are positioned within the Eurospin test object and placed inside the head coil for imaging.

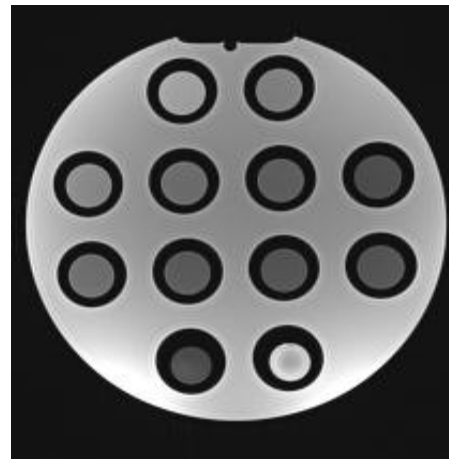**Figure A2** An image of the gel phantoms acquired at 1.5T.

The images acquired at 3.0T were analysed in the traditional way. Each cine acquisition was pulled forward onto a remote work station and regions of interest (ROIs) were manually placed on each of the gel, water and oil phantoms. This was performed on the first image frame of each of the 25 framed cine acquisitions (Figure A2) using the manufacturer's software

(Argus, Siemens Healthcare, Erlangen, Germany). Placement of the ROIs provides quantitative signal information such as the mean signal value within the ROI (+/- the standard deviation (SD) of the mean) plus the maximum and minimum signal within the ROI.

To calculate the T1 and T2 values of each of the phantoms, the mean signal +/- SD had to be manually entered into an Excel spreadsheet so that the signal values could be plotted against TR and TE respectively. The flip angle data was handled in the same way but this time signal was plotted against changing flip angle.

 This analysis technique proved both time consuming and laborious. It was also open to human error due to the large number of signal measurements that have to be manually transferred from the workstation to the spreadsheet. This inefficient, and potentially inaccurate, method was the motivating force to produce a time-efficient method of dealing with this data that was accurate and reproducible.
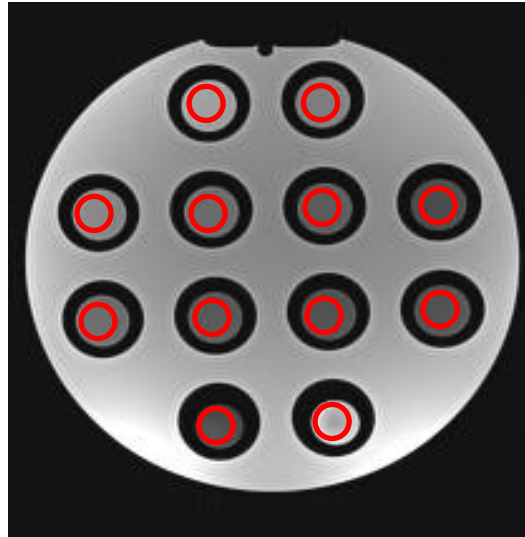
Figure A3 Each image had ROIs placed over the gel, oil and water phantoms.

A2.3 The Environment

The following work was performed in the MAT LAB® (Math Works, Natick, USA) environment and the novel MATLAB script created during this work is summarised in Appendix B of this thesis.

A2.4 The Aim

The purpose of this work was to provide a compact block of functions that would efficiently handle the large volumes of images acquired. These functions needed to be easily transportable between machines (computers) that had the MATLAB environment installed.

A2.5 The Code

A class of type MRI data was created that contained all the properties and methods required for processing all the TR TE and FA data obtained during the spin density measurements.

A2.6 The Files

The images acquired during the routine QA testing of the 1.5T Avanto were copied from the scanner onto a CD-ROM and loaded into MATLAB. Placing these images in the MATLAB environment automatically separated each cine series into 25 individual images, creating 2000 individual files in total. Each file was automatically labelled with a series of numbers (string) (e.g. 21009738) rather than a recognisable label (Figure A4). This presented an immediate problem as the strings bore no relation to the file content. This meant that the only way to determine the content of each file was to open the image DICOM headers using MATLAB's image processing toolbox. This was an inefficient process similar to that of transferring the signal measurements from the work station to the Excel file in the previous method. Therefore, the first step in this work was to create a method for renaming files so that they were instantly recognisable.

A2.7 Renaming the Files

The MRI data class provides a method for renaming all files dynamically. The file names are generated automatically based on the metadata found in the respective DICOM header files of the images (Figure A5). (An example of a DICOM header is attached to the end of this chapter for the interested reader.) The renaming task is performed by initiating the class and selecting the relevant option at the prompt (see example below). The operator then has the

option to process the TR, TE or FA data. Each option will provide the operator

with a range of prompts that work to set up the processing stage.

EXAMPLE 1: Renaming files

 Instantiate the class by creating a variable,

  >> data = MRIdata;

> Select from the following processing options

----

1. Rename DICOM files

2. Flip angle data

3. TR data

4. TE data

0. End processing

 > processing option -->

Selecting option '1' will rename the files. The class will then return to this point to continue processing the data. Option '0' can be selected to exit the process. The files can also be renamed without initiating the class using:

MRIdata.renameDICOMfiles

This will perform the task without presenting any prompts.

21009578	05/04/2010 15:10	File	193 KB
21009594	05/04/2010 15:10	File	193 KB
21009610	05/04/2010 15:10	File	193 KB
21009626	05/04/2010 15:10	File	193 KB
21009642	05/04/2010 15:10	File	193 KB
21009658	05/04/2010 15:10	File	193 KB
21009674	05/04/2010 15:10	File	193 KB
21009690	05/04/2010 15:10	File	193 KB
21009706	05/04/2010 15:10	File	193 KB
21009722	05/04/2010 15:10	File	193 KB
21009738	05/04/2010 15:10	File	193 KB
21009754	05/04/2010 15:10	File	193 KB
21009770	05/04/2010 15:10	File	193 KB

Figure A4 Each file is automatically labelled with a string in the MATLAB environment.

Cine_trueFISP_FA02_1....	01/08/2011 16:13	dcmFile	131 KB
Cine_trueFISP_FA02_2....	01/08/2011 16:13	dcmFile	131 KB
Cine_trueFISP_FA02_3....	01/08/2011 16:13	dcmFile	131 KB
Cine_trueFISP_FA02_4....	01/08/2011 16:13	dcmFile	131 KB
Cine_trueFISP_FA02_5....	01/08/2011 16:13	dcmFile	131 KB
Cine_trueFISP_FA02_6....	01/08/2011 16:13	dcmFile	131 KB
Cine_trueFISP_FA02_7....	01/08/2011 16:13	dcmFile	131 KB
Cine_trueFISP_FA02_8....	01/08/2011 16:13	dcmFile	131 KB
Cine_trueFISP_FA02_9....	01/08/2011 16:13	dcmFile	131 KB
Cine_trueFISP_FA02_10...	01/08/2011 16:13	dcmFile	131 KB
Cine_trueFISP_FA02_11...	01/08/2011 16:13	dcmFile	131 KB
Cine_trueFISP_FA02_12...	01/08/2011 16:13	dcmFile	131 KB

Figure A5 An example of some renamed files.

To continue processing the data, the operator must select option 2, 3 or 4.

As an example, option 3 for processing the TR data will be selected.

> processing option --> 3

This selection sets the procedure for starting the processing and organisation of the data. The operator then needs to set the working directory in response to 'type the full string for the directory to process'.

This will be of the form C:\Users\John Smith\mriData\". NB: This directory should point to the directory with the renamed files and not the originals.

> type the full string for the directory to process:

C:\Users\Shona\Documents\MRI\all data\data\TR.

The operator will then be prompted for the range of files to process. The TR data is slightly different to the TE and FA data due to the irregular range over which the TRs need to be acquired. As they cannot simply be defined in a step-wise fashion, a MATLAB vector is expected for this prompt. The TE and FA methods simply prompt for the starting, ending and step points.

> select the range of TRs to process : NOTE: TR range is in format [start, next, next+1, ...] For the data acquired on the Avanto, this would be of the form:

type TR range (use [ ] for more than one file): [100:50:500, 500:100:1000, 1500, 2000, 3000, 5000, 10000]

Finally, the operator is prompted to provide the number of ROIs for analyses. This allows the operator to analyse any or all of the phantom gels and so the response should be a number in the range of 1 to 12.

> How many masks/ROIs would you like to create? 12

A3 Measuring the Signal

Once this number has been returned, an image of the agarose, oil and water filled phantoms will appear in a window. Each phantom image is labelled with a number, in this case ROI number 1 (Figure A6). The operator is then required to manually place an ROI on the first gel by holding down the left hand button of the mouse and dragging it over the gel. If the resulting ROI is not in the correct position, it can be highlighted and moved by the operator.
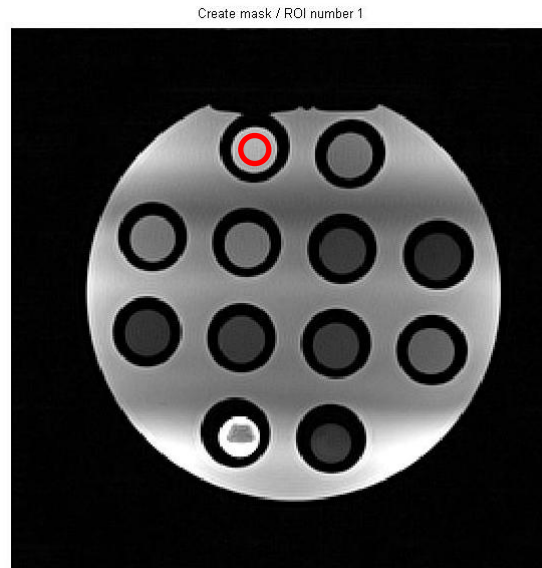
Figure A6 The operator places an ROI on gel 1.

Once the ROI is in place, the operator is required to double click on the image. This automatically replaces the image labelled ROI number 1 with the image labelled ROI number 2. The operator now places an ROI on the second gel (Figure A7).
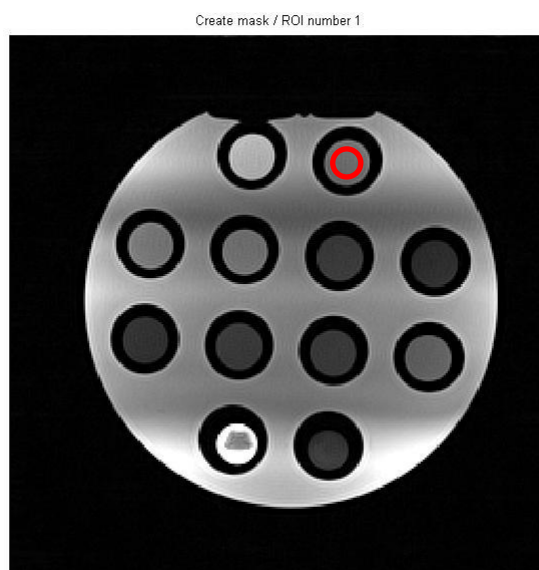
Figure A7 When the second image appears, the operator places an ROI on gel number 2.

A3.1 Plotting the data

This process is repeated until all the required phantoms have ROIs placed on them. The ROIs are then stored and converted to binary masks, which are then applied to each of the 25 frames of the cine series, for each TR value. This process is concluded with the option of plotting the data. The response to this option can be of the form, "y", "yes", "n" or "no". The case of the response is not considered and thus can be either. For example:

> would you like to plot the data? **yes**

or

> would you like to plot the data? **y**

By selecting to plot the data, MATLAB will produce a graph for each of the ROIs selected at the start of the process (Figure A8). The operator can also choose to plot the data at a later date by selecting "no". The plotting routine (function) can then be invoked at a later time by calling the relevant method (class function):

data = data.plotMRIdata;
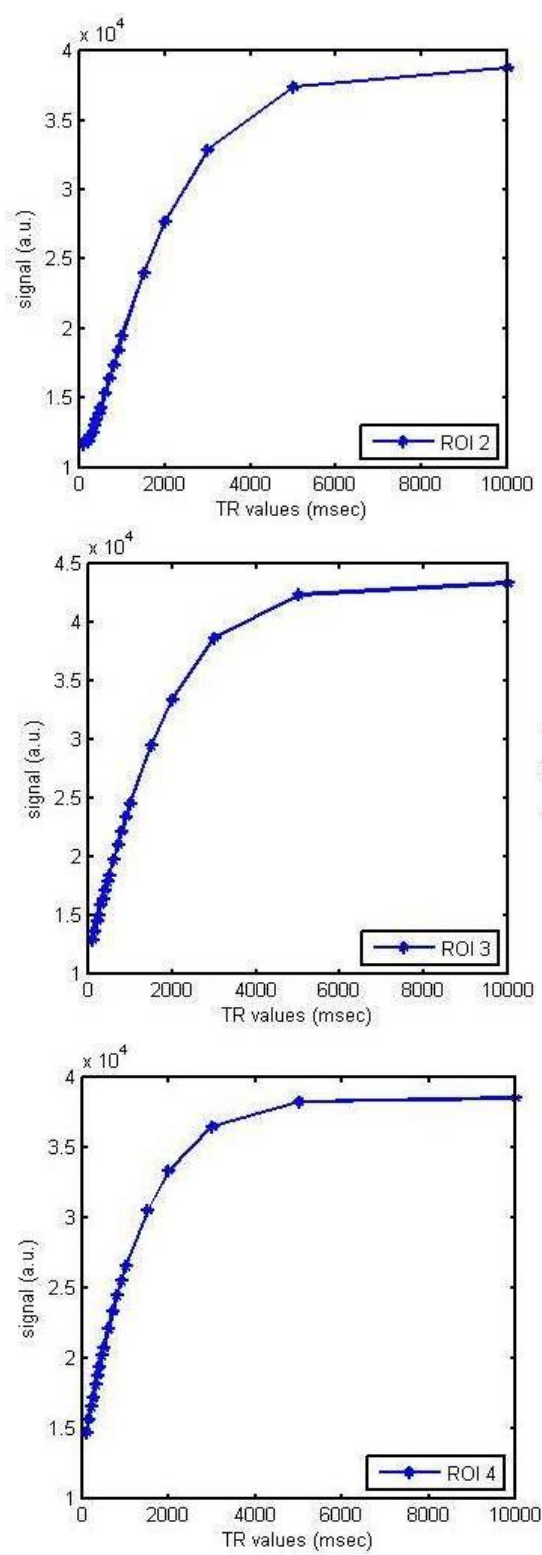
Figure A8 By selecting to plot the data, MATLAB will produce plots for each of the selected ROIs as can be seen here

for ROIs 2, 3, and 4.

A4 Calculating T1 Relaxation Rates

Once plots have been created of signal v TR, an accurate calculation of the T1 relaxation rates of the gel, oil and water phantoms can be obtained simply by using a fitting routine. This process is invoked via the relevant method calls:

data = data.calcT1;

The operator is then asked to examine each plot and, through a series of prompts, to choose the range over which the T1 relaxation rates should be calculated. The results of the fit are stored in the class property 't1' or 't2' and are accessed via: data.t1
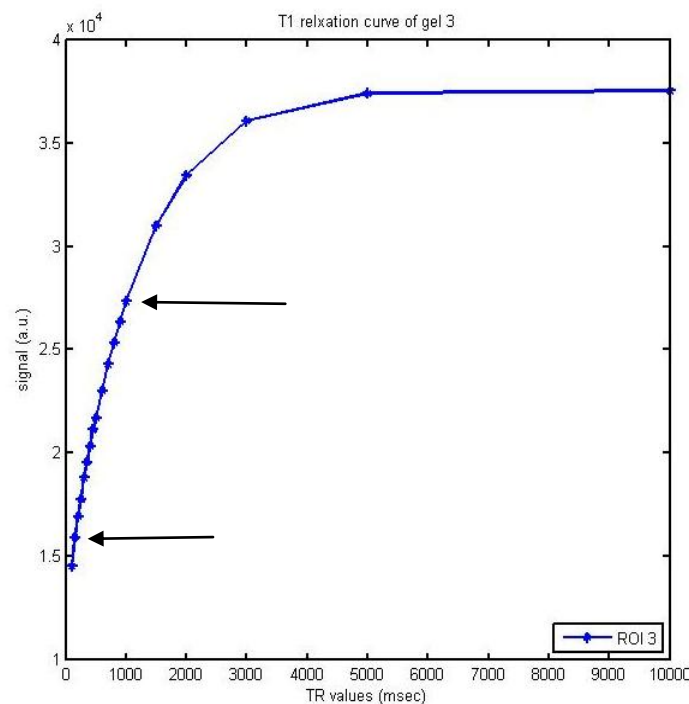
Figure A9 The operator visually selects the range over which the T1 values of the gel will be calculated.

Once these values have been fed into MATLAB, the fitting routine plots the fit of the chosen gel in a separate figure. An example of these fits for ROI 2, 3 and 4 can be seen in Figures A10, A11 and A12.
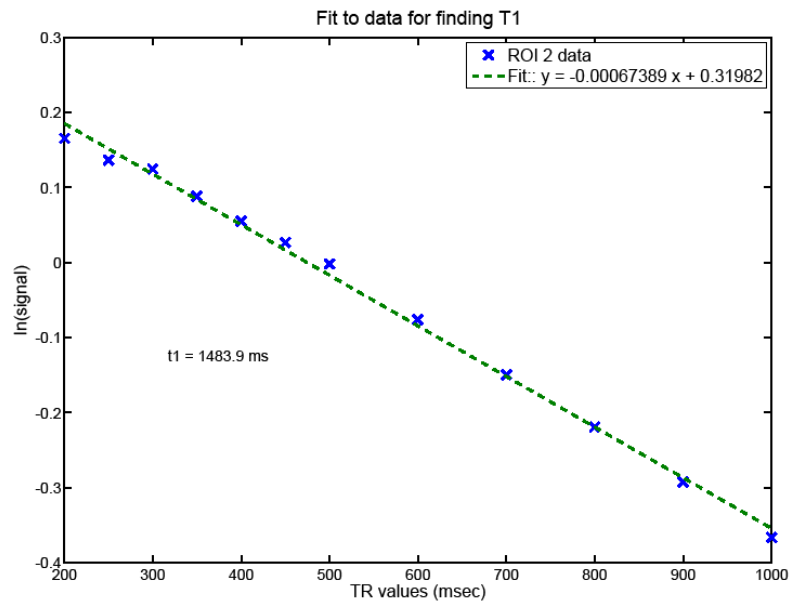
Figure A10 By plotting the fit for ROI 2, the T1 value can be calculated in MATLAB.
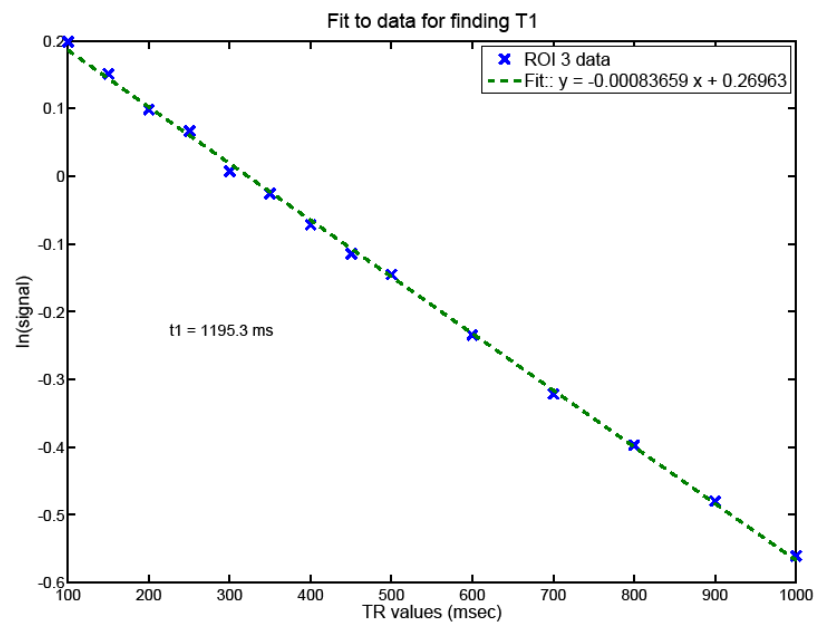
Figure A11 By plotting the fit for ROI 3, the T1 value can be calculated for this gel.
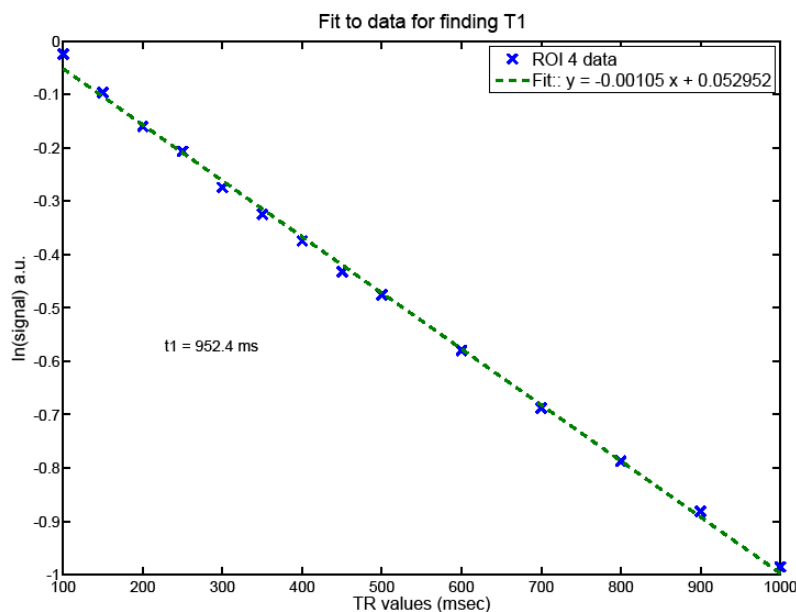
Figure A12 By plotting the fit for ROI 4, the T1 value can be calculated for this gel.

Once this step is completed for each gel, the calculated T1 values can then be compared to the known theoretical values. In the examples provided in this sub-chapter, the calculated values of T1 for the gels in ROI 1, 2 and 3 were 1483.9ms, 1195.3ms and 952.4ms. These values compare favourably with the theoretical values for these gels, which are 1480ms, 1261ms and 959ms respectively at 292K.

A4.1 TE Data

This time-efficient and accurate process can be repeated using the TE data (Figure A12) simply by selecting the relevant prompts, at the start of the exercise. The operator should ensure that the correct directory is also selected; for example, if the operator wanted to calculate the T2 values of the gels:

> Select from the following processing options

----

1. Rename DICOM files

2. Flip angle data

3. TR data

4. TE data

Then option 4 would be selected and the directory would change from:

> type the full string for the directory to process:

     C:\Users\Shona\Documents\MRI\all data\data\TR.

to:

> type the full string for the directory to process:

     C:\Users\Shona\Documents\MRI\all data\data\TE.

Care should also be taken at other prompts; for example:

data = data.calcT1; should be replaced by data = data.calcT2;
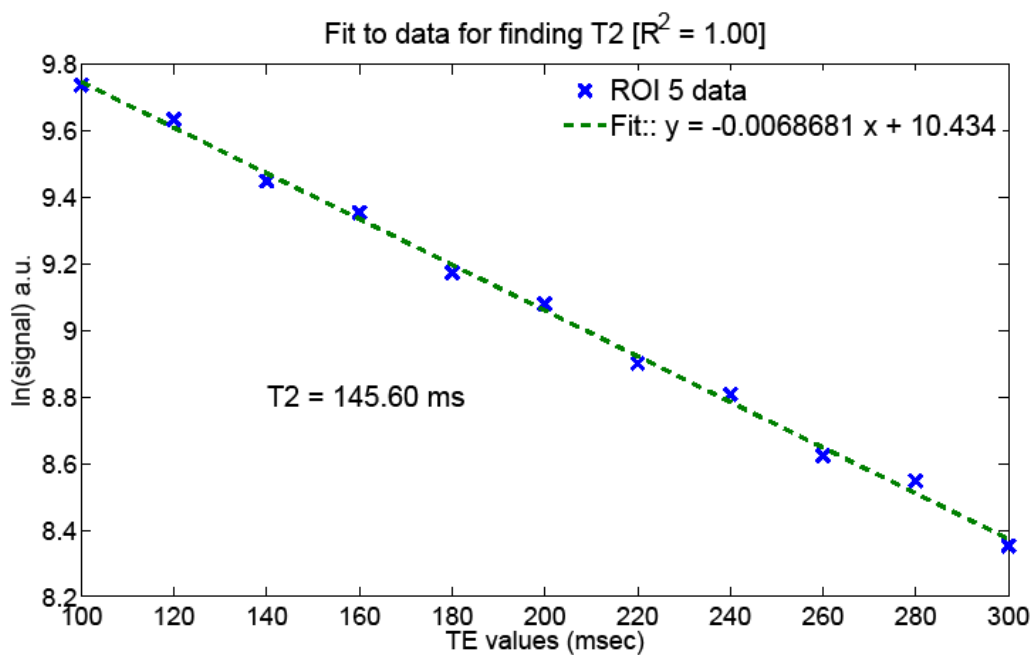
Figure A13 T2 relaxation values for each gel can be determined by using the TE data and selecting the relevant prompts.

A4.2 Flip Angle Data

The flip angle data should be treated in the same way up until the plotting stage. At this point, the operator will be given the option to plot the signal v instance number or plot the signal v flip angle (see below). Plotting the signal v instance number allows the operator plot a graph detailing how the signal changes throughout each 25-frame cine acquisition, whilst plotting signal v flip angle will give the operator a picture of how flip angle effects image contrast.

> Flip Angle data

1. create plot of Signal vs. instance number (time)

2. create plot of Signal vs. flip angle

An example of the type of the information available in an image DICOM header.

1	Format	DICOM
2	FormatVersion	3
3	Width	256
4	Height	256
5	BitDepth	16
6	ColorType	Grayscale
7	FileMetaInformationGroupLength	210
8	FileMetaInformationVersion	[2x1 uint8]
9	MediaStorageSOPClassUID	1.2.840.10008.5.1.4.1.1.4
10	MediaStorageSOPInstanceUID	1.3.6.1.4.1.9590.100.1.2.228772607612717533806987
11	TransferSyntaxUID	1.2.840.10008.1.2.1
12	ImplementationClassUID	1.3.6.1.4.1.9590.100.1.3.100.7.1
13	ImplementationVersionName	MATLAB IPT 7.1
14	SpecificCharacterSet	ISO_IR 100
15	ImageType	ORIGINAL\PRIMARY\M\RETRO\DIS2D
16	InstanceCreationDate	20100405
17	InstanceCreationTime	143317.421000
18	SOPClassUID	1.2.840.10008.5.1.4.1.1.4
19	SOPInstanceUID	1.3.6.1.4.1.9590.100.1.2.228772607612717533806987
20	StudyDate	20100405
21	SeriesDate	20100405
22	AcquisitionDate	20100405
23	ContentDate	20100405
24	StudyTime	112253.906000
25	SeriesTime	143317.421000
26	AcquisitionTime	143303.417500

27	ContentTime	143317.421000
28	AccessionNumber	''
29	Modality	MR
30	Manufacturer	SIEMENS
31	InstitutionName	NINEWELLS HOSPITAL AVANTO
32	InstitutionAddress	Ninewells,GB,DD1 9SY
33	ReferringPhysicianName	[1x1 struct]
34	StationName	MRC25176
35	StudyDescription	PHYSICS^QUALITY ASSURANCE
36	SeriesDescription	Cine_trueFISP_FA02
37	PerformingPhysicianName	[1x1 struct]
38	ManufacturerModelName	Avanto
39	ReferencedImageSequence	[1x1 struct]
40	PatientName	[1x1 struct]
41	PatientID	test_05042010
42	PatientBirthDate	19700101
43	PatientSex	O
44	PatientAge	040Y
45	PatientWeight	50
46	ScanningSequence	GR
47	SequenceVariant	SK\SS\OSP
48	ScanOptions	CT
49	MRAcquisitionType	2D
50	SequenceName	*tfi2d1_15
51	AngioFlag	N
52	SliceThickness	10
53	RepetitionTime	47.8500
54	EchoTime	1.3600
55	NumberOfAverages	1
56	ImagingFrequency	63.6816
57	ImagedNucleus	1H
58	EchoNumber	1
59	MagneticFieldStrength	1.5000
60	NumberOfPhaseEncodingSteps	286
61	EchoTrainLength	1
62	PercentSampling	100
63	PercentPhaseFieldOfView	100

64	PixelBandwidth	930
65	DeviceSerialNumber	25176
66	SoftwareVersion	syngo MR B15
67	ProtocolName	Cine_trueFISP_FA02
68	TriggerTime	0
69	NominalInterval	1000
70	CardiacNumberOfImages	25
71	TransmitCoilName	Body
72	AcquisitionMatrix	[4x1 uint16]
73	InPlanePhaseEncodingDirection	COL
74	FlipAngle	2
75	VariableFlipAngleFlag	N
76	SAR	3.5875e-004
77	dBdt	0
78	PatientPosition	HFS
79	StudyInstanceUID	1.3.12.2.1107.5.2.30.25176.30000010040510225339210
80	SeriesInstanceUID	1.3.12.2.1107.5.2.30.25176.2010040514331558306800
81	StudyID	1
82	SeriesNumber	23
83	AcquisitionNumber	1
84	InstanceNumber	1
85	ImagePositionPatient	[3x1 double]
86	ImageOrientationPatient	[6x1 double]
87	FrameOfReferenceUID	1.3.12.2.1107.5.2.30.25176.2.20100405112254203.
88	PositionReferenceIndicator	''
89	SliceLocation	-1.3629e-008
90	ImageComments	RR 1000 +/- 2; 11 heartbeats
91	SamplesPerPixel	1
92	PhotometricInterpretation	MONOCHROME2
93	Rows	256
94	Columns	256

References

1. Haacke EM, Brown RW, Thompson MR, Venkatesan R. *Magnetic Resonance Imaging, Physical Principles and Sequence Design.* New York: John Wiley & Sons, 1999.

2. Reeder SB, Herzka DA, McVeigh ER. Signal-to-Noise Ratio Behaviour of Steady-State Free Precession. *Magnetic Resonance in Medicine* 2004: **52**; 123–130.

Appendix B. Matlab® code

This appendix summarises the MRIdata class discussed in chapter 4b of this thesis. It was created using Matlab® with the aim of simply and efficiently processing the large volumes of MRI data acquired as part of the departments regular quality assurance testing and/or installation procedures.

A full copy of the latest version of the MRIdata Matlab class is included on the accompanying CD. This is stored in the "MRIdata class" directory; and is included in the matlab script file "MRIdata.m".

B1 Header

The header or help section for the MRIdata class gives an indication on how to use the class for processing the MRI data.

```
% This file generates a class of type "MRIdata". It contains all the
% properties and methods required for processing Flip Angle, TR and TE
% data obtained from the MRI scanner in Ninewells Hospital.
% The purpose of this class is to provide a compact block of functions
% which are efficient and can be easily transported between machines
% with the MATLAB environment installed.
% The files from the MRI scanner come with meaningless file names. So,
% before any processing can be done these files have to be renamed.
% The MRIdata class provides a method for renaming the files
% dynamically. Point the class to the base directory with the raw
% files, and the renamed files will be stored in a sub-directory named
% "\renamedFiles". The file names will be generated automatically based
% on the meta data found in the respective DICOM files. To perform this
% renaming task simply instantiate the class and select the relavant
% option at the prompt. See the example below. Alternatively, you can
% perform this task without instanciating the class as the method does
% not depend on the class properties or methods. See the second example
% below.
% The user then has the option to process the data, either the Flip
% Angle (FA), the TR, and/or the TE data. Each option will then give
% the user a range of prompts which work to set up the processing
% stage. An example for the TR data is shown in Example 3.
```

```
% EXAMPLE 1: Renaming files
% Instantiate the class by creating a variable,
% data = MRIdata;
% This calls the constructor for the class, and provides an initial
% prompt for selecting a range of options. Select option "1" to rename
% the files. The class will return to this point to continue processing
% the data. Option "0" to exit.
% EXAMPLE 2: Renaming files, without instantiating the class.
% MRIdata.renameDICOMfiles
% This performs the renaming without instantiation, and will not
% present any prompt.


% EXAMPLE 3: Process data - TR for illustration
% data = MRIdata;
% Option "3" in response to "processing option --> "
% This results in the setting procedure for starting the processing and
% organisation of the data.
% Set the working directory in response to "type the full string for
% the directory to process: ", this will be of the form,
% C:\Users\John Smith\mriData\"
% NB: This directory should point to the directory with the renamed
% files and not the originals.
% Next the user is prompted for the range of files to process. The TR
% data is slightly different and expects a MATLAB vector. The other
% methods prompt for the starting, ending and step points.
% This arose from the files that were to be processed. This should be
% changed in future versions.
% an example would be of the form,
% [100:50:500, 600, 1000, 3000]
% For files with TR values
% 100, 150, 200, 250, 300, 350, 400, 450, 500, 600, 1000, 3000.
% Finally, the user is requested to provide the number of ROIs that
% will be created. The first image in the series is then displayed for
% the creation of each ROI. These are then stored and converted to
% binary masks, which are then applied to each image for each ROI.
% The process is concluded with the option of plotting the data. The
% response can be of the form,
% "y", "yes", "n" or "no"
% The case of the response is not considered and thus can be either.
% If you would like to plot at a later date simply invoke the
% plotting method by calling the relevant method,
% data = data.plotMRIdata;
% For TE and TR data, a fitting routine is available to find either the
% T1 or T2 values. These are invoked via the relevant method calls,
% data = data.calcT1;
% or,
% data = data.calcT2;
% The user is then asked the range to calculate the fit from via a
% series of prompts like before. The results of the fit are stored in
% the class property "t1" or "t2" and are accessed via,
% data.t1
% or,
% data.t2
% The fitting routine also plots, in a separate figure, the fit results
% for the specific ROI selected.
%  MATLAB by Dr Tom Gallacher  email: thomas.gallacher@gmail.com
```

```
%  MRI theory by Shona Matthew
% Class version: $v4.4
```

B2 Class data members

MRIdata class and its data members define the variables that are used to store the MRI data as it is processed.

*Constant means variable does not change and can be accessed without creating an "instance" of the MRIdata class.

*SetAccess + GetAccess determines whether those variables can be accessed from the matlab command window, i.e. outside the class. "public" means the variables can be accessed and "private or protected" means that only functions internal to the class can access the variables.

```
properties (Constant)
version = '4.4';
end

properties (SetAccess = public, GetAccess = public)
tr_Data = struct;         % intensity data - TR
te_Data = struct;         % intensity data - TE
fa_Data = struct;         % intensity data - FA

t1
t2

s0_in                     % S0 input for T1 fit.
s0_out                     % s0 from T1 fit.
r_sq                      % R^2 val - 1 indicates perfect fit to data.
end

properties (SetAccess = protected, GetAccess = protected)
sizeChk           % image size in pixels (one number - img is square)
noROIs             % number of gels/ROIs
noFrames = 25;     % number of frames - usually 25
noFiles            % number of files in cur folder
fa_range            % range of flip angle
tr_range            % range of TR to process
te_range            % range of TE to process
noFA               % number of flip angle files to process
```

```
noTR                % number of TR files to process
noTE                % number of TE files to process

filedata = struct;      % struct for file names
masks = uint16([]);        % holds all the masks

fa_instance_format = '%*s %*s  FA%*d %d %*c %*s';
fa_format =  '%*s %*s  FA%d %*d %*c %*s';
markerSpec = ['+','o','*','.','x','s','d','^','v','>']; % used for plotting

isFA = 0      % flag to indicate if FA data has been processed.
isTR = 0      % flag to indicate if TR data has been processed.
isTE = 0      % flag to indicate if TE data has been processed.
processOption = 0;    %Process option selected. 0 indicates default: no option
selected
processOption_stop = 0; % used in the processMRI while loop
end
```

B3 Class methods (functions)

This section contains a list of the MRIdata methods. These methods are used for processing MRIdata and include routines such as formatting the file names (from metadata generated by the MRI scanner), plotting data, fitting to experimental data, etc.

The methods are grouped into three different blocks that have specific access rights: these are "static", "public", and "protected".

B3.1 Static method block

The static method block is similar to the "constant" data member block (see appendix B1.2); the routine can be performed without creating an instance of the class.

```matlab
methods (Static)
%------- rename DICOM files to something more useful
function renameDICOMfiles(varargin)
% As of v3.3 of class file: varargin format is:
% - varargin{1} -> function handle of status box
% - varargin{2} -> handles struct

%** create new directory for renamed files
newDir = 'renamedFiles';
if nargin == 0 %only display if no input args
disp(' ');
disp('Renaming DICOM files. New files will be put in "renamedFiles" directory');
disp('This directory will be located in the original dicom files folder.');
end

% Check that folder doesn't already exist..
if isdir(newDir);
if nargin == 0
disp(' ');
disp(
'************************************************************'
)
disp(['WARNING:: the folder "' newDir '" already exists. Move these...']);
disp(
'************************************************************'
)
disp(' ');
else
% defined in MRI GUI file
varargin{1}(['WARNING:: the folder "' newDir '" already exists. Move these...'],
varargin{2});
end
else
%** Data setup
inFile = struct(); % preallocate memory - makes it run quicker
NumberOfFiles2Process = 0;

%** Start renaming files
% generate the new folder for the files - generated below
mkdir(newDir);
Direc = [pwd '\' newDir '\'];
%read files from current directory
files = dir();

% how many files is there in the directory
numFiles = length(files);

% find the number of files that are actually DICOM files - used for
% progress check
for k = 1:numFiles
if files(k).isdir == 0
NumberOfFiles2Process = NumberOfFiles2Process + 1;
end
end

if nargin == 0
%progress bar
```

```matlab
pbar = waitbar(0, 'Renaming DICOM files...');
end

%loop over all files in current directory
for i = 1:numFiles
%check file isn't a folder
dirtype = files(i).isdir;

% if this is = 0, then file is not a folder -> process this
if dirtype == 0
% get all info for DICOM file store in 'info'
if isdicom(files(i).name)
info = dicominfo(files(i).name);

% keep hold of the variables that we are interested in.
inFile.name = files(i).name;
inFile.protocolName = info.ProtocolName;
inFile.instanceNumber = info.InstanceNumber;
inFile.EchoTime = info.EchoTime;
curImageData = dicomread(inFile.name);

% create new variable with the string for the new file name
if ~isempty(strfind(inFile.protocolName, 'FA'))
outFilename = [inFile.protocolName '_' num2str(inFile.instanceNumber) '.dcm'];
elseif ~isempty(strfind(inFile.protocolName, 'se_mc'))
outFilename = [inFile.protocolName '_TE' num2str(inFile.EchoTime)  '.dcm'];
elseif ~isempty(strfind(inFile.protocolName, 'TR'))
outFilename = [inFile.protocolName '.dcm'];
end

% write the image to a new file put in the renamed folder.
dicomwrite(curImageData, [Direc outFilename], info, 'CreateMode', 'Copy');
end
% progress bar...
per = i/NumberOfFiles2Process;

if nargin == 0
waitbar(per);
else
varargin{1}(['Renaming files:  percentage done -> ' num2str(per*100)],
varargin{2});
end
end
end
end
if nargin == 0
close(pbar);
else
varargin{1}('Renaming complete', varargin{2});
end
end % end renameDICOMfiles
end % END STATIC
```

B3.2 Public method block

These functions are available for use outside of the class. These functions consist of mainly processing options, i.e. process TR, TE or FA, and for plotting the results of the data processing algorithms. There also functions for obtaining the relaxation time parameters for each respective data process; these routines call private methods which perform the data fitting (see appendix B1.3.3).

```matlab
methods (Access = public)
%------- constructor
function obj = MRIdata(varargin)
disp(['Running MRIdata CLASS Version ' num2str(obj.version)]);
close all

if nargin == 0
obj = obj.processMRI;
end
end %end constructor

%------- process Flip angle (FA) data
function obj =  proc_flipAngle(obj, FArange, varargin)
% v3.3 varargin contains
% - varargin{1} -> noROIs
% - varargin{2} -> function handle to status box
% - varargin{3} -> handles struct for UI controls

obj.isFA = 1;
obj.fa_range = FArange';
obj.noFA = length(FArange);

%reset other TR & TE data
obj.isTR = 0;
obj.isTE = 0;
obj.tr_Data = [];
obj.te_Data = [];

% START PROCESSING
% Sort file in strctured variables (struct)
obj = obj.sortFileNames_fa;
% Create the ROIs
obj = obj.createROIs(varargin);
% Apply to our files
obj = obj.applyROIs(varargin);
```

```matlab
end % end proc_flipAngle()

%------- process TR data
function obj = proc_TR(obj, TRrange, varargin)
% v3.3 varargin contains
% - varargin{1} -> noROIs
% - varargin{2} -> function handle to status box
% - varargin{3} -> handles struct for UI controls

obj.isTR = 1;
obj.tr_range = TRrange;
obj.noTR = length(obj.tr_range);

%reset other TR & TE data
obj.isFA = 0;
obj.isTE = 0;
obj.fa_Data = [];
obj.te_Data = [];

% START PROCESSING
% Sort file in strctured variables (struct)
obj = obj.sortFileNames_tr;
% Create the ROIs
obj = obj.createROIs(varargin);
% Apply to our files
obj = obj.applyROIs(varargin);
end %end proc_TR()

%------- process TE data
function obj = proc_TE(obj, TErange, varargin)
% v3.3 varargin contains
% - varargin{1} -> noROIs
% - varargin{2} -> function handle to status box
% - varargin{3} -> handles struct for UI controls

obj.isTE = 1;
obj.te_range = TErange;
obj.noTE = length(TErange);

%reset other TR & TE data
obj.isTR = 0;
obj.isFA = 0;
obj.tr_Data = [];
obj.fa_Data = [];

% START PROCESSING
% Sort file in strctured variables (struct)
obj = obj.sortFileNames_te;
% Create the ROIs
obj = obj.createROIs(varargin);
% Apply to our files
obj = obj.applyROIs(varargin);
end % end proc_TE()

%------ plotting data
function varargout = plotMRIdata(obj, varargin)
close all
```

```matlab
% only display if not using GUI
if nargin == 1
if obj.processOption == 0 || obj.processOption == 2
%options
disp(' ');
disp(' ');
disp('--------------------------------------------------------------');
disp('To process MRI data, choose from the following options');
disp('--------------------------------------------------------------');
disp(' ');
disp('> Flip Angle data');
disp('1. create plot of Signal vs. instance number (time)');
disp('2. create plot of Signal vs. flip angle');
disp(' ');
disp('> TR data');
disp('3. create plot of Signal vs. TR value');
disp(' ');
disp('> TE data');
disp('4. create plot of Signal vs. TE value');

disp(' ');
optNum = input('> option number:  ');
disp(' ');
else
optNum = obj.processOption;
end
end


if nargin == 2
optNum = varargin{1};
end

%%% option 1.   *FA data*
if optNum == 1
%get plot range (if not using GUI)
if nargin == 1
plt_fa_range = obj.opt1plotRange;
else
if nargin  == 2 %no plot range present

farangeMIN = obj.fa_Data(1,1).angle;
farangeMAX = obj.fa_Data(end,1).angle;

if length(obj.fa_Data) ~= 1
farangeSTEP = obj.fa_Data(2,1).angle - obj.fa_Data(1,1).angle;
else
farangeSTEP = 1;
end
plt_fa_range = farangeMIN:farangeSTEP:farangeMAX;

else
if nargin == 4
plt_fa_range = varargin{2}:varargin{3}:varargin{4};
else
error('MRIdata::no enough plot range arguments passed to plotMRIdata()');
```

```matlab
end
end
end
% Xaxis
x = 1:obj.noFrames;

% Start plotting with separate windows for each angle
for FAitr = 1:length(plt_fa_range)

% sort out the plot window
if length(plt_fa_range) <= 3
subplot(1,3,FAitr);
elseif length(plt_fa_range) > 3 && length(plt_fa_range) < 7
subplot(2,3,FAitr);
end

if length(plt_fa_range) >= 7
if FAitr > 6
if mod(FAitr,6) == 1
figure
end
end
if mod(FAitr,6) == 0
subplot(2, 3, 6)
else
subplot(2, 3, mod(FAitr,6))
end
end %end sorting out plot window

% Do the plotting
for z = 1:obj.noFA
%loop over all FA files. if FA number has been selected -> plot it
if plt_fa_range(FAitr) == obj.fa_Data(z,1).angle;
%plot signal for all gels for each selected FA
for GELitr = 1:obj.noROIs
y = obj.fa_Data(z,1).roi(GELitr,1).signal;
plot(x, y, [obj.markerSpec(GELitr) '-'],'LineWidth', 2);
hold all
axis tight
xlabel('instance number');
ylabel('signal');
set(gca, 'LineWidth', 1.5);
set(gcf, 'Position', [0 0 1280 750]);
end
% sort out legend
obj.applyLegend;
title(['Flip angle - ' num2str(plt_fa_range(FAitr))]);
end
end
end
hold off
end

%% Option 2 *FA data*
if optNum == 2
% loop over all ROIs
for GELitr = 1:obj.noROIs
```

```matlab
% loop over all Flip Angles and get corresponding signal
for FAitr = 1:obj.noFA
x(FAitr) = obj.fa_Data(FAitr,1).angle;
y(FAitr) = obj.fa_Data(FAitr,1).roi(GELitr,1).signal(1);
end

% plot data
plot(x, y, [obj.markerSpec(GELitr) '-'], 'LineWidth', 2);
hold all
axis tight
xlabel('flip angle');
ylabel('signal');
clear x y
end

% sort out gel
obj.applyLegend;
set(gca, 'LineWidth', 1.5);
hold off
end

%% Option 3 *TR data*
if optNum == 3
% loop over all ROIs
for ROIitr = 1:obj.noROIs

% sort out the plot window
if obj.noROIs <= 3
subplot(1,3,ROIitr);
elseif obj.noROIs > 3 && obj.noROIs < 7
subplot(2,3,ROIitr);
end

if obj.noROIs >= 7
if ROIitr > 6
if mod(ROIitr,6) == 1
figure
end
end
if mod(ROIitr,6) == 0
subplot(2, 3, 6)
else
subplot(2, 3, mod(ROIitr,6))
end
end %end sorting out plot window


% loop over all TRs and get corresponding signal
for TRitr = 1:obj.noTR
x(TRitr) = obj.tr_Data(TRitr,1).TRval;
y(TRitr) = obj.tr_Data(TRitr,1).roi(ROIitr,1).signal;
end

% plot data
plot(x, (y), '*-', 'LineWidth', 2);
hold all
axis square
```

```matlab
xlabel('TR values (msec)');
ylabel('signal (a.u.)');
legend(['ROI ' num2str(ROIitr)]);
legend('Location', 'SouthEast');
set(gca, 'LineWidth', 1.5);
xlim([0 x(end)]);
clear x y
end
hold off
end

%% Option 4 *TE data*
if optNum == 4
% loop over all ROIs
for ROIitr = 1:obj.noROIs

% sort out the plot window
if obj.noROIs <= 3
subplot(1,3,ROIitr);
elseif obj.noROIs > 3 && obj.noROIs < 7
subplot(2,3,ROIitr);
end

if obj.noROIs >= 7
if ROIitr > 6
if mod(ROIitr,6) == 1
figure
end
end
if mod(ROIitr,6) == 0
subplot(2, 3, 6)
else
subplot(2, 3, mod(ROIitr,6))
end
end %end sorting out plot window

% loop over all TRs and get corresponding signal
for TEitr = 1:obj.noTE
x(TEitr) = obj.te_Data(TEitr,1).TEval;
y(TEitr) = obj.te_Data(TEitr,1).roi(ROIitr,1).signal;
end

% plot data
plot(x, y, 'x' , 'LineWidth', 2, 'MarkerSize', 10);
hold all
axis square
xlabel('TE values (msec)');
ylabel('signal (a.u.)');
legend(['ROI ' num2str(ROIitr)]);
legend('Location', 'NorthEast');
set(gca, 'LineWidth', 1.5);
xlim([0 x(end)]);
clear x y
end
hold off
end
```

```matlab
if nargout == 1
varargout{1} = obj;
end
end % end plotMRIdata()

%------- process MRI data prompt function
function obj = processMRI(obj)
% processMRIdata
%
%   This is the master function which will guide you through the processing
%   of all MRI data. This script currently supports:
%
%       - renaming all files to something more meaningful
%       - processing flip angle data (both TrueFISP & FLASH)
%       - processing TR data
%       - processing TE data
%
%  To plot this data use the plotMRIdata method.
%
%
%   $vc1  (class version)
%
%   Shona Matthew


disp(' ');
disp('    **** Processing MRI data ****');
disp(' ');
disp('NOTE:: DICOM files have to be renamed before processing!!!');
disp(' ');

while obj.processOption_stop ~= 1

disp('> Select from the following processing options');
disp('--------------------------------------------');
disp('1.   Rename DICOM files');
disp('2.   Flip angle data');
disp('3.   TR data');
disp('4.   TE data');
disp(' ');
disp(' ');
disp('0.   End processing');
disp(' ');
obj.processOption = input('> processing option --> ');
disp(' ');




% string holding the directory to do the processing on
if obj.processOption ~= 0
pDir = input('> type the full string for the directory to process: ', 's');
disp(' ');
%change the current directory to the folder containg the data
cd(pDir);
end

%* Option 1 - rename dicom files
```

```matlab
if obj.processOption == 1
obj = obj.renameDICOMfiles;
end

%* Option 2 - Flip angle data
if obj.processOption == 2
disp('> select the range of flip angles to process');
disp(' ');
startFA = input('> starting flip angle:  ');
endFA = input ('> ending flip angle:  ');
stepFA = input('> flip angle steps:  ');

range = startFA:stepFA:endFA;
% run the processing script
obj = obj.proc_flipAngle(range);

%quit the function now that data has been processed
obj.processOption_stop = 1;
end

%* Option 3 - TR data
if obj.processOption == 3
disp('> select the range of TRs to process');
disp('::NOTE: TR range is in format - [start, next, next+1, ....]');
disp(' ');

range = input('> type TR range (use [ ] for more than one file):  ');
% run the processing script
obj = obj.proc_TR(range);

%quit the function now that data has been processed
obj.processOption_stop = 1;
end

%* Option 4 - TE data
if obj.processOption == 4
disp('> select the range of TEs to process');

startTE = input('> starting TE:  ');
endTE = input ('> ending TE:  ');
stepTE = input('> TE steps:  ');

range = startTE:stepTE:endTE;
% run the processing script
obj = obj.proc_TE(range);

%quit the function now that data has been processed
obj.processOption_stop = 1;
end

% Quit the class.
if obj.processOption == 0
obj.processOption_stop = 1;
end

end %end while loop
```

```matlab
% reset stop flag.
obj.processOption_stop = 0;

% Do not print if quit
if obj.processOption ~= 0
disp(' ');
disp('---------------------------------------------------------------');
plt = input('> would you like to plot the data?  ', 's');

switch lower(plt)
case 'y'
obj = obj.plotMRIdata;
case 'yes'
obj = obj.plotMRIdata;
case 'n'
disp('> Use ".plotMRIdata" to plot data');
case 'no'
disp('> Use ".plotMRIdata" to plot data');
end
disp(' ');
else
disp('> MRIdata process quit. ');
end
end % end processMRI()

%------- process gradient T2 for TE data
function obj = calcT2(obj)

xStart = input('Starting x val --> ');
xStop = input('Stopping x val --> ');
ROIno = input('ROI number --> ');

figure
%get data
for TEitr = 1:obj.noTE
x(TEitr) = obj.te_Data(TEitr,1).TEval; %#ok<AGROW>
y(TEitr) = obj.te_Data(TEitr,1).roi(ROIno,1).signal; %#ok<AGROW>
end

% Truncate the data to the specified region
stopIdx = find(x == xStop);
startIdx = find(x == xStart);

%Re-arrange formula
yf = log(y(startIdx:stopIdx));

%plot data
plot(x(startIdx:stopIdx), yf, 'x', 'MarkerSize', 12, 'Linewidth', 1.5);
xlabel('TE values (msec)');
ylabel('ln(signal) a.u.');

set(gca, 'LineWidth', 1.5);

% calc gradient & plot fit
[g,c] = obj.getGradient(x(startIdx:stopIdx), yf);
obj.t2 = -1/g;
hold all
```

```matlab
fit = g*x(startIdx:stopIdx) + c;

% work out R^2 - 1 indicates perfect fit!
sse = sum((fit - yf).^2);
ssr = sum((fit - mean(yf)).^2);
obj.r_sq = ssr/(ssr+sse);

% Add fit to the plot
plot(x(startIdx:stopIdx), fit, '--', 'Linewidth', 1.5);
legend(['ROI ' num2str(ROIno) ' data'], ['Fit:: y = ' num2str(g) ' x + '
num2str(c)]);
legend('Location', 'NorthEast');
title(['Fit to data for finding T2 [R^2 = ' num2str(obj.r_sq, '%0.2f') ']']);
hold off;

clear x y stopIdx ROIno
end

%------- process gradient T1 for TR data
function obj = calcT1(obj)
disp(' ');
xStart = input('Starting x val --> ');
xStop = input('Stopping x val --> ');
ROIno = input('ROI number --> ');

figure
%get data
for TRitr = 1:obj.noTR
x(TRitr) = obj.tr_Data(TRitr,1).TRval; %#ok<AGROW>
y(TRitr) = obj.tr_Data(TRitr,1).roi(ROIno,1).signal; %#ok<AGROW>
end

% Y should be ln(y) to give rising exponential
%            y = log(y);

% Truncate data to specified region
stopIdx = find(x == xStop);
startIdx = find(x == xStart);

%output s0 in (taken from data)
obj.s0_in = max(y);

%Re-arrange formula
%            yf = log(max(y) - y(startIdx:stopIdx));
yf = log(1.8080e3 - y(startIdx:stopIdx));

%plot data
plot(x(startIdx:stopIdx),  yf, 'x', 'MarkerSize', 12, 'Linewidth', 1.5);
xlabel('TR values (msec)');
ylabel('ln(signal) a.u.');

set(gca, 'LineWidth', 1.5);

% calc gradient & plot fit
[g, c, err] = obj.getGradient1( x(startIdx:stopIdx), yf);
obj.err = err; %return err details of polyfit
```

```matlab
%output S0 (y-intercept) point from fit.
obj.s0_out = exp(c);

obj.t1 = -1/g;
hold all
fit = g*x(startIdx:stopIdx) + c;

% work out R^2 - 1 indicates perfect fit!
sse = sum((fit - yf).^2);
ssr = sum((fit - mean(yf)).^2);
obj.r_sq = ssr/(ssr+sse);

plot(x(startIdx:stopIdx), fit, '--', 'Linewidth', 1.5);
legend(['ROI ' num2str(ROIno) ' data'], ['Fit:: y = ' num2str(g) ' x + '
num2str(c)]);
legend('Location', 'NorthEast');
title(['Fit to data for finding T1 [R^2 = ' num2str(obj.r_sq, '%0.2f') ']']);
hold off;

clear x y stopIdx ROIno
end

%------- Plot the TE data on a natural log scale.
function plot_TE_logScale(obj)
% Plot TE data on natural log scale. This helps the fitting
% rountine for finding the best section of straight line. Use
% these limits in the calcT2 method.
%
% SEE ALSO: calcT2

% Check that TE data has been processed.
if obj.processOption == 4
figure
% loop over all ROIs
for ROIitr = 1:obj.noROIs

% sort out the plot window
if obj.noROIs <= 3
subplot(1,3,ROIitr);
elseif obj.noROIs > 3 && obj.noROIs < 7
subplot(2,3,ROIitr);
end

if obj.noROIs >= 7
if ROIitr > 6
if mod(ROIitr,6) == 1
figure
end
end
if mod(ROIitr,6) == 0
subplot(2, 3, 6)
else
subplot(2, 3, mod(ROIitr,6))
end
end %end sorting out plot window

% loop over all TRs and get corresponding signal
```

```matlab
for TEitr = 1:obj.noTE
x(TEitr) = obj.te_Data(TEitr,1).TEval; %#ok<AGROW>
y(TEitr) = obj.te_Data(TEitr,1).roi(ROIitr,1).signal; %#ok<AGROW>
end

% plot data
plot(x, log(y), 'x' , 'LineWidth', 2, 'MarkerSize', 10);
hold all
axis square
xlabel('TE values (msec)');
ylabel('ln[signal] (a.u.)');
legend(['ROI ' num2str(ROIitr)]);
legend('Location', 'NorthEast');
set(gca, 'LineWidth', 1.5);
xlim([0 x(end)]);
clear x y
end
hold off
else
warning('MRIdata:plotLogScaleTE', 'TE data has not been processed. Run
".processMRI" method with option "4" first.');
end

end
end % END PUBLIC METHODS
```

B3.3 Protected method block

These functions are like a "black box" for the class: They have been created to

perform specific tasks specific to the processing of MRI data, but the user does

not require knowledge of them in order to use the MRIdata class.

```matlab
methods (Access = protected)
%------- sort out the names of the files to process - FA
function obj = sortFileNames_fa(obj)
% Extract file names, angles and instances into a struct object
% variable: "filedata".
% Note this expects 25 instances or frames. Anything else and
% it will fall over.

%trac progress
counter = 0;
pbar = waitbar(0, 'Organising FA file structure...');
%  no files to process
infiles = dir('*FA*.dcm');
obj.noFiles = length(infiles);

if obj.noFiles ~= 0
for fa = 1:obj.noFA %ordering angle increasing
for frame = 1:obj.noFrames %run through frames
```

```matlab
for j = 1:obj.noFiles %run through file list
if obj.fa_range(fa, 1) == sscanf( strrep(infiles(j, 1).name, '_', ' '),
obj.fa_format)%sort angle increasing
if  frame == sscanf( strrep(infiles(j, 1).name, '_', ' '),
obj.fa_instance_format)%sort frame increasing

counter = counter + 1;
per = counter/obj.noFA/obj.noFrames;

obj.filedata(fa, 1).names(frame,1).name  = infiles(j, 1).name;
obj.filedata(fa, 1).val                         = sscanf( strrep(infiles(j, 1).name, '_',
' '), obj.fa_format);
obj.filedata(fa, 1).names(frame,1).frame = sscanf( strrep(infiles(j, 1).name, '_', '
'), obj.fa_instance_format);

% progress bar
waitbar(per);

end
end
end
end
end
close(pbar);
else
error('ERR: No FA files found in directory!');
end
clear infiles
end % end sortFileNames_fa()

%------- sort out the names of the files to process - TR
function obj = sortFileNames_tr(obj)
for n = 1:obj.noTR
obj.filedata(n, 1).name = ['TR=' num2str(obj.tr_range(n)) 'ms.dcm'];
obj.filedata(n, 1).tr = obj.tr_range(n);
end
end %end sortFileNames_tr()

%------- sort out the names of the files to process - TE
function obj = sortFileNames_te(obj)
for n = 1:obj.noTE
obj.filedata(n,1).name = ['se_mc_TE' num2str(obj.te_range(n)) '.dcm'];
obj.filedata(n, 1).TEval = obj.te_range(n);
end
end % end sortFileNames_te()

%-------- generate the masks for processing
function obj = createROIs(obj, varargin)
% From v3.3 class file, here varargin contains;
% - varargin{1} -> noROIs
% - varargin{2} -> function handle to status box update
% - varargin{3} -> handles struct from GUI

% Are we using the command line
if isempty(varargin{1})
disp(' ');
obj.noROIs = input('How masks / ROIs would you like to create?  ');
```

```matlab
else
% or the GUI
obj.noROIs = varargin{1};
end

% Create new figure
figure

for i = 1:obj.noROIs
% use 1st image to get mask(s)
if obj.isFA
inImg = dicomread(obj.filedata(1, 1).names(1, 1).name);
elseif obj.isTR || obj.isTE
inImg = dicomread(obj.filedata(1,1).name);
end


% readjust contrast on image - so we can see it
curImg = imadjust(inImg);
% show the image
imshow(curImg);
title(['Create mask / ROI number ' num2str(i)]);

% Get Screen size so that figure looks big for setting ROIs
sRes = get(0, 'ScreenSize');
sRes(1) = 10;
sRes(2) = 10;
sRes(3) = sRes(3)*0.98;
sRes(4) = sRes(4)*0.90;
set(gcf, 'Position', sRes);
% allow us to select area of interest
hmask = imellipse;
title(['Create mask / ROI number ' num2str(i)]);
% wait 'til we are finished then return pos. of each vetex of the ROI
pos = wait(hmask);
% convert these positions to generate a binary mask
obj.masks(:,:,i) = uint16(roipoly(curImg, pos(:,1), pos(:,2)));
end
clear inImg curImg
close all
end%end createROIs()

%------- apply each roi to image & get the data
function obj = applyROIs(obj, varargin)
% From v3.3 class file,  here varargin contains;
% - varargin{1} -> noROIs
% - varargin{2} -> function handle to status box update
% - varargin{3} -> handles struct from GUI

if obj.isFA
% Get size of images - just use the first one.
obj.sizeChk = length(dicomread( obj.filedata(1, 1).names(1,1).name) );

% Loop over all files
for itr = 1:obj.noFA
% Loop over all frames/instances
for fitr = 1:obj.noFrames
```

```matlab
% Loop over all ROIs
for i = 1:obj.noROIs
loadImg = imadjust(dicomread(obj.filedata(itr,1).names(fitr,1).name));

% If size is the same - apply mask
if length(loadImg) == obj.sizeChk
imgData = obj.masks(:,:,i).*loadImg;

% Get data from ROIs
mskLabels = bwlabel(obj.masks(:, :, i));
stats = regionprops(mskLabels, imgData , 'meanIntensity');
% FA data variable: Y: av. intensity, X: FA angle
obj.fa_Data(itr, 1).roi(i,1).signal(fitr) = stats.MeanIntensity;
obj.fa_Data(itr, 1).angle = obj.fa_range(itr,1);
else
obj.fa_Data(itr, 1).roi(i,1).signal(fitr) = NaN;
obj.fa_Data(itr, 1).angle = obj.fa_range(itr,1);

% Error handling.
if i == 1
tmp = dicomread(obj.filedata(itr,1).names(fitr,1).name);
errSTR = ['WARNING: missed out file ' obj.filedata(itr,1).names(fitr,1).name '.
File size = ' num2str(size(tmp))...
' Mask size = ' num2str(size(obj.masks(:,:,1)))];
clear tmp

if isempty(varargin{1})
disp(['* ' errSTR]);
else
varargin{2}(errSTR,varargin{3});
end
end
end
end
end
end
end
elseif obj.isTR || obj.isTE

% Check size before applying mask later
obj.sizeChk = length(dicomread( obj.filedata(1, 1).name) );

if obj.isTR
noItr = obj.noTR;
elseif obj.isTE
noItr = obj.noTE;
end

% Loop oevr each file: either TR/TE
for itr = 1:noItr
% Loop over each ROI
for i = 1:obj.noROIs
loadImg = imadjust(dicomread(obj.filedata(itr,1).name));

% If image size is ok - apply mask
if length(loadImg) == obj.sizeChk
imgData = obj.masks(:,:,i).*loadImg;
```

```matlab
% Get data
mskLabels = bwlabel(obj.masks(:, :, i));
stats = regionprops(mskLabels, imgData, 'meanIntensity'); %#ok<*MRPBW>

% Store data depending on the processing we are doing.
if obj.isTR
obj.tr_Data(itr,1).roi(i,1).signal = stats.MeanIntensity;
obj.tr_Data(itr,1).TRval = obj.tr_range(itr);
elseif obj.isTE
obj.te_Data(itr,1).roi(i,1).signal = stats.MeanIntensity;
obj.te_Data(itr,1).TEval = obj.te_range(itr);
end

else
if obj.isTR
obj.tr_Data(itr,1).roi(i,1).signal = NaN;
obj.tr_Data(itr,1).TRval = obj.tr_range(itr);
elseif obj.isTE
obj.te_Data(itr,1).roi(i,1).signal = NaN;
obj.te_Data(itr,1).TEval = obj.te_range(itr);
end

% Problem? Display message in command line, or in GUI
if i == 1
tmp = dicomread(obj.filedata(itr,1).name);
errSTR = ['WARNING: missed out file '  obj.filedata(itr,1).name '. File size = '
num2str(size(tmp))...
' Mask size = ' num2str(size(obj.masks(:,:,1)))];
clear tmp

if nargin == 1
disp(['* ' errSTR]);
else
varargin{2}(errSTR,varargin{3});
end
end
end
end
end

end
clear loadImg mskLabels imdata
end % end applyROIs()

%------- sort out fig legends
function applyLegend(obj)
%sort out legend
% See "MRIdata.m" for full details
end % end applyLegend()

%------ sort out plot length for FA data only
function FArange = opt1plotRange(obj)
%return val depending on plot opt
retryPlot = 1;
disp(' ');
disp('---------------------------');
```

```matlab
disp(':: Choose flip angle range ::');
disp('----------------------------');
disp('a. Plot all flip angles (NOTE:: this can produce a lot of graphs)');
disp('b. input my own flip angle range');
disp(' ');
opt = input('plot range option:  ', 's');
disp(' ');

while retryPlot == 1
retryPlot = 0;

if opt == 'b'
farangeMIN = input('what is the starting flip angle to plot: ');
farangeMAX = input('what is the ending flip angle to plot: ');
if farangeMIN ~= farangeMAX
farangeSTEP = input('what is the steps between each flip angle: ');
else
farangeSTEP = 1;
end
elseif opt == 'a'
farangeMIN = obj.fa_Data(1,1).angle;
farangeMAX = obj.fa_Data(end,1).angle;
if length(obj.fa_Data) ~= 1
farangeSTEP = obj.fa_Data(2,1).angle - obj.fa_Data(1,1).angle;
else
farangeSTEP = 1;
end
else % if the user selects an option which isn't present get them to retry.
disp('*** WARNING: please select one of the options ***');
retryPlot = 1;
disp('----------------------------');
disp(':: Choose flip angle range ::');
disp('----------------------------');
disp('a. Plot all flip angles (NOTE:: this can produce a lot of graphs)');
disp('b. input my own flip angle range');
disp(' ');
opt = input('plot range option:  ', 's');
end
end

FArange = farangeMIN:farangeSTEP:farangeMAX;
end % end opt1plotRange()

%------ fit straight line to get gradient for T2
function [g, c] = getGradient(obj, x, y)
% MATLAB function for fitting to nth degree polynomial.
% "p" contains the coefficients from the fit where p(1)
% corresponds to the coefficient for the highest order term;
% in this case the x term, with degree 1.
%
% p(1) -> m
% p(2) -> c
%
% for polynomial
%   y = m x + c

if obj.isTE || obj.isTR
```

```matlab
p = polyfit(x, y, 1);
g = p(1);
c = p(2);
else
err = 0; % just for safety.
g = 0;
c = 0;
end

%            obj.err = err;
end %end getGradient
end % END PROTECTED METHODS
```

Glossary of terms

2CH	Two-chamber
4CH	Four-chamber
ADC	Analogue to digital converter
AF	Atrial fibrillation
ANOVA	Analysis of variance
AP	Anterior-posterior
ATP	Adenosine triphosphate
B_0	Main magnetic field
B_1	Radio frequency pulse
BW	Bandwidth
CAD	Coronary artery disease
CHF	Congestive heart failure
CMRI	Cardiac magnetic resonance imaging
CNR	Contrast-to-noise ratio
CO	Cardiac output
CoR	Coefficient of repeatability
CT	Computed tomography
CVD	Cardiovascular disease
DCM	Dilated cardiomyopathy
dT	Duration time
DTPA	Diethylene triamine pentaacetic acid
ECG	Electrocardiogram
Echo	Echocardiography
ED	End-diastole
EDV	End-diastolic volume
EF	Ejection fraction

Emf	Electromotive force
EPI	Echo planar imaging
ES	End-systole
ESMRMB	European Society for Magnetic Resonance in medicine and Biology
ESV	End-systolic volume
FA	Flip angle
FID	Free induction decay
FIESTA	Fast imaging employing steady-state acquisition
FLASH	Fast low angle shot
FOV	Field of view
Gd	Gadolinium
GE	Gradient echo
GRAPPA	Generalised autocalibrating partially parallel acquisitions
HCM	Hypertrophic cardiomyopathy
HLA	Horizontal long axis
HNV	Healthy normal volunteers
IR-GRE	Inversion recovery gradient echo
ISMRM	International Society for Magnetic Resonance in Medicine
LA	Left atrium
LAA	Left atrial appendage
LV	Left ventricle
LVH	Left ventricular hypertrophy
LVHD	Left ventricular hypertrophy and type 2 diabetes
LVHI	Left ventricular and ischemic heart disease
LVM	Left ventricular mass
M_0	Net magnetisation vector
MHD	Magnetohydrodynamic
MHRA	The medicines and healthcare regulatory agency

MI	Myocardial infarction
MRI	Magnetic resonance imaging
M_{xy}	Magnetisation vector in the x-y plane
N_{FE}	Number of frequency encoding steps
NHS	National Health Service
NHV	Normal healthy volunteer
NMR	Nuclear magnetic resonance
N_{PE}	Number of phase encoding steps
NSA	Number of signal averages
PCr	Phosphocreatine
PD	Proton density
PET	Positron emission computed tomography
PI	Parallel imaging
PPI	Partial parallel imaging
ppm	Parts per million
PQRST	Five deflection waves produced by the heart
PV	Pulmonary veins
RF	Radio frequency
ROI	Region of interest
RV	Right ventricle
SA	Short-axis
SAR	Specific absorption rate
SD	Standard deviation
SE	Spin echo
SENSE	Sensitive encoding for fast MRI
SLE	Systemic Lupus Erythematosus
SMASH	Simultaneous acquisition of parallel imaging techniques
SNR	Signal-to-noise ratio
SPECT	Single photon emission computed tomography

SPGR	Spoiled gradient echo
SSFP	Steady-state in free precession
SV	Stroke volume
T	Tesla
T1	Longitudinal relaxation rate
T2	Spin-spin relaxation rate
T2*	Time constant that includes spin-spin relaxation plus additional dephasing effects
TE	Echo time – the time period between the excitation pulse and signal measurement
TR	Repetition time between successive RF pulses
UK	United Kingdom
USA	United States of America
VECG	Vector ECG
VLA	Vertical long axis
α	Angle of precession from the z-axis